RADIO ENVIRONMENT MAP GENERATION AND PERFORMANCE EVALUATION IN HETEROGENEOUS ENVIRONMENTS

by

Alp Bintuğ Uzun

B.S., Computer Engineering, Yıldız Technical University, 2021

M.S., Computer Engineering, Boğaziçi University, 2025

Submitted to the Institute for Graduate Studies in
Science and Engineering in partial fulfillment of
the requirements for the degree of
Master of Science

Graduate Program in Computer Engineering

Boğaziçi University

2025

ACKNOWLEDGEMENTS

I express my sincere gratitude to my advisor, Assistant Professor H. Birkan Yılmaz, for his invaluable support, guidance, and expertise throughout the duration of this thesis.

I would also like to express my gratitude to the Department of Computer Engineering for providing access to the HPC server, which was vital for this thesis.

Furthermore, I thank Assistant Professor Doğan Ulus for his assistance in resolving the issues encountered on this server.

I also express my sincere gratitude to Alperen and Serkan, whom I consider brothers, for their precious friendship and support, knowing that we will continue to share our lives together.

I extend my sincere thanks to Aleyna for her invaluable friendship and unwavering support, knowing I could always rely on her during challenging times.

Finally, I extend my deepest gratitude to Dilara for her faith in my ability to complete this thesis even when I thought the otherwise. Her constant encouragement and evident pride in my progress were invaluable, and I thank her for her steadfast support.

ABSTRACT

RADIO ENVIRONMENT MAP GENERATION AND PERFORMANCE EVALUATION IN HETEROGENEOUS ENVIRONMENTS

The objective of this thesis is the creation of a Radio Environment Map (REM) [1] in environments with heterogeneous propagation characteristics because of it is more likely to reflect real-world conditions accurately. Moreover, the scarcity of concrete studies on this topic in the literature highlights a gap that needs to be addressed. This aim necessitates two primary areas of investigation: firstly, the simulation of REMs based on specified parameters, and secondly, the reconstruction of REMs from a limited set of measurements derived from the simulated REM. Consequently, the resulting system developed within this thesis will enable the prediction of a REM for a given area utilizing only a limited number of measurements taken within that area, without defining its propagation characteristics.

The simulation of the REM will be based on a scenario wherein the environment contains regions with differing propagation characteristics. This allows for the creation of realistic environments and their subsequent simulation. The output of this initial scenario comprises over forty thousand REMs, each with distinct characteristics.

The scenario for REM reconstruction is based on performing a limited number of measurements on the generated REMs, and subsequently utilizing these measurements to reconstruct the entire REM. Our proposed methodologies fall under two primary categories: *Single-Point Estimation* and *Full-REM Estimation.* Within each category, machine learning models employing artificial neural networks with varying architectures were developed, and their respective success rates were investigated.

ÖZET

HETEROJEN ÇEVRELERDE RADYO ÇEVRE HARİTASI OLUŞTURULMASI VE PERFORMANSININ DEĞERLENDİRİLMESİ

Bu tezin amacı, sinyal yayılma karakteristiğine bakıldığında gerçek dünyayı daha iyi yansıtabilen heterojen olan çevrelerde Radyo Çevre Haritası (Radio Environment Map - REM) oluşturulmasıdır. Ayrıca literatürde bu konuda yapılmış olan somut çalışma azlığı, doldurulması gereken bir boşluğa dikkat çekmektedir. Bu amaçta iki ana konu ortaya çıkmaktadır, ilki verilen parametrelerle REM simülasyonu, ikincisi ise simüle edilen REM üzerinden sınırlı sayıda ölçüm yapılarak REM'in yeniden oluşturulması. Böylece bu projenin çıktısı olan sistemde, herhangi bir bölge içinde yapılacak sınırlı sayıda ölçüm kullanılarak o bölgenin REM'inin oluşturulması sağlanacaktır.

REM'in simülasyonunda, haritalandırılacak bölgenin içinde farklı yayılma karakteristiklerine sahip olan bölgeler olduğu varsayılacaktır. Böylece gerçeğe daha yakın bölgeler oluşturulup bunun simülasyonu yapılabilecektir. Bu ilk senaryonun çıktısında, birbirinden farklı karakteristiklere sahip kırk binden fazla REM oluşturulmuştur.

REM'in yeniden oluşturulması için baz alınacak senaryoda, oluşturulan REM'ler üzerinde sınırlı sayıda ölçüm yapılacak ve bunlar kullanılarak tüm REM'in tekrar oluşturulması sağlanacaktır. Bunun için önerilen yöntemlerimiz iki başlıkta toplanmıştır, bunlar *Tek noktayı tahmin etme* ve *Tüm REM'i tahmin etme* olarak belirlenmiştir. Tahmin için farklı mimarilere sahip yapay sinir ağları kullanan makine öğrenmesi modelleri oluşturulmuş ve bu mimarilerin başarı oranları araştırılmıştır.

TABLE OF CONTENTS

LIST OF FIGURES

LIST OF TABLES

LIST OF SYMBOLS

A	Area of Interest
A_e	Effective Aperture
d	Distance Between Two Antennas
G_t	Transmitter Gain
G_r	Receiver Gain
H_0	Null Hypothesis
H_1	Alternative Hypothesis
I	Irradiance of a Point Light
n	Path Loss Exponent
P_r	Power Received
P_t	Power Transmitted
$\hat{P}$	Predicted Signal Power
S	Received Signal Power without the Effective Aperture
$\hat{z}(x)$	Inverse Distance Weighting for x
λ	Wavelength of the signal
β	Distance Weight
σ	Standard Deviation

LIST OF ACRONYMS/ABBREVIATIONS

2D	Two Dimensional
BHM	Bayesian Hierarchical Model
BTK	Bilgi Teknolojileri ve İletişim Kurumu
CR	Cognitive Radio
CRN	Cognitive Radio Network
IoT	Internet of Things
LoS	Line of Sight
MSE	Mean Squared Error
MCD	Measurement Capable Device
ReLU	Rectified Linear Unit
REM	Radio Environment Map
RF	Radio Frequency
PLE	Path Loss Exponent
PU	Primary User
SNR	Signal-to-Noise Ratio
SU	Secondary User

1. INTRODUCTION

In today's increasingly connected world, wireless communication systems are ubiquitous, powering everything from mobile devices and autonomous vehicles to smart grids and internet of things (IoT) [2] devices. This surge in demand places immense pressure on the radio frequency (RF) spectrum [3], a finite and tightly regulated [4] resource [5]. Although the spectrum is extensively allocated [6], it is often underutilized in some places [7–9] where large portions of frequency bands are reserved for Primary Users (PUs) [10] such as TV broadcasters, military services, or cellular operators who are frequently inactive in the licensed frequency bands [11]. For example, frequency allocation of the radio spectrum of the Republic of Türkiye can be seen in Figure 1.1.

Every country has its own regulations on RF licensing, for example, in the Republic of Türkiye, Information and Communication Technologies Authority (BTK) is the regulatory body who oversees the spectrum licensing and regulation. In the US, Federal Communications Commision-FCC oversees the spectrum allocation. In the UK, the regulatory body is the Ofcom (Office of Communications).

To address this inefficiency when accessing the RF spectrum, the Cognitive Radio (CR) [12–15] is proposed. CR systems enable Secondary Users (SUs) to opportunistically access the spectrum without causing harm to broadcasting PUs. This is achieved by enabling measurement capable devices (MCDs)-including the SUs to sense the spectrum environment and identify spectrum holes or white spaces—gaps where PUs are inactive and not transmitting. This method of enabling the SU to detect the presence of the PU is achieved by the methods of spectrum sensing.

However, reliable spectrum sensing becomes increasingly difficult in wireless environments where propagation characteristics can vary significantly. These variations are often due to propagation effects such as small scale fading—rapid changes over short distances—and large-scale fading-average changes over long distances-, which oc-

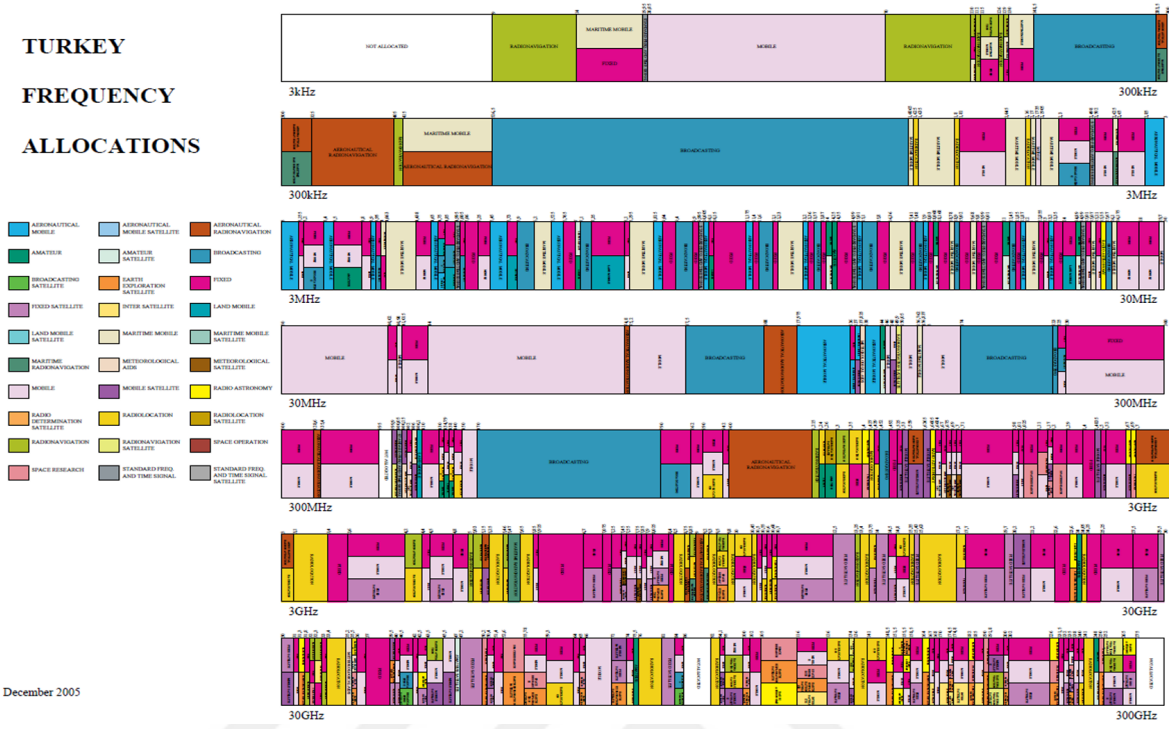

Figure 1.1. Frequency allocation of the Republic of Türkiye.

curs due to obstacles and distance. To navigate such complexities, Cognitive Radio Networks (CRNs) [16, 17] benefit from leveraging contextual awareness of the radio environment. This is achieved by constructing Radio Environment Maps (REM).

REM and the evaluation of its performance emerge as critical components in optimizing CRNs to operate efficiently in such diverse settings [18].

REM serves as a comprehensive spatial representation of the radio frequency environment. REMs enable network operators and designers to gain valuable insights into the propagation characteristics of the wireless environment. An example REM can be seen in Figure 1.2 where the received signal power is denoted by colors. The color bar scale and their respective dB values can be seen to the right of the figure. To construct this REM, a ideal environment is considered where the propagation characteristic is uniform across all locations.

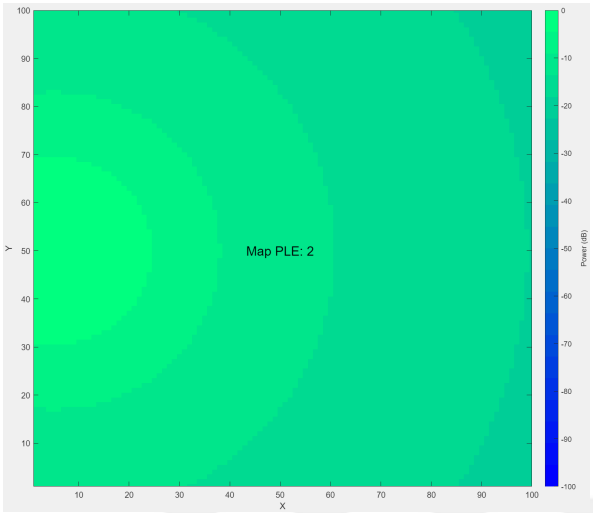

Figure 1.2. Example REM on an ideal environment with transmitter located at $(5, 50)$.

Path Loss Exponent (PLE) [19] for this environment is set to 2, PU that is transmitting is located at $(5, 50)$ and is transmitting at 92MHz, which is used by radio stations within the Republic of Türkiye.

In this context, the generation and evaluation of REMs are of great importance, serving as a base for the design, deployment, and optimization of CRNs. By accurately modeling the RF environment, we can anticipate signal propagation patterns, identify potential presence of PUs, sources of interference, and devise strategies to mitigate performance degradation.

For example, let us deploy 8 MCDs to the previous REM, which can be seen in Figure 1.3-(a), and suppose that we don't have the full REM in our hands. In order to reconstruct the REM, we will need to rely on our MCDs. We have no idea on the propagation characteristics of the environment other than the measurements taken from our MCDs. We have no idea on PU location, its propagation characteristics, or overall environment characteristics.

In our context, we are aiming to construct REMs with limited information over a *heterogeneous environment*, where propagation characteristics vary significantly within

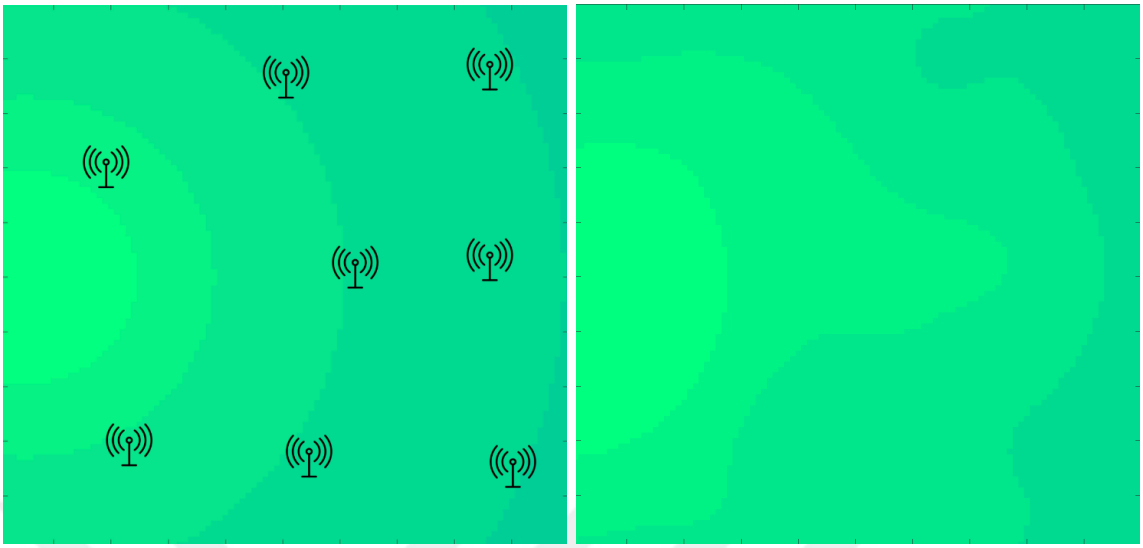

(a) (b)

Figure 1.3. (a) Example MCDs sensing the true REM - (b) Example REM reconstruction from MCD measurements.

the environment. Having different formations within the environment which effect the signal propagation characteristics is a more accurate assumption of the real world conditions. For example when constructing a REM for a wide area, such as a city, we will encounter aforementioned problems such as fading caused by buildings. But this remains true when constructing a REM for a small area, such as an office, where there is fading caused by walls or desks. A constructed REM over an area -no matter its size- will have the required information to design a reliable CRN over the said area.

In this thesis, our objective is to reconstruct the REM of heterogeneous environments from a finite amount of measurement from the sensors distributed through the RF environment. In pursuit of this objective, the preliminary information required to understand the basis of this thesis is discussed in Chapter 2. The challenges requiring resolution are detailed in Chapter 3. A systematic literature review of existing academic work addressing similar problems is presented in Chapter 4. The methodology employed and the proposed architectural framework for addressing these challenges are outlined in Chapter 5. An analysis of the most successful implementations of the proposed solutions is presented in Chapter 6.

Finally, Chapter 7 discusses potential avenues for future research, outlining topics that could benefit from further investigation and expand upon the presented work.

2. PRELIMINARY INFORMATION

This chapter discusses the preliminary information required to better understand topics of this thesis. We begin with the methods of spectrum sensing [20–22] and discuss the challenges it encounters. Then we discuss how we can overcome these challenges.

As previously discussed in Chapter 1, allocation of the RF spectrum is highly inefficient. To increase the efficiency of the RF spectrum, CR is proposed where SUs can transmit in already allocated channels while not causing interference to the channel's primary owner -the PU. This is achieved via the methods of spectrum sensing, where the SU senses the RF channel to detect the presence of the PU and the availability of the channel. And decides to transmit based on the spectrum sensing result.

There are numerous spectrum sensing techniques that are used to determine whether PUs are present or absent. Among them, energy detection [23–25] is the most commonly used due to its simple and less demanding nature. It works by measuring the energy of the received signal and comparing it to a predefined threshold. If the measured energy exceeds this threshold, the PU is assumed to be present; otherwise, the PU is considered absent and band is considered to be available for SUs. This method does not require prior knowledge of the PU's signal characteristics, making it highly adaptable but fragile. Energy detection suffers from low signal-to-noise ratio (SNR) [26] conditions, and cannot differentiate between interference (or high noise) and legitimate PU signals when SNR is low. Its performance is often evaluated using probabilities of detection, false alarm, and missed detection, which are heavily influenced by factors like SNR, threshold selection, and sensing time.

Matched filtering [27–29], on the other hand, is a spectrum sensing technique used in CR that maximizes the SNR for detecting known PU signals. It operates by correlating the received signal with a template of the PU's signal, which means it

requires prior knowledge of the PU's transmission characteristics such as frequency of the signal, pulse shape, and frame structure.

More advanced methods include cyclostationary feature detection, which exploits periodicities in modulated signals, and cooperative sensing, where multiple MCDs share their sensing information to improve detection accuracy and reduce false alarms [30].

Spectrum sensing is essentially a binary hypothesis testing problem which searches for spectrum holes:

- H_0: Null hypothesis, the PU is not transmitting and the RF spectrum is free.
- H_1: Alternative hypothesis, the PU is transmitting and the RF spectrum is occupied.

When a MCD senses the channel, there are four possible outcomes which are shown in Table 2.1. All of these outcomes impact the performance of the CR and the ability for PU & SU to transmit. These results can be interpreted as follows;

- True Negative: The SU correctly detects the absence of the PU from the channel and can safely transmit.
- False Negative: Presence of the PU is missed by the SU, which leads to the SU deciding to transmit and causing interference.
- False Positive: Absence of the PU is missed by the SU, which leads to the SU deciding not to transmit and wasting the spectrum hole.
- True Positive: The SU correctly detects the presence of the PU from the channel and can avoid causing interference.

Practical applications of spectrum sensing include TV white space devices (WSDs) that dynamically access unused television channels, using mobile devices in highly concentrated areas where there are a lot of interference, and military communication systems which needs to adapt to congestion or jammed RF spectrum by sensing spectrum

Table 2.1. Spectrum sensing - possible outcomes.

Prediction ↓	H_0 **- PU Absent**	H_1 **PU Present**
PU Absent	True Negative	False Negative (Missed Detection)
PU Present	False Positive (False Alarm)	True Positive

availability in real time. The ability of CR systems to manage spectrum access while ensuring almost zero interference with PUs is crucial to the development of wireless communication networks which use RF spectrum more efficiently.

However, ensuring the absence of PUs in heterogeneous environments characterized by different terrain, structures, and interference sources presents significant challenges such as shadowing, multipath fading, spatial SNR variance, and hidden node problem. Now let us elaborate these challenges.

Shadowing (or shadow fading) [31, 32] is a phenomenon where radio signals experience *Large Scale Fading* due to obstructions such as buildings, trees, walls, or terrain blocking the direct line-of-sight between a transmitter and receiver. In CRNs, shadowing critically affects the ability of SUs to detect PUs, potentially leading to aforementioned missed detections (false negatives) or false alarms (false positives). Effects of shadowing can be seen in Figure 2.1 where the black area represents the PU's transmission and the gray area represents the shadowing generated by the forest which reduces the received signal strength on the MCD's side.

Multipath fading [33–36] occurs when transmitted signals take multiple paths—due to reflections, scattering, and diffraction—before reaching the receiver. These multiple signals can arrive in different times, phases, and amplitudes, causing them to constructively or destructively interfere with the original signal, which leads to *Small Scale Fading*. This phenomenon is especially problematic in mobile environments and urban areas, where buildings and obstacles reflect signals. Effects of multipath fading can be

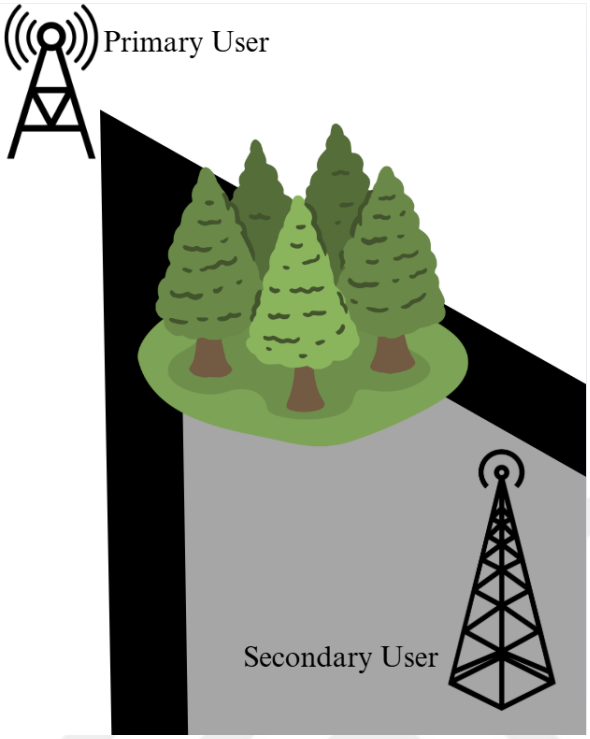

Figure 2.1. Shadowing effect on the secondary user.

seen in Figure 2.2 [37] where we have three different rays which represent the different paths the signal transmitted from the PU can take.

Path A and C reflect off of buildings whereas the path B has a direct line of sight (LoS). This means that the signal which follows path B will arrive at the MCD sooner than the signals which follow paths A and C, this effect can be seen in Figure 2.3. This makes the SU to sense the presence of the PU when it is not present.

Previously we've mentioned *Small Scale Fading* and *Large Scale Fading*. *Small scale fading* Small scale fading refers to jitter (rapid fluctuations) in the amplitude, phase, or multipath fading of a radio signal over short time or distance intervals, caused by interference between multiple signal paths. Large scale fading refers to the gradual change in the average signal power over longer distances or time, primarily due to path loss and shadowing from obstacles like buildings or terrain.

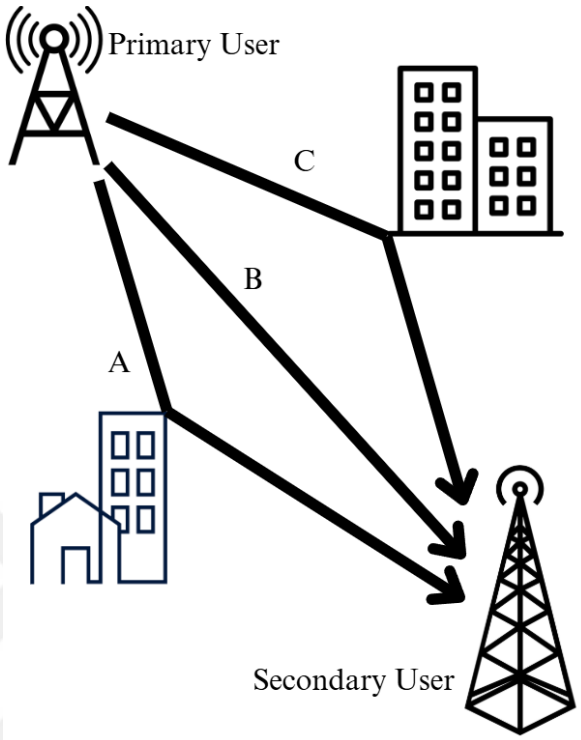

Figure 2.2. Multipath fading effect on the secondary user.

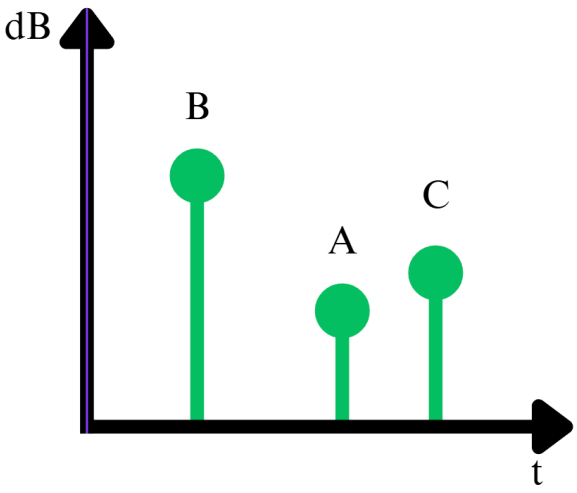

Figure 2.3. Multipath fading effect on the signal time.

Effects of these phenomenons can bee seen in Figure 2.4 where blue line expresses *Large Scale Fading* and green line expresses *Small Scale Fading*.

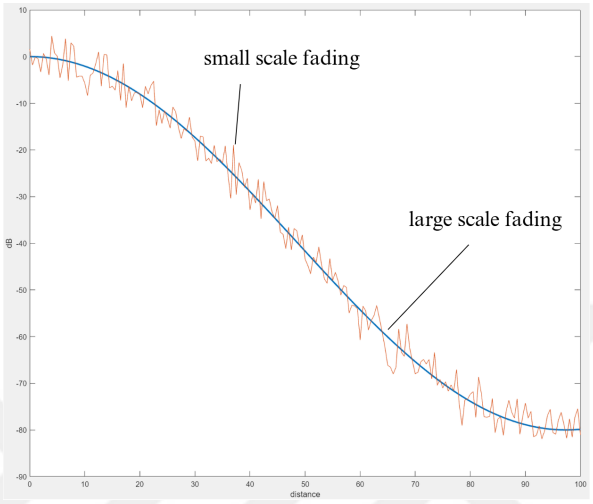

Figure 2.4. Small scale fading and large scale fading.

Spatial SNR variation refers to the change in SNR as a function of location in a wireless environment. In heterogeneous environments, such as urban areas, rural zones, or mixed terrains, this becomes more recognizable due to diverse propagation characteristics—like building or vegetation density, or even the weather condition. These variations are based on path loss, shadowing, and multipath fading. We've previously discussed shadowing and multipath fading. Now let us discuss the variance in path loss. In Figure 2.5 we can see four different zones. Zone A is a empty plains terrain, Zone B is a lake, Zone C is a forest and Zone D is an urban city. In a such environment, the signal transmitted from the PU to the Zone D will have to go through different zones with different path loss characteristics. Zone A and B will have a relatively low path loss, while zones C and D will have high path loss. Any signal coming from the PU will have to go through different zones and will have to face spatial loss variations, this effect will be observable even in the same zones with high variations such as urban areas. This topic will be discussed in detail in upcoming chapters.

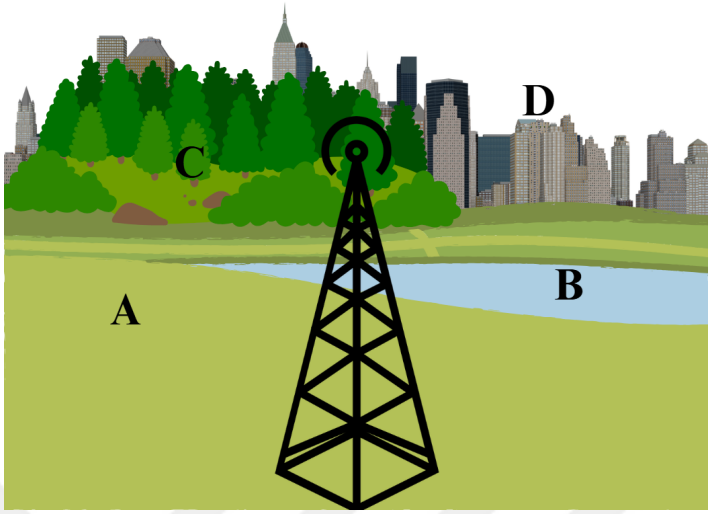

Figure 2.5. Path loss variance example.

The hidden node problem [38–40] happens when two devices (like wireless users) are both trying to talk to the same receiver but can't hear each other because they're too far apart. Since they don't know the other is transmitting, they might send data at the same time, causing their signals to collide at the receiver and making the transmitted signal unclear or lost entirely.

The hidden node problem in cognitive radio networks arises when a SU fails to detect the presence of a PU due to obstacles, aforementioned fading problems, or shadowing, and consequently transmits on the same frequency, causing interference. This issue is especially severe in our case, heterogeneous environments, where diverse terrain, infrastructure, and material properties cause spatial variations in signal propagation. For instance, buildings, hills, forests, or even walls can block PU signals in one area while leaving them detectable in another, creating zones where some MCDs are effectively "blind" to ongoing PU activity.

Now let us visualize hidden node problem with Figure 2.6. We have two secondary users. SU-1 transmits in area A, SU-2 transmits in area E, and PU transmits in area C. Intersection of area A and area C is area B, where SU-1 and PU can interfere with each

other. Intersection of area C and area E is area D, where SU-2 and PU can interfere with each other. Let us consider SU-1 and SU-2 to be out of the boundaries of area C. As we can see in the figure, there is a mountain range between the SU-1 and the PU, which cripples the ability of SU-1 to detect the PU, this makes the PU a hidden node for SU-1. In such an environment, SU-1 might transmit when PU is active, this will result in interference in area B. Whereas the PU is in range of detection for SU-2 and is not a hidden node for it, which means SU-2 can correctly detect the presence of the PU and no interference should be observed in area D.

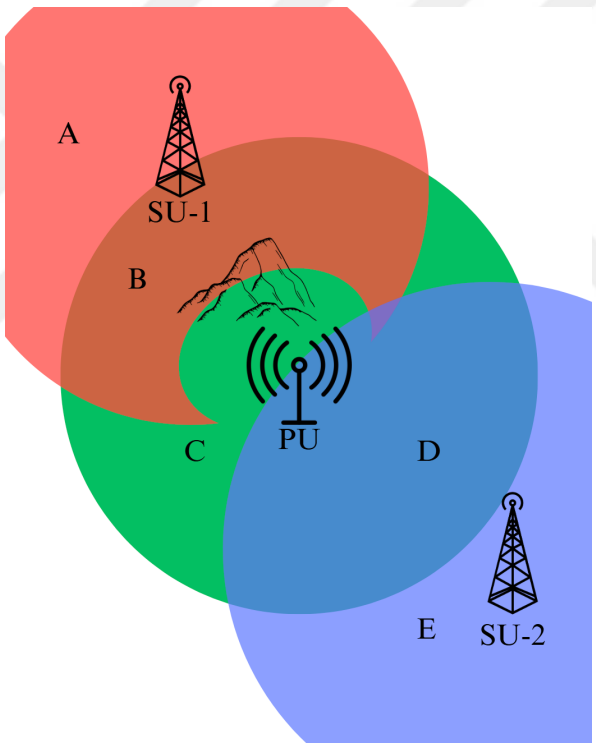

Figure 2.6. Hidden node example.

A Radio Environment Map (REM) [41–45] is like a smart map that shows where and how the radio signals are being used in an area. In CR, REM helps devices understand the radio environment better—like where signals are strong or weak, and which frequencies are busy or free.

This information helps the system make smarter choices about when and where to send data without causing interference. REM supports spectrum sensing by giving extra context, so devices don't just guess what's happening—they use a more complete picture to find the best open channels.Previously mentioned problems can be solved by REM as follows;

- Hidden Node Problem: Given that the REM stores spatial information about PU activity, a CR node (SUs) can consult the REM to presence of the PU even when it cannot sense PU directly.
- Spatial SNR Variation: REM stores general propagation characteristics of an environment, therefore a CR node can predict SNR value in a location before transmitting.
- Multipath Fading: REM identifies areas prone to multipath fading (e.g., near reflective surfaces like water or buildings), so CR can switch to modulation schemes less sensitive to delay caused by multipath fading.
- Small & Large Scale Fading: REM stores signal variations in the environment of interest, so the CR node can change its propagation methods based on this (e.g., increasing transmission redundancy, increasing transmit power).

Also, to simulate a REM, we need to calculate the received power for every point within the REM. To do so, the Friss Transmission Equation will be used, which can be represented as

$$P_r = P_t G_t G_r (\frac{\lambda}{4\pi d})^n \tag{2.1}$$

where P_r describes received power, P_t describes transmitted power, G_t and G_r are gains for transmitting and receiving antennas respectively, λ describes the wavelength of the transmitted signal, d describes the distance between transmitting antenna and receiving antenna, n describes the PLE. The PLE is 2 when the free space propagation holds. But in our case, it can be as low as 1.80 in LoS Indoor Propagation [46] and as high as 4-6 in building obstructed paths [47].

3. PROBLEM DEFINITION & MOTIVATION

This section is dedicated to the introduction of the problems to be addressed and solutions proposed within the scope of this thesis. Initially, we will deconstruct the topic of *Radio Environment Map Generation and Performance Evaluation in Heterogeneous Environments*, explain its fundamental components, and analyze the challenges encountered.

Let us begin by defining the term 'Heterogeneous Environment'. When an RF environment contains different areas with different propagation characteristics, it is called a heterogeneous environment. Heterogeneous environments are especially useful to work on thanks to their better approximation of the real world cases. Basing the Radio Environment Map (REM) on heterogeneous environments instead of uniform and controlled environments makes us better adept our techniques to the real world conditions and make our results closer to the reality.

First step into the process REM simulation is calculating the received signal strength at any given point. This calculation will be performed using the Friis transmission equation which can be represented as

$$P_r = P_t G_t G_r (\frac{\lambda}{4\pi d})^n \tag{3.1}$$

where P_r describes received power, P_t describes transmitted power, G_t and G_r are gains for transmitting and receiving antennas respectively, λ describes the wavelength of the transmitted signal, d describes the distance between transmitting antenna and receiving antenna, n describes the PLE.

Utilizing Equation (3.1), it is possible to generate a REM in a homogeneous environment as it was previously shown in Figure 1.2 – that is, an environment where PLE remains consistent throughout. However, this approach does not accurately reflect real-world conditions. When mapping a given area, the presence of diverse structures

within that area will result in variations in PLEs. For instance, an area may encompass regions with low PLEs, such as plains, alongside regions characterized by high PLEs, such as urban areas or forests.

Consequently, when an area contains multiple PLEs, the formula specified in Equation (2.1) becomes inapplicable because the equation assumes a clear, direct LoS between transmitter and receiver, with no obstacles, reflections, or interference and a constant PLE. This leads us to the first problem we will define in this section: how should the transmitted signal strength be calculated to generate a REM in environments with heterogeneous propagation characteristics?

Generating a REM is only the first of several challenges to be investigated within the scope of this project. In the real world, it is neither feasible nor practical to create a REM by physically measuring signal strength at every point, nor is it reasonable to expect to know the true values of the Gain and PLE for all locations. Therefore, we must assume that we have limited information available for REM generation. This leads us to the second problem addressed in this project: what approach should be adopted for REM estimation, and which parameters significantly impact the success of REM prediction? How can we successfully reconstruct a REM with having limited information, such as small numbers of measurements?

So, let us define our problem, let:

- $A \subset \mathbb{R}^2$: The area of interest.
- $s_i \in A$: The 2D location (i.e. $s_i = (x_i, y_i)$) of the i-th measurement capable device (MCD).
- $P_r(s_i)$: The measured signal power (including noise and interference) at s_i.
- N^{MCD}: Number of MCDs.
- $\chi = \{(s_i, P_r(s_i)) | i = 1, 2, ..., N^{MCD}\}$: The set of measurements from all MCDs.
- $\hat{P}_r(x, y)$: The predicted signal power at (x, y).
- $P_r^*(x, y)$: The real signal power (excluding noise and shadowing) at (x, y).

Given these, the objective is to find a function that estimates the mean signal power at any given location $f : A \to \mathbb{R}$ such that:

$$\min_{f} \frac{\sum_{(\mathbf{x},\mathbf{y})\in A} \left(f(\mathbf{x},\mathbf{y}) - P_r^*(\mathbf{x},\mathbf{y})\right)^2}{|A|}$$

The optimum f, call it f^*, will be utilized to predict the signal strengths for unknown points within the area of interest A, and minimize the square error. In this case our estimate will be evaluated as follows:

$$\hat{P}_r(x, y) = f^*(x, y)$$

By doing so, we are aiming to predict the signal strengths for unknown points within the area of interest and minimize the square error.

The literature review conducted to answer these questions will be presented in Chapter 4, while our proposed solutions will be discussed in Chapter 5. The performance metrics of the selected solutions will be detailed in Chapter 6, and topics beyond the scope of this project, but potentially relevant for future research, can be found in Chapter 7.

4. RELATED WORK

The construction of radio environment maps has been a hot topic for the past decade. In this chapter, we discuss related work in this chapter.

In a 2021 study, Xu et al. [48] proposed an analysis framework based on spectrum data collected by spatially distributed sensors to construct the REM. Researchers propose a three-stage Bayesian Hierarchical Model (BHM) to mimic the spectrum data generation process under spatially correlated shadow fading. The parameters of BHM are estimated with the Markov chain Monte Carlo algorithm from data collected by the sensor network.

In another study from Zhang et al. [49] propose that traditional spectrum sensing method, based on Nyquist-Shannon sampling theorem will not be suitible in high frequency spectrum bands. In their paper, they propose an adaptive compressed spectrum sensing algorithm based on REM dedicated for space information networks to address this claim.

In another study by Hu et al. [50], researchers aim to solve false spectrum measurements crowdsourced-based spectrum sensing models. They introduce ST-REM, where they mix self-label techniques developed for semi-supervised learning with spectrum sensing. They propose to use two different kinds of MCDs; a small group of highly trusted and fixed MCDs, and one big group of mobile users. They propose a iterative method to evaluate the trustworthiness of mobile secondary users to overcome false spectrum measurements.

In a 2013 study, Yilmaz et al. [41] provide a comprehensive analysis on REM construction techniques and REM architecture. Researches define False Alarm, Missed Detection, and Correct Detection zones to discuss what happens when Real-REM and Estimated-REM do not overlap perfectly. In False Alarm Zone, there is no PU but

Estimated-REM thinks that there is, so SU broadcast is prohibited. In Missed Detection Zone, the PU is present but its presence is missed and SUs are free to broadcast. Also, researches investigate REM construction methods and divide them under two categories; Spatial Statistics Based Methods and Transmitter Location Determination Based Methods. Methods in the first category try to estimate areas without any measurements based on spatial statistics of specific locations. Methods in the second category try to locate the PU first, estimate the signal strength at each location later.

In a 2014 study, Pesko et al. [44] created a comprehensive survey about REM construction methods. In this study, researchers divided REM construction methods into three categories; Direct Methods, Indirect Methods, and Hybrid Methods. Direct Methods are using interpolation approach to estimate the signal levels at locations of interest. Indirect Methods are using estimated or known parameters of the transmitter and radio propagation environment. These methods first need to estimate the characteristics of the transmitter (e.g. location, power, antenna height) and construct the REM based on these estimations.

In a different study, Wang et al. [51] proposed a method to use REM in satellite-to-land communications. In this study, REM is used to determine when Low Earth Orbit (LEO) CRN should use the spectrum band used by Geostationary Earth Orbit (GEO) PU. In this study, REM is constructed by using SS methods to provide the spatial description of the GEO PU signal.

In a privacy based study, Amin et al. [52] aims to preserve location privacy of crowdsourced-based spectrum sensing agents. In this paper, SUs report their approximate location calculated by Planar Laplacian mechanism, instead of their real location. The study constructs different REM predictions with different privacy thresholds and compares the results.

In another study, Meshkove et al. [53] propose a method to construct Indoor REMs. In this study, researchers managed to create a testbed to empirically study the

construction of Radio Environmental Maps over a area that spans several rooms with both non load-bearing (paper) and bearing (semi-concrete) walls.

In an effort to handle heterogenous primary users Vizziello et al. [54] propose a resource management framework using REM for handling heterogeneous primary users in CR networks. In their study, they use a Cyclostationary Autocorrelation Function to detect and classify PU signals, and then they extract the features of the heterogeneous PUs.

In a 2009 study, Willink and Rutagemwa proposed a framework to evaluate CRNs in heterogeneous environments [55], they outline that controlled environments in IEEE 802.22 is unrealistic and MCDs will probably be different kinds of spectrum users, such as radio or radar. They draw attention to the inability to communicate of these kinds of MCDs and define a heterogenous environment based on the characteristics of spectrum users and their inability to communicate with each other, thus congesting the spectrum.

Pesko et al. propose a solution to constructing radio environment map using omnidirectional or directional transmitter antenna named self-tuning method [56]. The proposed method operates using the characteristics of the operating environment estimates the transmitter characteristics. Success of their method vary based on the directionality of the transmitter antenna, the method achieves a root mean square error of 5 at high number of measurements and using directional antenna, and achieves an error of 12 when using an omnidirectional antenna at the same number of measurements. This research is more closely related to our topic; however, the researchers have detailed information about the environment in which the REM will be constructed, and based on this information, they estimate the PU characteristics and generate the REM accordingly. In our case, however, the characteristics of the environment are not known in advance. Instead, they are estimated based on the measurements conducted by the MCDs, and the REM is created using these estimations

Recommendation made by Radiocommunication Sector of the International Telecommunication Union; ITU-R 1546-6 [57] has been the closest source to our problem that we could find. It proposes a propagation method for three different paths; land paths, sea paths, and mixed land-sea paths. This Recommendation also covers radio frequencies ranging from 30 MHz to 4 GHz, describes a method for point-to-area radio propagation predictions for terrestrial services. Recommendation covers paths up to 1 000 km length for effective transmitting antenna heights less than 3 000 m.

Now let us quickly summarize methods and categorize their performance metrics in Table 4.1. As it can be seen in the same table, researcher are usually using RMSE for evaluating their performance metrics.

Table 4.1. Summary of other REM generation methods.

Citation	**Summary**	**Performance Metric**
Pesko et al. [56]	Introduces a method to estimate the transmitter characteristics.	RMSE
Kaniewski et al. [58]	Divides environment into different zones by their distance to the nearest transmitter.	RMSE
Qi Chen et al. [59]	uses generative adversarial network algorithms to predict the REM	RMSE
Yifan Wang et al. [60]	proposes a first predict-then-correct method with a generative adversarial network	RMSE mean absolute error (MAE) structural similarity (SSIM) peak signal-to-noise ratio (PSNR)
Yuxuan Li et al. [61]	they predict PLE using a hybrid transformer-convolution model.	RMSE

5. METHODOLOGY

In this section, we present our methodology, which consists of two main steps. In the first step, we will generate a REM dataset through simulation; this process will be discussed in detail in Section 5.1. In the second step, we will utilize and manipulate the generated dataset to train a neural network. Using this trained model, we aim to estimate the REM of a region based on a limited number of measurements collected from that region. This step will be elaborated in Section 5.2

5.1. REM Generation

The steps of the process we defined for generating a REM are illustrated in Figure 5.1. As shown in this figure, the first step is to define the propagation characteristics of the region to be simulated. In our case, the transmitting PU has the same characteristics throughout the entire project, Based on these characteristics, we must then select the algorithm that will provide the most realistic simulation. Subsequently, the simulation is carried out, and a comprehensive dataset is generated that includes regions with varying propagation characteristics. This dataset will form the foundation for the success of the methodology described in Section 5.2.

To understand different zones and their characteristics, let us consider Figure 5.2. In this figure, there are three different zones, and a base map. Let us consider the Zone 0 as plains terrain, Zone 1 as a mountain range, Zone 2 as a metropolitan area, and Zone 3 as a lake. All of these zones have different propagation characteristics. Zone 1 might have a higher path-loss exponent, Zone 2 might have a higher interference, Zone 3 might have a lower path-loss exponent. This might cause bad reception of PU signal in Zone 2 but a strong reception in Zone 3 with direct Line of Sight (LoS) to the PU. All of these parameters should be considered to simulate a REM.

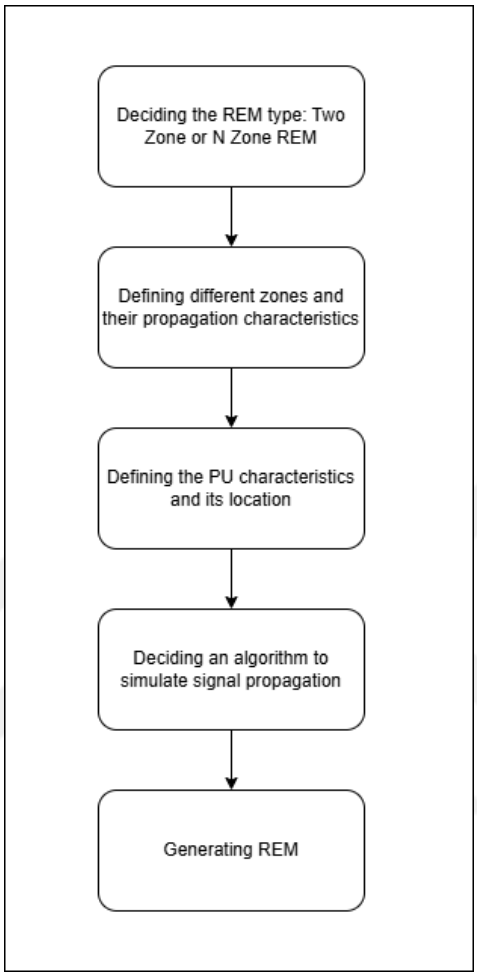

Figure 5.1. REM generation steps.

5.1.1. Simulation

To simulate our REM, we will use the Friis Transmission Equation as it was discussed in Chapter 2, specifically the Equation (2.1).

But this equation holds for constant Path Loss between two points. In our case, we have different zones with different path loss exponents. A direct path between the PU and a MCD can easily pass through multiple zones. In this case, the Friis equation does not hold. In such cases, we should follow the solution proposed by ITU-R 1546-

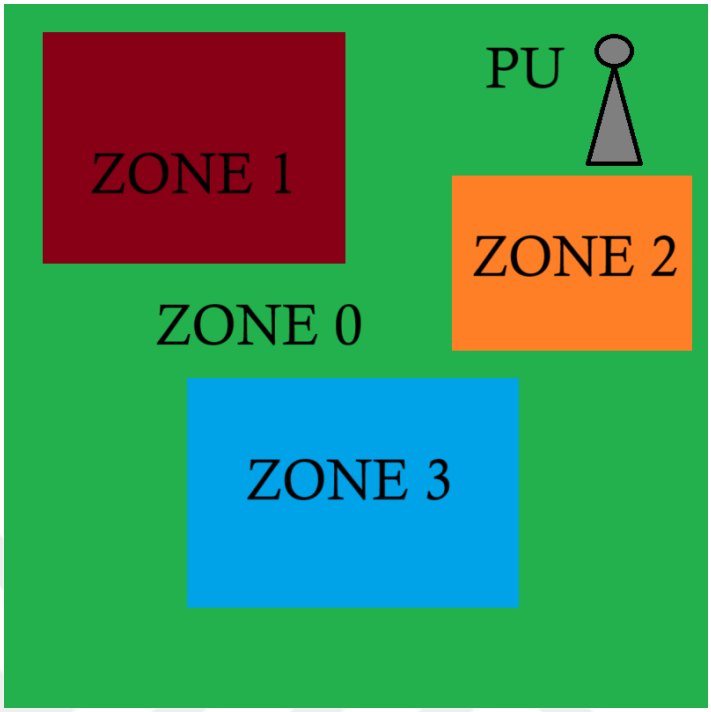

Figure 5.2. Visualization of different zones.

6 [57] where we modify our received power equation as

$$P_r = \sum_{i=1}^{k} \frac{P_{r(i)} d_i}{d_{total}}$$
$$P_{r(i)} = P_t G_t G_r (\frac{\lambda}{4\pi d_{total}})^{n_i} \tag{5.1}$$

where n_i is the PLE of i-th zone and d_i is the distance traveled within the i-th zone. Following this equation, if our PU and MCD are separated with two zones; Zone_1 and Zone_2 with $n_1 = 2n_2$ and $d_1 = d_2$ we end up with $P_r = \frac{P_{r(2)}^2 + P_{r(2)}}{2}$. Visualization of this can be seen in Figure 5.3.

After this, we might end up with a REM like shown in Figure 5.4 where colder colors show lower signal strength. In this case, our Zones change at $X = 50$, as it can be seen in the same figure, characteristics of propagation is changed. The wave shapes are more steep at the $X \geq 50$ zone because PLE is set to 4 whereas it was 2 in $X < 50$ zone.

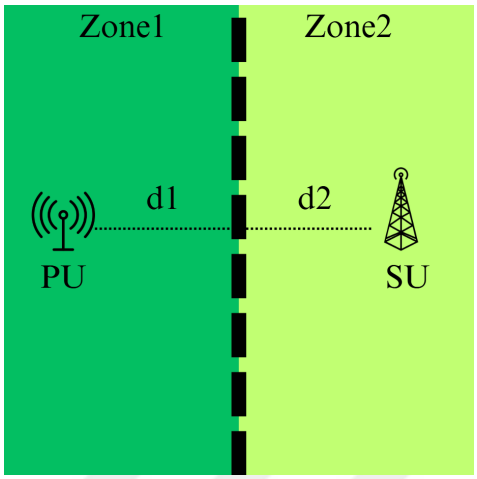

Figure 5.3. Two-zone visualization.

However, there is a significant flaw in this method. If we change the order of the regions we previously discussed – for example, placing the region with PLE = 4 in the $X < 50$ area and the region with PLE = 2 in the $X \geq 50$ area – the result observed in Figure 5.4 appears as in Figure 5.5-(b). The reason for this is that in the previously mentioned scenario, when using Equation (5.1) in the range $0 > X > 50$, the loss is high in the area with a high PLE value because it passes through that area. Afterwards, in the following range, since both the path length and signal transmission power are used in areas with both low and high PLE values, these values accumulate and increase. Therefore, an increase in the received signal strength is observed when transitioning from a high PLE value to a low PLE value.

This situation is not intuitively accurate. For instance, consider a region served by a single base station. Suppose there is only one building in this area, and no structures exist that could cause signal reflections. In such an environment, if the signal strength is weak inside the building, and upon stepping outside the building the structure still lies between the receiver antenna and the base station, it is unreasonable to expect an increase in signal strength due to the shadowing generated by the building.

If this example remains unclear, let us repeat the same thought experiment using the visible light frequency range of the electromagnetic spectrum. In this version,

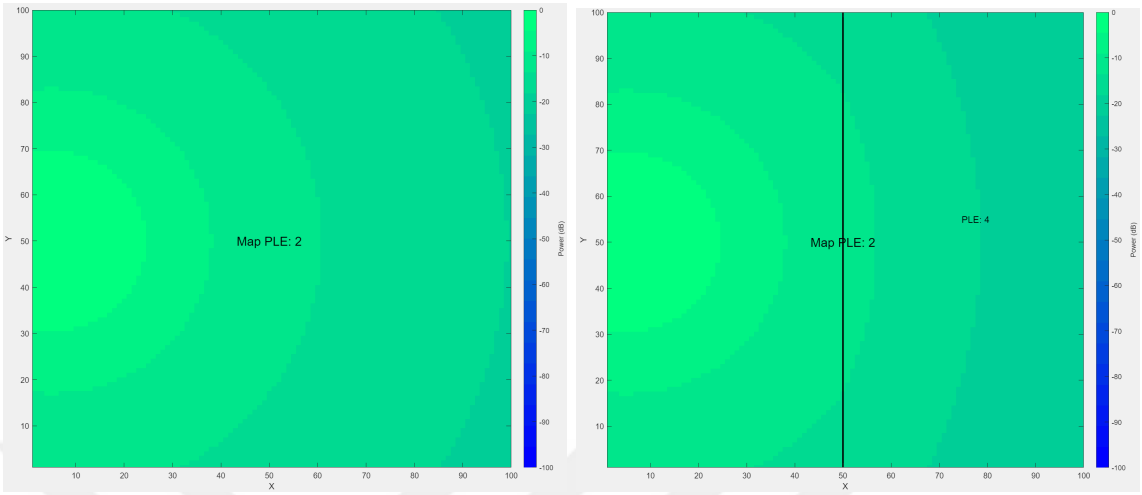

(a) (b)

Figure 5.4. ITU-R 1546-6: simulated REM (a) ideal environment (b) two different zones.

imagine a flashlight in place of the base station and a box covered with dark-tinted glass representing the building. When this thought experiment is repeated, if the flashlight appears dim when viewed through the dark glass from inside the box, it would be illogical to expect the flashlight to appear brighter when viewed from outside the box through the same tinted glass.

Now let us examine this example in depth. Let us imagine a point light source and try to calculate the irradiance of a point in a ideal space. This can be represented as

$$I = \frac{P}{4\pi d^2} \tag{5.2}$$

where I is the irradiance [62], meaning the intensity of light for a given point (W/m^2). P denotes the total radiant power emitted (W), and d is the distance between the source of the light and the point of interest.

This equation is similar to what we've discussed under Equation (2.1), but there are a few differences because the Friis equation takes the characteristics of the receiving

antenna into account, it does not reflect the signal power for a point in space, but it reflects signal power perceived by an antenna.

So let us break down that Equation (2.1) into

$$\begin{aligned} P_r &= SA_e \\ S &= \frac{P_t G_t}{4\pi d^2} \\ A_e &= \frac{G_r \lambda^2}{4\pi} \end{aligned} \tag{5.3}$$

where S denotes the received signal power at a given point in an ideal space (W/m^2) and A_e denotes the effective aperture of the receiving antenna.

Now equations 5.2 and 5.3 look similar when we compare the I to the S. Therefore, if we do not account for the characteristics of the receiving antenna and focus purely on the transmission environment, visible light and radio waves should have similarities in behavior.

However, when the previously mentioned ITU-R Recommendation P.1546-6 is applied, the signal strength is predicted to increase with distance upon exiting the building. In other words, according to this model, the flashlight appears brighter when observed from outside the box, even though it is still viewed through the obstructing structure—an outcome that contradicts physical intuition.

When investigating a solution to this problem, the first approach that came to mind was to calculate PLE specified in Equation (2.1) as

$$n = \sum_{i=1}^{k} \frac{n_i d_i}{d_{total}} \tag{5.4}$$

where n_i is the PLE of the ith region, d_i is the distance traveled within the ith region, and the d_{total} is the total distance between the transmitter and the receiver.

Essentially, our aim was to address the issue inherent in the ITU-R Recommendation P.1546-6, namely the neglect of local PLE values, by computing the average PLE using locally observed PLEs.

Although this proposed solution does not fully resolve the previously mentioned issue, it offers a partial improvement over ITU-R Recommendation P.1546-6. As illustrated in Figure 5.5-(c), while the abrupt increase observed earlier has been mitigated, a residual increase still remains. Intuitively, when transitioning from a region with a high PLE to one with a lower PLE, we would expect not an increase in the received signal strength, but rather a reduction in the rate at which the signal strength decreases with distance. Therefore, a new solution must be proposed to address this discrepancy.

In our final proposed solution, we are replacing the term d_i with a new term $d_{i_{weighted}}$, we also suggest replacing the d_{total} term found in Equation (5.1) with a new term, $d_{weighted}$. Final equation that we will use to calculate the received power can be represented as

$$\begin{aligned} P_r &= \sum_{i=1}^{k} \frac{P_{r(i)} d_{i_{weighted}}}{d_{weighted}} \\ P_{r(i)} &= P_t G_t G_r (\frac{\lambda}{4\pi d_{total}})^{n_i} \\ d_{i_{weighted}} &= d_i^{n_i} \\ d_{weighted} &= \sum_{i=1}^{k} d_{i_{weighted}} \end{aligned} \tag{5.5}$$

where $P_{r(i)}$ denotes the received power for the PLE i, $d_{i_{weighted}}$ denotes the weighted distance of the ith zone, and the $d_{weighted}$ denotes the summation of the weighted distances.

Making these two changes will help us better reflect the different PLEs and their effects on the signal strength. With this proposal, our objective is to compute the total distance from the MCD to the PU by taking into account the PLE values of the regions traversed. In doing so, we aim to appropriately reduce the rate of signal strength

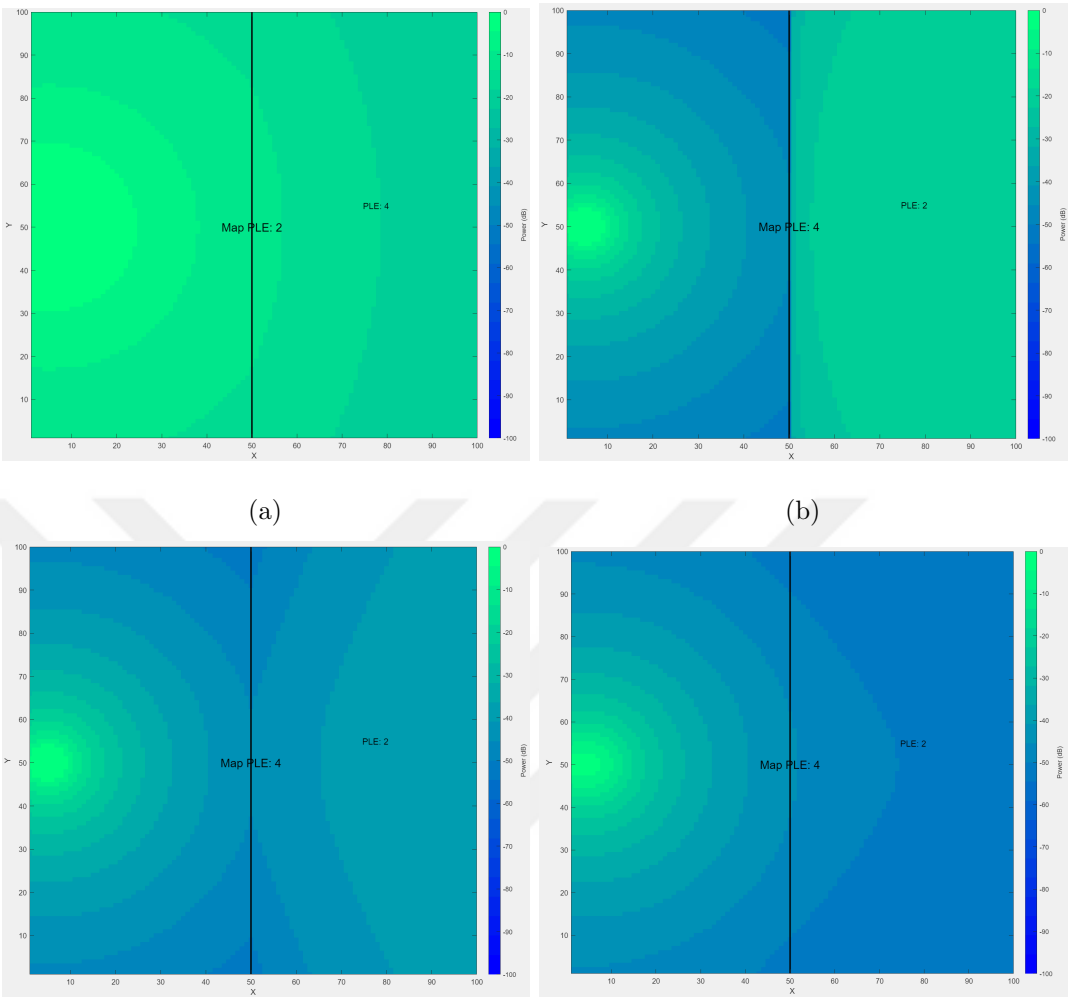

(a) (b)

(c) (d)

Figure 5.5. (a) ITU-R 1546-6: simulated REM in figure 5.4, (b) ITU-R 1546-6: simulated REM-2 (c) proposed solution I: simulated REM (d) proposed solution II: simulated REM.

attenuation following a transition from a high-PLE region to a low-PLE region. As demonstrated in the simulation results shown in Figure 5.5-(d), the frequency of color transitions—indicating the rate of signal attenuation—decreases after the line $X = 50$, which reflects a reduction in the signal strength decay rate, as expected.

From this point onward, as described in Section 5.1.2, method we have preseneted in Equation (5.5) will be employed for REM generation.

5.1.2. REM Database Generation

In this step, we simulate different REMs with different PU locations, transmit powers, and zones. We initialize every REM with randomized parameters. After that we simulate them and save its properties such as received powers in every location, PU information, and different zone information into our database.

To generate this database first we have to set a few standards. We have set the size for our environment to $(128, 128)$ which can be interpreted as a 128 meter by 128 meter square zone. We have set the transmitting frequency of our PU to 92 MHz to represent real world usage, this frequency band is used by radio stations within Turkey.

Then we have decided on two different map types, one with two different zones with different propagation characteristics, essentially dividing the map into two at $x = 64$ or $y = 64$. The other consists of N different zones where $1 \leq N \leq 5$, which also contains the previously defined ZONE 0. Zones are rectangles with their locations and proportions are randomly generated, yet they must reside within the map. If one or more regions overlap (for example, a building or a lake inside a forest), the most recently created region will override the characteristics of the overlapping regions within its own boundaries. In other words, within the area of overlap, the properties of the latest defined region will take precedence over those of the previously defined regions.

No matter the map type, different zones can have a PLE value with range of $2 \leq PLE \leq 5$. PLE value for each zone is randomly generated within the specified range.

Also, the location of the PU is randomly selected with in the range of $-128 \leq x \leq 256$ and $-128 \leq y \leq 256$. This helps us create different REMs, where in some the PU is a resident of the area of interest, meanwhile in most, it is not.

After deciding the characteristics of the REM as previously stated and generating the PU, we go into simulating the REM itself. We start by implementing a method to calculate the distance between a point of the REM we are trying to calculate the received signal power and the PU. Then we create a structure to store the path information. This path information contains the direct LoS path between PU and the target location, and also contains which zones the signal goes through, and distance covered within each zone. An example for this can be found in Figure 5.6 where the PU is transmitting to point A which is visible on the map. As it is visible on the same figure, the signal has to travel through three different zones, and the propagation characteristics it faces will change four times. First, it will travel through ZONE 0, then it will enter ZONE 2 and face its first change on propagation characteristics, then it will re-enter ZONE 0, then go through ZONE 3, and end its journey in ZONE 0.

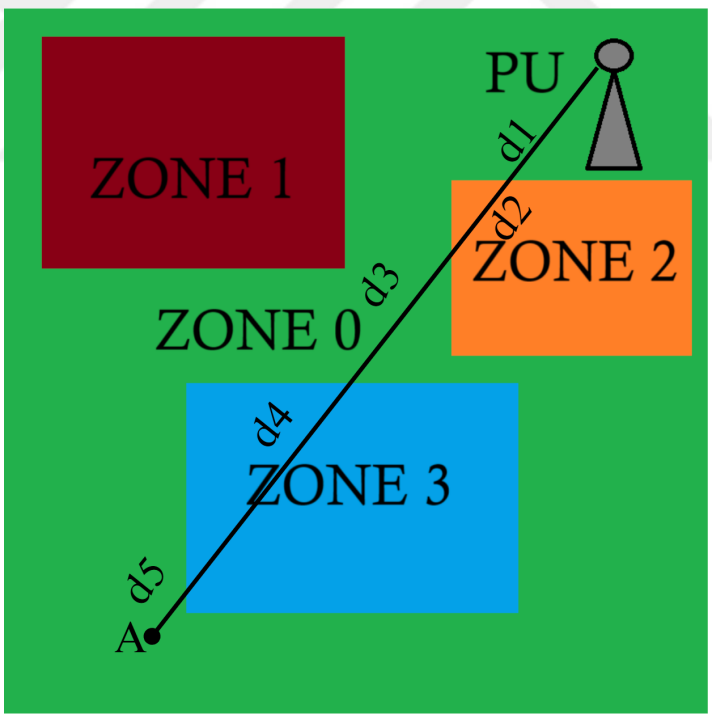

Figure 5.6. REM generation example: creating the direct LoS path information.

After generating a structure to hold all the relevant information about the signal path, we are calculating the received power for $d_{weighted}$ by using Equation (5.5).

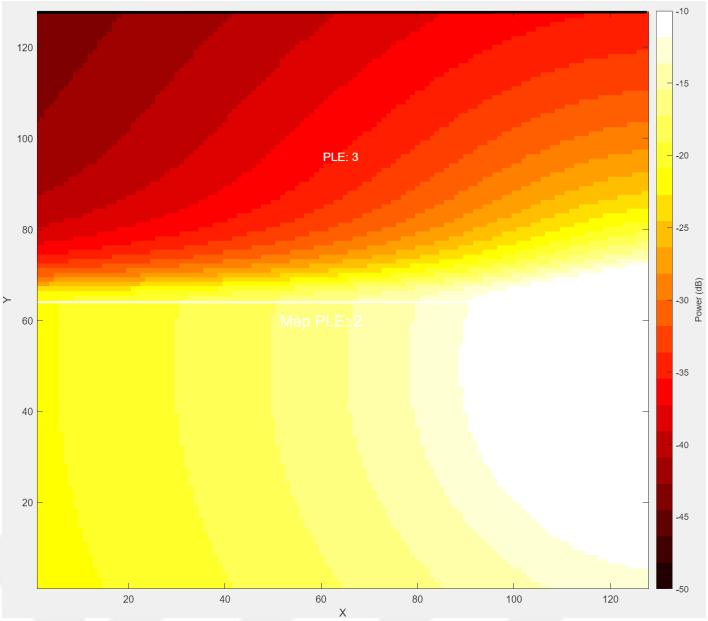

Figure 5.7. Generated two zone REM example: 1.

Now let us examine some REMs generated using this technique, in all the graphs white denotes high signal power, then comes the yellow and orange, then red, which denotes low signal power. First, we will construct 5 REMs using the two zone REM type. In Figure 5.7, we can see a two zone REM divided at $y = 64$ where a low PLE zone stands at $y < 64$ and high PLE zone stands at $64 < y$. The PU for this example is located at $(140, 55)$. The high PLE zone in this example, creates a rapid decline in received signal strength at $y > 64$, which can be seen in the same figure. Because the REM is located at $x = 140$, the right side of the high PLE zone receive a better signal.

In Figure 5.8, we see two similar REMs side by side, of Figure 5.8-(a) we see the higher PLE region on the left, meanwhile it is the opposite of 5.8-(b). We observe the color changes appear more frequently at higher PLE zone, which represents a increase of the rate of which the signal power decreases. In the case of the Sub figure (a), the PU is located just outside of the boundaries of the low PLE region, and resides in a high PLE zone. This means that the high signal power penetrates through the low PLE zone on the right, shines in it, and gets slowed when it hits $x = 64$ and faces the high PLE zone, and the low signal power zones at the top and bottom right corners of this map is caused by the high PLE zone which the PU resides in. In this example,

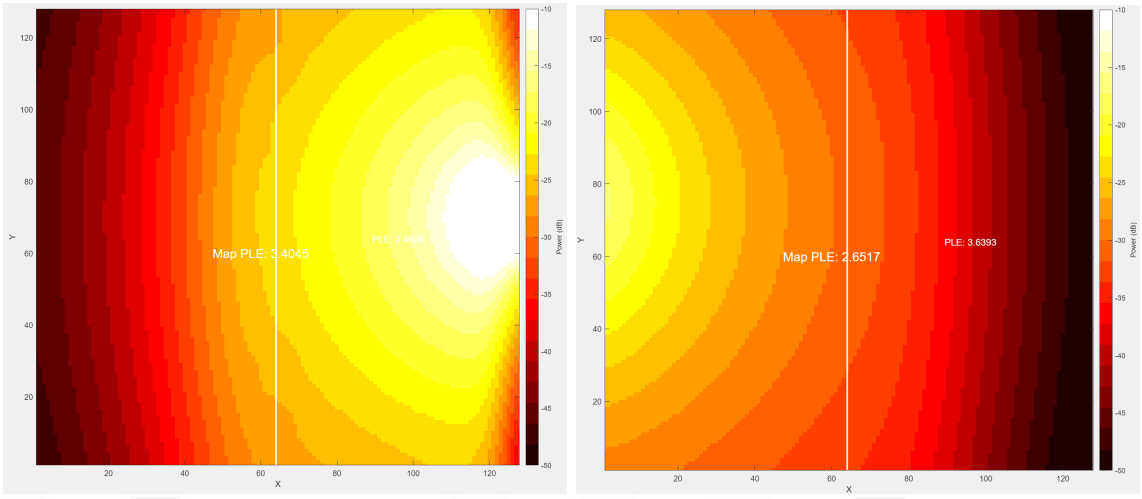

(a) (b)

Figure 5.8. Two similar REMs (a) generated two zone REM example: 2 (b) generated two zone REM example: 3.

signals start in a high PLE zone, then enter a low PLE zone, and re-enter the high PLE zone at $x = 64$. In the case for Sub figure (b), the PU is in the low PLE zone and the signals only face a PLE change at $x = 64$.

In Figure 5.9, the PU is located at the top left side of the area of interest and there is a relatively high PLE zone at the top, and relatively low PLE zone at the bottom and we can see the shadowing created by the top zone clearly at the $50 < y < 80$ zone which gets looser with the distance to this zone, also a relief on signal strength when we get lower parts of the map, which is caused by relatively low PLE of that zone.

Figure 5.10 presents the most interesting situation of two zone REMs so far. Given that there is a high signal power zone at the top left of the area of interest, we might think that PU is located to the top left of the map, but interestingly enough, the PU is located at $(125, 180)$, which is to the top right of the map. Because there is a high PLE zone in front of the PU at the right side of the map, we see the signal power drop significantly in that zone also we can see the shadowing effect of this zone to the low PLE zone in the left.

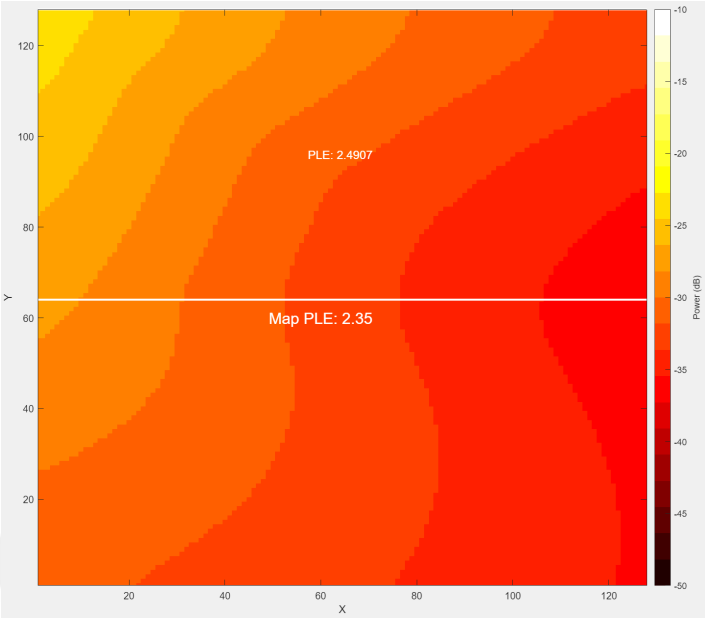

Figure 5.9. Generated two zone REM example: 4.

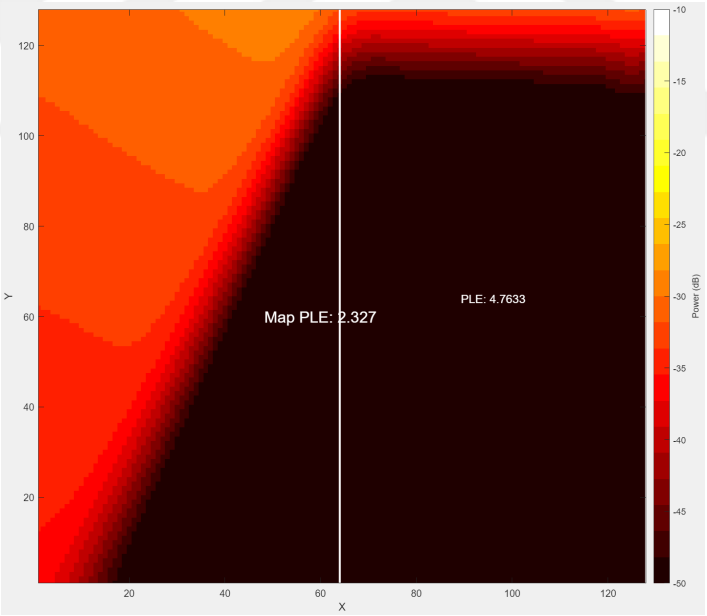

Figure 5.10. Generated two zone REM example: 5.

Now let us begin analyzing our examples on N zone REMs. In Figure 5.11 we see that there are three zones with different PLEs, two of them have similar PLE to the base PLE of the map, which is 2.8462. Despite having a similar PLE with 2.3795, the zone on the right sees a slight relief on the pressure of the received signal power. Meanwhile the zone at the center with PLE of 4.6788 creates a shadowing effect present from the

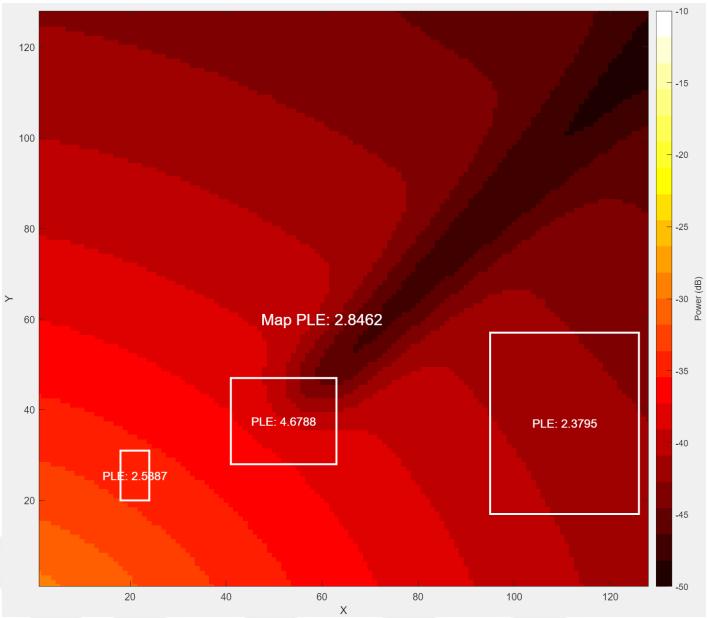

Figure 5.11. Generated N zone REM example: 1.

center of the map to the top right corner. This is a great example on how different structures within the area of interest can effect the propagation characteristics. That zone with high PLE could be a urban zone with tall buildings, could be a mountain or a forest.

In Figure 5.12 we see a similar effect to the Figure 5.11 where a high PLE zone creates shadowing, deeper we go into the high PLE zone, the signal strength drops faster. Left side of the zone with high PLE has a similar propagation characteristics to the base map, because it faces the PU, but the rate of signal power decline increases with the distance the signal covers within the high PLE zone.

The Figure 5.13-(a) shows five different zones, most important of them are two that is located at the center, and the one located at the top. In this figure, we clearly see that effects of shadowing can be cured in a relatively low PLE zone. The zone with PLE of 4.4973 creates a huge shadowing effect to the top right side of the map, but there are two zones which collides with this zone and the shadowing zone it creates, one with PLE of 3.2679 to the right of this high PLE zone, other with PLE of 3.2881 to the top of this zone. The zone on the right clearly creates a positive shadowing effect

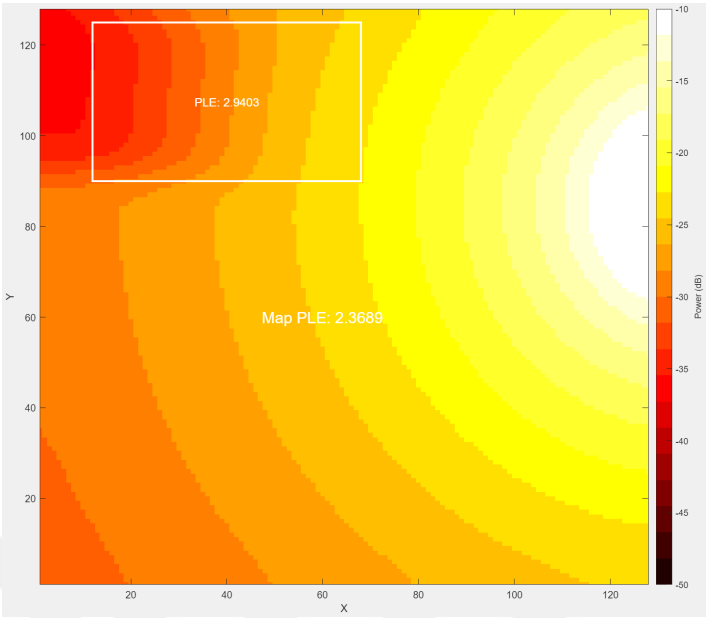

Figure 5.12. Generated N zone REM example: 2.

where the signal power is stronger, which is visible through a protrusion it creates to the top left of the high PLE zone. Meanwhile the zone at the top slightly corrects the angle of the circular color pattern which denotes the received signal power.

The same principle of negative shadowing can be seen in Figure 5.13-(b) where there is a relatively small zone of high PLE, but it still manages to completely degrade the received signal power in bottom side of the REM even when the location is far away from that zone.

The Figure 5.14 on the other hand, shows a zone of low PLE within a high PLE environment. As it can be seen in the same figure, this zone increases the signal strength within itself -relative to of those with the same distance to the PU but outside of that zone. This effect is still visible through to the bottom right of the map, there is a bulge of greater received signal power.

These examples are a tiny part of our 40.000 REM database, where we have a far more comprehensive DB, divided equally between two zone REMs and N zone REMs. We also store their metadata containing the location of the PU and its transmission

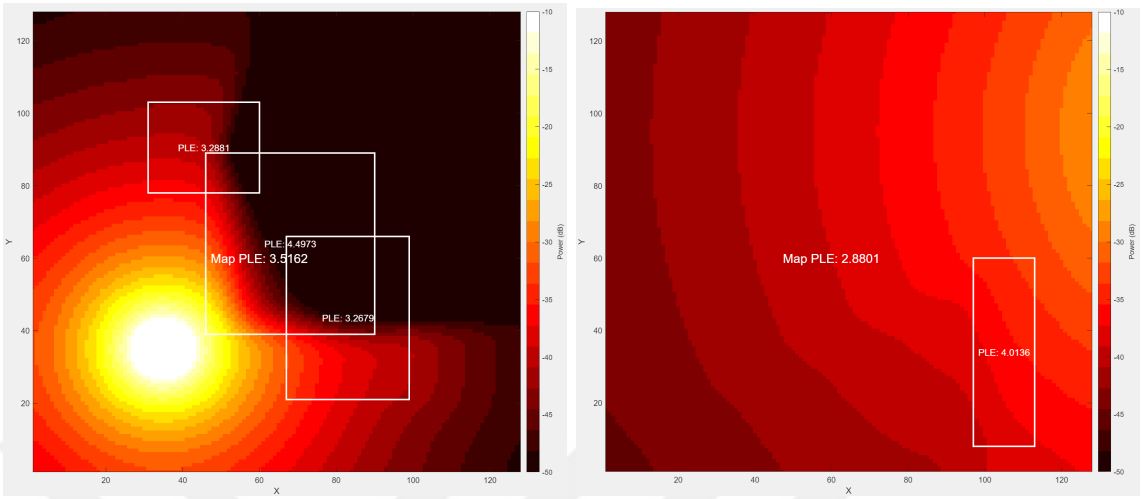

(a) (b)

Figure 5.13. Negative shadowing effects (a) generated N zone REM example: 3 (b) generated N zone REM example: 4.

characteristics, location and propagation characteristics of different zones within the map. Even though metadata is not used when training the model-we are only using the resulting REM and expecting our system to find different zones with only measurements from MCDs- they are useful to make comprehensive analysis on the results, which is discussed in Chapter 6. Now let us discuss how we are aiming to reconstruct the REMs we've created by only using the measurements from the MCDs.

5.2. REM Reconstruction

In this section, we will examine the methods we propose for REM generation. These methods can be categorized under two main approaches: *Single-Point Estimation* and *Full REM Construction*.

In the first approach, we aim to estimate a single point of the REM by using measurements taken from various other locations within the map. By applying this method iteratively across the entire area, each point of the REM can be estimated, thus enabling the estimation of the full REM. In the second approach, we utilize the measurements obtained from the original REM to directly train a model capable of

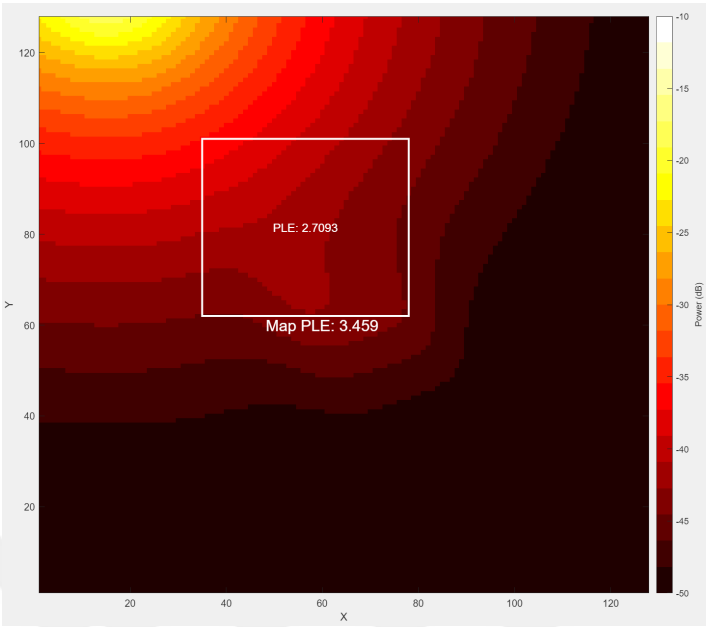

Figure 5.14. Generated N zone REM example: 5.

estimating the whole two-dimensional REM. Subsequently, we will evaluate the performance of the models produced by both approaches and determine which ones to proceed with in training. A detailed analysis of these selected models will be presented in the following section.

5.2.1. Single Point Prediction Approach

All of the proposed solutions examined under this heading focus on estimating the dB value at a selected point of the REM. A visualization of this method can be seen in Figure 5.15 where we have numerous MCDs (denoted by antenna symbols) and a point (denoted by p where $p = (x, y)$) that we are trying to predict the received signal power of. To achieve this, we are gathering the measurements from all the SUs and their locations, and feeding this information to our prediction engine along with the location of X, then we are predicting its received signal power.

To achieve this, various neural network architectures have been developed. The first of these architectures can be observed in Figure 5.16. In this figure, x and y represent an array of coordinates of MCDs, dB represents the measured signal power

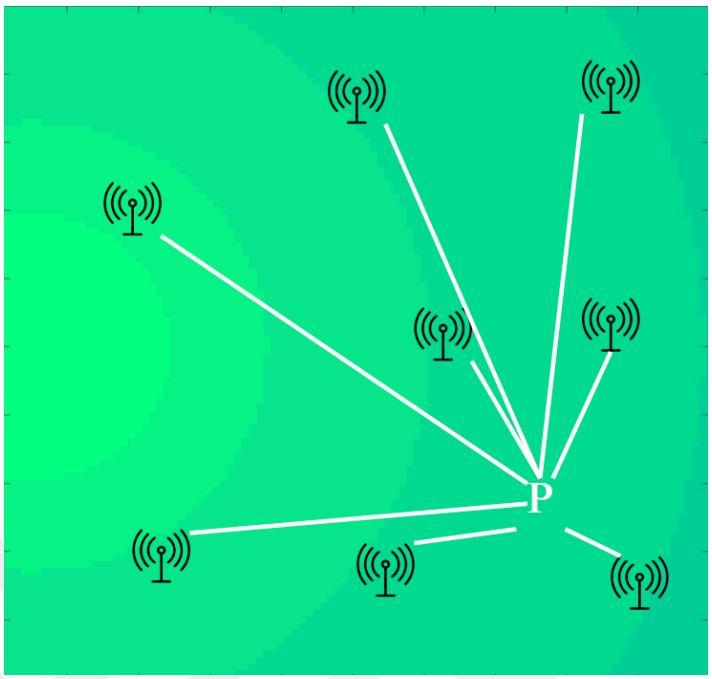

Figure 5.15. Point prediction example.

at these coordinates. This architecture represents the simplest design among those we developed. By combining different types of layers, training decay rates, and dropout layers within this architecture, more than twenty distinct neural networks were trained.

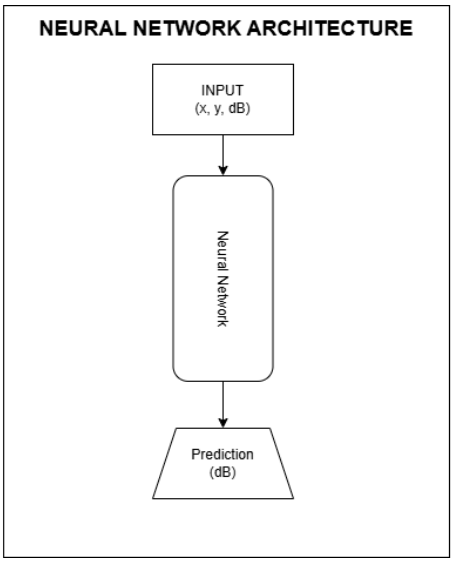

Figure 5.16. Neural network architectures: simple sequential network.

The input layer shown in Figure 5.16 receives a matrix with a width of three. The length of this matrix varies depending on the number of measurements conducted. In our initial training experiments, measurements were taken from a total of 15 points, and for each point, the matrix included the corresponding X and Y coordinates along with the measured dB value. Additionally, the X and Y coordinates of the target point to be estimated were appended to the end of the matrix, with the corresponding dB value set to a constant of -1. This setup enabled the neural network to output the estimated dB value for the given X and Y coordinates. Under these conditions, the input matrix provided to the neural network had dimensions of $(16, 3)$.

Following the training sessions, we increased the number of measurement points from 15 to 31 in order to better assess the relation between the number of measurement points and overall system success. Despite increasing our input size by two folds, we are still trying to reconstruct a REM by measuring only 1/512 of it, which is still challenging. Accordingly, the input layer matrix size of the neural network was set to $(32, 3)$. In this configuration, a noticeable reduction in error was observed. To compare these two scenarios, we designed a simple neural network composed solely of Dense layers. This network consists of four layers: the first and last Dense layers have a size of 64, while the two intermediate Dense layers have a size of 256. The rectified linear unit (ReLU) was employed as the activation function. The Adam optimizer was used with a learning rate of 10^{-7} and a weight decay of 10^{-8}. We also set the batch size to 64 and the number of epochs to 5000. In doing so, we aim to ensure that, despite the low learning rate, the training process can still converge effectively and yield reliable results.. For this and all subsequent network designs mentioned, the loss values were calculated using the mean squared error (MSE). The error rates observed under these conditions are presented in Table 5.1.

After obtaining these results, although the error rates had decreased by 56%, they still remained far from the desired level. As a first step, we decided to increase the number of layers within the same architecture. Instead of a four-layer network with intermediate layer sizes of 256, we designed a deeper network comprising ten layers,

Table 5.1. Input size comparison results.

$(16, 3)$ **Input Train Loss**	$(16, 3)$ **Input Validation Loss**
32.397	36.935
$(32, 3)$ **Train Loss**	$(32, 3)$ **Validation Loss**
18.398	19.663

with intermediate layer sizes reaching 4096. ReLU was again used as the activation function. The exact architecture of this network is as follows: Dense(64), Dense(256), Dense(1024), Dense(4096), Dense(16384), Dense(16384), Dense(4096), Dense(1024), Dense(256), Dense(64).

By widening the intermediate layers in this configuration, our goal was to enable the neural network to recognize more subtle variations—such as changes in the PLE—that may be difficult to detect. Upon training this architecture with our dataset, we obtained the results shown in Table 5.2. While these results represented a notable improvement over the previous ones, they still fell short of our target performance, prompting us to develop new architectural approaches.

Table 5.2. Bigger sequential network results.

Train Loss	**Validation Loss**
12.613	14.178

Once we confirmed that the $(32, 3)$ input structure provided both sufficiently low computational cost and satisfactory accuracy, we proceeded to develop additional architectures and conducted comparisons based on this measurement configuration. One such architecture we proposed is illustrated in Figure 5.17. In contrast to our previous neural network, which utilized a single input layer, this model employs four separate input layers. The inputs to these four layers were designed as follows:

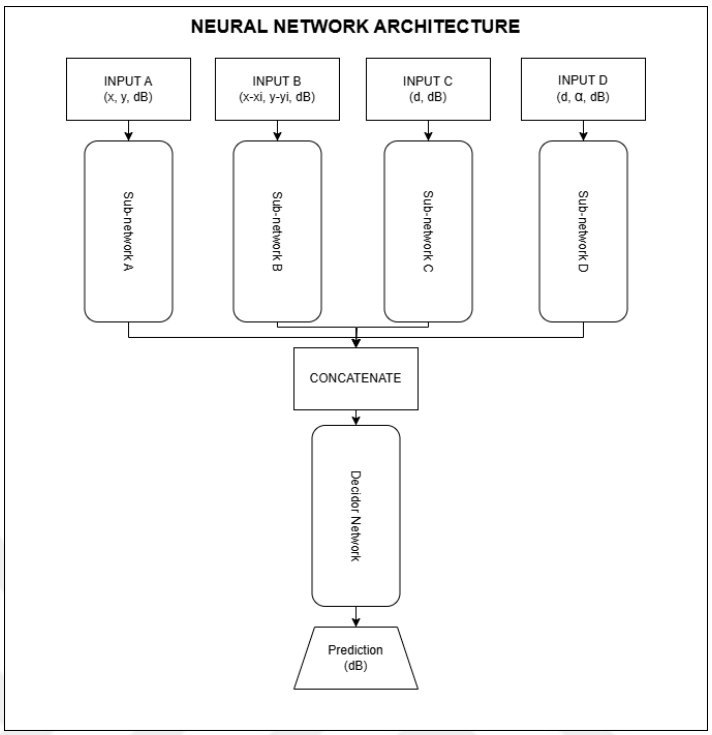

Figure 5.17. Neural network architectures: non-sequential network.

- Input A layer: Similar to the initial setup, this layer receives the coordinates and corresponding measurements of 31 reference points, with the coordinates of the target (to-be-predicted) point appended to the end of the matrix.
- Input B layer: Instead of absolute coordinates, this layer receives the relative coordinates of the 31 reference points with respect to the target point, along with the measurement values at those points. The coordinates of the target point are not appended in this case.
- Input C layer: This layer receives the Euclidean distances from each of the 31 reference points to the target point, in addition to the measurement values at those points.
- Input D layer: In addition to the distances used in Input C, this layer incorporates the angular information between each reference point and the target point, enabling the computation of the distances as vectors.

While designing the sub-networks within each of the four branches of this network, we adopted a structure similar to that of the previous architecture; however, the number

of intermediate layers was reduced. As a result, each sub-network was configured as follows: Dense(64), Dense(256), Dense(1024), Dense(4096), Dense(4096), Dense(1024), Dense(256), Dense(64).

For the decider network, which combines the outputs of the four branches, a more compact architecture was selected. This network consists of the following layers: Dense(4), Dense(16), Dense(64), Dense(256), Dense(256), Dense(64), Dense(16), Dense(4).

This newly developed architecture was observed to perform significantly more effectively than the previous one. Although the number of parameters was reduced from 411 million to 103 million, the network still achieved the results presented in Table 5.3. Despite offering considerable improvements over earlier outcomes, these results still fall short of the performance level we aim to reach.

Table 5.3. Non-sequential network results.

Train Loss	**Validation Loss**
10.519	11.496

After designing this architecture, we decided not only to diversify the input structure of the neural network to improve prediction accuracy, but also to avoid directly estimating the output in terms of dB. Instead, we chose to insert a custom-designed mathematical layer into the network. The first method we experimented with under this approach was to implement a network that replicates the Inverse Distance Weighting (IDW) algorithm. The IDW algorithm can be expressed as

$$\begin{aligned} \hat{z}(p) &= \frac{\sum_{i=1}^{n} w_i z_i}{\sum_{i=1}^{n} w_i} \\ w_i &= |p - p_i|^{-\beta} \\ p &= (x, y) \end{aligned} \tag{5.6}$$

where w_i denotes the distance weight, z_i denotes the actual value of p_i, and $\hat{z}(p)$ denotes the calculated power at p.

As shown in the Equation (5.6), a value for β must be determined in order to compute the IDW and we call it IDW-β. In the architecture illustrated in Figure 5.18, the objective was to estimate the β parameter at the output of the Decider Network and, using the measurement locations and values provided in Input A, calculate the signal strength at the target location via the IDW algorithm. In this architecture, the previously described network structure was preserved entirely, with the only modification being the addition of an IDW layer to the end of the Decider Network.

Although training was conducted using the same number of epochs and the same batch size, incorporating this custom layer increased the training time by up to a factor of 17. Moreover, because this method involves predicting an exponential value, we frequently encountered the Exploding Gradient Problem during training. This issue typically arises when training occurs on a highly steep error surface and the step size is not well-suited to the surface characteristics [63]. In our case, the problem was exacerbated by the nature of the exponential values involved—small variations in the β estimate could lead to disproportionately large shifts in the output, even resulting in NaN values.

A key contributor to this instability was our continued use of the ReLU activation function. By switching to a bounded activation function such as the sigmoid, we were able to constrain the predicted β within a specific interval, thereby reducing the risk of exploding gradients. Although this resolved the gradient instability, it also led to more constrained and suboptimal predictions. In this configuration, we set the range of the β parameter to $(1, 10)$, and the results obtained from this training setup are presented in Table 5.4. The reason for worse results in this model is the instability of the predictions despite setting a range to the β value.

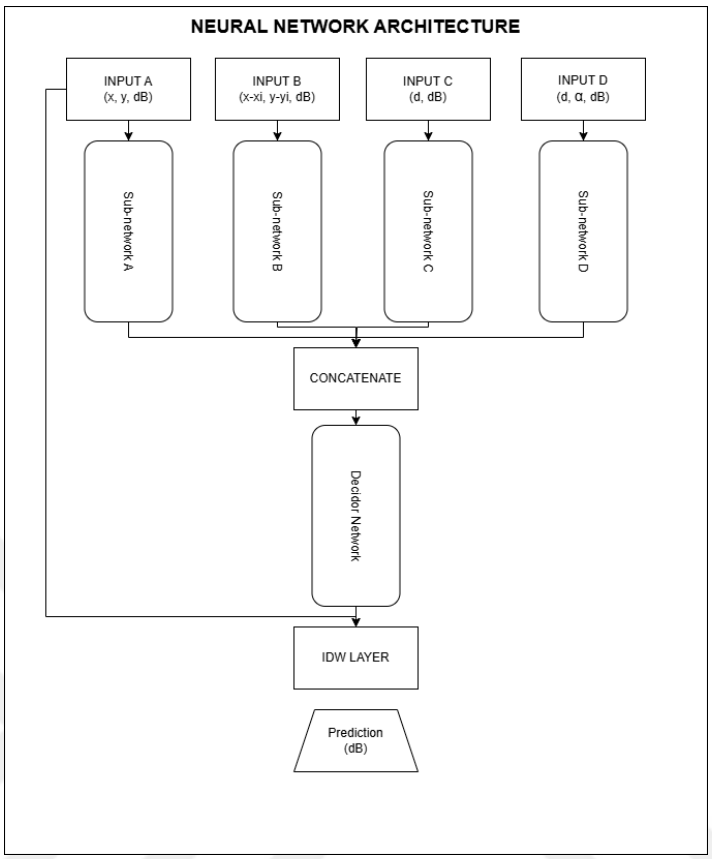

Figure 5.18. Neural network architectures: IDW layer network.

Table 5.4. IDW network results.

Train Loss	**Validation Loss**
18.731	22.527

Since the results from the previous step did not meet our expectations, we replaced the IDW Layer with a Friis Layer, which implements the Friis Transmission Equation as shown in Equation (3.1). Naturally, this required more substantial modifications to our network architecture. The updated neural network design is illustrated in Figure 5.19.

We restructured the earlier four-branch network architecture to align with a decomposition of the Friis equation into three distinct components. In this new design, each sub-network is tasked with estimating a specific term from the equation:

- Sub-network A is responsible for predicting the path loss exponent n.
- Sub-network B estimates the value of $\frac{\lambda}{4\pi d}$.
- Sub-network C predicts the term $P_t G_t G_r$, which encompasses the transmitted power and the gains of the transmitting and receiving antennas.

These three values are then used within the Friis Layer to compute the received signal power in dB.

By removing the previously used decider network and adopting this modular structure, the total number of parameters was reduced to 77 million. The corresponding performance results can be seen in Table 5.5.

However, even with this approach, we were unable to fully resolve the Exploding Gradient Problem encountered earlier. We identified the primary cause as the simultaneous prediction of exponential terms and multiplicative coefficients, both of which are sensitive to even minor variations during training. To mitigate this, we employed sigmoid activation functions for all three sub-networks and introduced value constraints for each predicted parameter:

The PLE n was restricted to the range $(1, 10)$. The distance-dependent coefficient $\frac{\lambda}{4\pi d}$ was bounded between $(0, 1)$. The gain-related term $P_t G_t G_r$ was limited to the range $(1, 10000)$. Despite these constraints and the increased training time, we still observed significant fluctuations during training, indicating persistent instability in the learning process.

Table 5.5. Friis network results.

Train Loss	Validation Loss
11.694	17.931

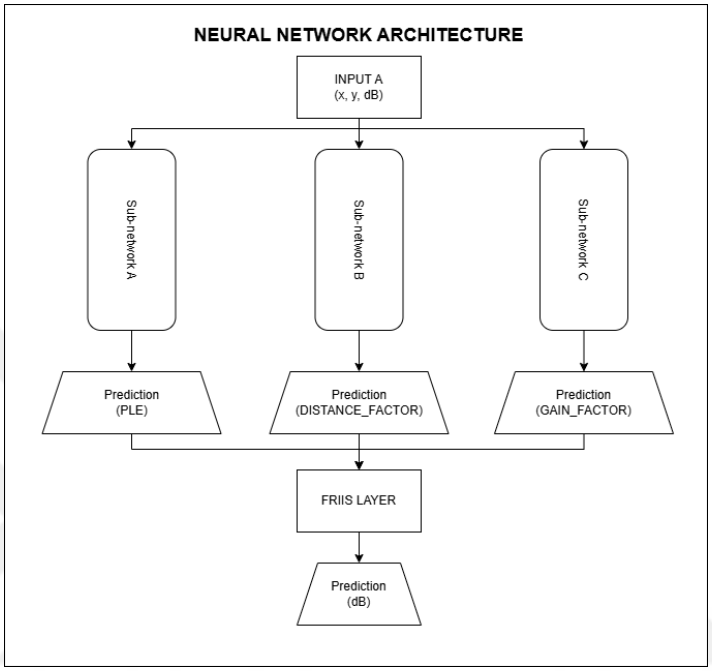

Figure 5.19. Neural network architectures: Friis layer network.

5.2.2. Entire REM Prediction Approach

All of the proposed solutions discussed under this section are designed to estimate the entire Radio Environment Map (REM) simultaneously. We will examine two different architectures in this context, namely *the Simple Sequential Generator Network* and *the IDW Input Sequential Generator Network*.

The first approach is illustrated in Figure 5.20. Architecturally straightforward, this model is an adaptation of the network previously shown in Figure 5.16. Two key modifications were made:

- The coordinate of the prediction point was removed from the input layer, as the goal is now to generate the entire map rather than a single location.

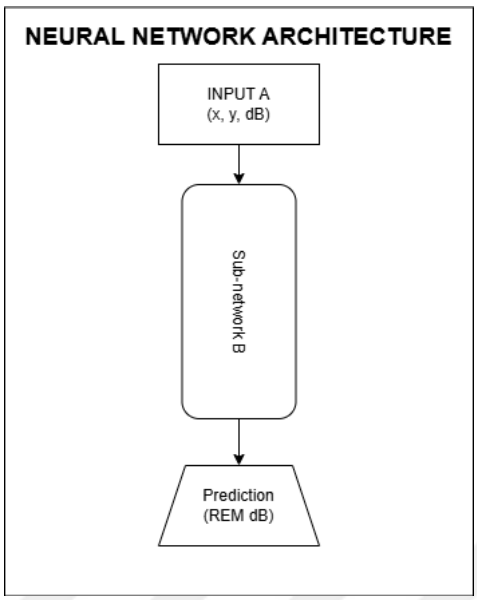

Figure 5.20. Neural network architectures: simple sequential generator network.

Table 5.6. Simple generator network results.

Train Loss	**Validation Loss**
7.173	8.671

- The output layer was redesigned to predict an entire REM with a resolution of $(128, 128)$ units, rather than outputting a single value.

Since the network now produces a multidimensional output instead of a single scalar, it was no longer appropriate to progressively reduce the layer sizes. Instead, the architecture was adjusted so that the final layer matches the dimensions of the target REM. Accordingly, the following network configuration was adopted: Dense(64), Dense(256), Dense(1024), Dense(4096), Dense(16384).

By setting the final layer size to 16,384—equivalent to the flattened size of a $(128, 128)$ grid—the network is enabled to directly generate the desired map. The results obtained using this architecture are presented in Table 5.6, and they indicate a notable improvement over previous approaches, bringing the performance closer to the desired level.

The second method was developed to enhance the performance of the first approach. The overall architecture is depicted in Figure 5.21. In this design, before passing any input to the neural network for prediction, a preliminary map is generated using the IDW algorithm. This IDW-generated map is then provided as an input to the network, which is expected to refine and improve upon this initial estimation through learning.

The second method relies on the use of a β parameter, as defined earlier in Equation (5.6). Therefore, selecting the optimal β value is a crucial step. To determine this, a series of simple neural networks were trained using $1 \leq \beta \leq 9$. β value that yielded the best performance in these simpler models was then used in training more complex architectures.

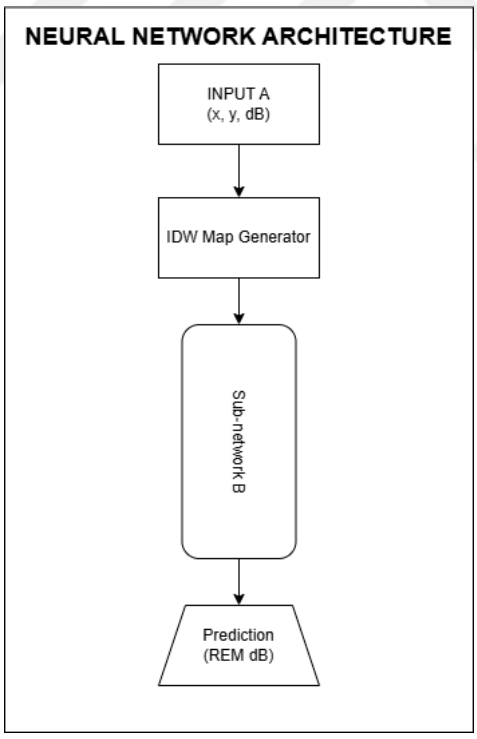

Figure 5.21. Neural network architectures: IDW input sequential generator network.

The neural network employed for this selection process was structured as follows: Dense(16384), Dense(1024), Dense(64), Dense(1024), Dense(16384). This model, consisting of approximately 34 million parameters, was trained separately for each of the 9

Table 5.7. Different β value results.

	$\beta = 1$	$\beta = 2$	$\beta = 3$	$\beta = 4$	$\beta = 5$	$\beta = 6$	$\beta = 7$	$\beta = 8$	$\beta = 9$
MSE	11.492	6.542	4.712	4.271	4,183	4,181	4.206	4,241	4.276

different β values. The resulting performances were compared, and the most appropriate β value was selected accordingly. The outcomes of these comparisons are presented in Table 5.7.

As observed in the results, selecting $\beta > 6$ leads to a decline in performance. Moreover, increasing it beyond 5 does not provide significant additional benefit. Therefore, for all subsequent experiments, the β value is fixed at 5.

Given that this method yielded better training results even with a relatively shallow neural network, we decided to continue by training various neural architectures based on the same approach. To further explore the effectiveness of this method, three different neural networks were developed.

The first of these is referred to as the main network, and it follows the architecture: Dense(16384), Dense(4096), Dense(1024), Dense(256), Dense(64), Dense(64), Dense(256), Dense(1024), Dense(4096), Dense(16384). This model comprises approximately 408 million parameters. The design objective here is to extract meaningful features from the IDW-based input in the early layers, and then reconstruct the REM using those features in the later layers.

The second network retains a similar number of layers but significantly increases the width of each, aiming to leverage larger parameter capacity in the middle layers to produce a more refined REM output. The architecture of this model is as follows: Dense(16384), Dense(16384), Dense(4096), Dense(4096), Dense(1024), Dense(1024), Dense(1024), Dense(1024), Dense(4096), Dense(4096), Dense(16384), Dense(16384). This model contains roughly 716 million parameters.

The third and final network is based on the same architecture as the Main Network but incorporates a 20% Dropout layer. The rationale behind this modification is to reduce variance in predictions and improve generalization by preventing overfitting, thereby aiming for a network with lower standard deviation in its outputs.

The training and validation accuracies of these neural networks are presented in Table 5.8. In the following section, the performance of these models on REMs that were not included in either the training or validation datasets will be analyzed. These results will be compared against the IDW algorithm, and evaluated from various perspectives.

Table 5.8. Three IDW networks training comparison.

Main Network	
Training Error	**Validation Error**
0.1814	1.2088
Bigger Network	
Training Error	**Validation Error**
0.4015	37.1448
High Dropout Network	
Training Error	**Validation Error**
1.2298	3.0940

6. PERFORMANCE EVALUATION AND DISCUSSION

In this section, the performance of the three networks selected for further evaluation, as described in Chapter 5, will be assessed in comparison to the IDW algorithm, which will serve as the benchmark method. These three networks will hereafter be referred to as the Main Network, the Dropout Network, and the Big Network, respectively.

6.1. Visual Results

First, let us select a REM that was previously generated. As illustrated in Figure 6.1-(a), the REM consists of two distinct regions: for $x < 64$, the PLE value is low, whereas for $x \geq 64$, the PLE value is set significantly higher. In this specific scenario, the PU is located outside the map at the coordinates $(28, -85)$. Considering these conditions, the shadowing effect caused by the high PLE region starting at $x = 64$ is clearly observable in the range $64 < x < 80$.

Now, let us examine how the IDW algorithm performs on this REM. As shown in Figure 6.1, the predictions of the IDW method become more accurate as the β value increases. In the same figure, the distinct spots visible in the REMs generated by IDW correspond to the measurement points used in the original REM.

The prediction errors of the REMs produced by IDW are illustrated in Figure 6.2 in terms of dB, and in Figure 6.3 as percentage errors. In both visualizations, dark blue indicates regions of low error, while dark red signifies high error. When calculating the error in dB, the absolute difference between the predicted and actual values was taken.

So, how do our previously introduced algorithms actually perform? As illustrated in Figure 6.4, unlike IDW, all three methods are able to easily capture the overall structure of the original REM. Compared to the Main Network, which only includes

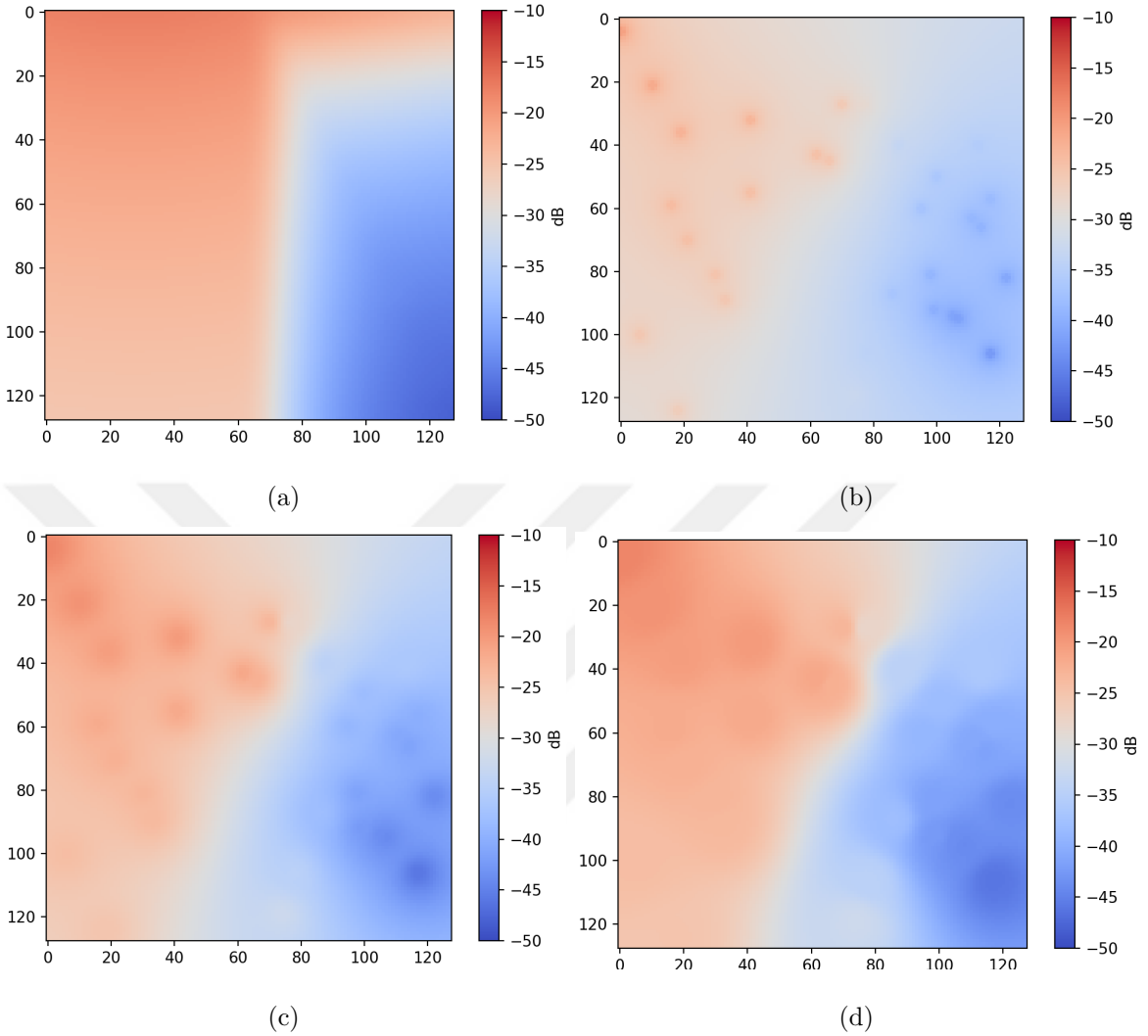

Figure 6.1. (a) Original REM (b) IDW, $\beta = 1$ (c) IDW, $\beta = 2$ (d) IDW, $\beta = 3$.

weight decay, the Big Network and the Dropout Network (which incorporates a dropout rate of 0.2) tend to produce noisier results. As shown in Figure 6.5, even the less successful algorithms reduce the error levels of IDW - which can reach up to 12 dB - to below 6 dB, while the best-performing algorithm reduces this difference to under 3 dB. Similarly, considering the percentage errors previously discussed, Figure 6.6 reveals that our methods reduce the IDW error rates, which can exceed 150%, to approximately 50%.

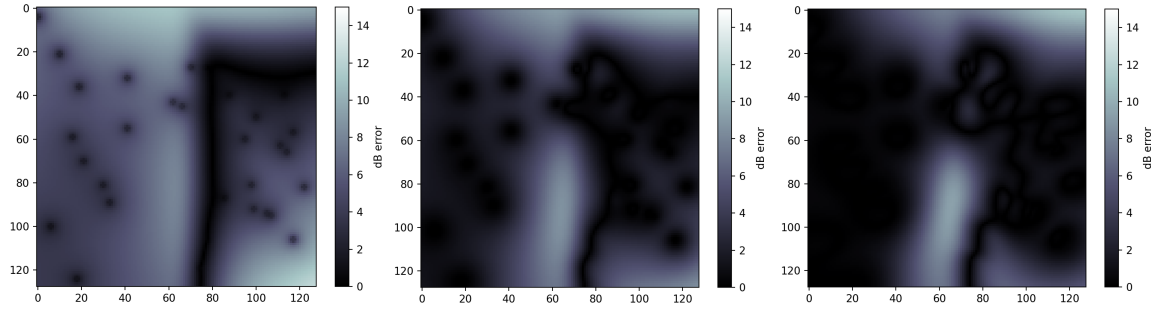

(a) (b) (c)

Figure 6.2. Errors in dB (a) IDW, $\beta = 1$ (b) IDW, $\beta = 2$ (c) IDW, $\beta = 3$.

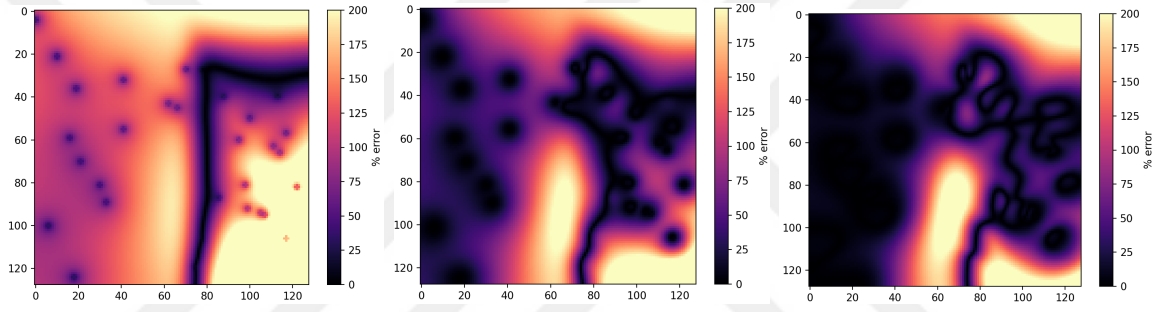

(a) (b) (c)

Figure 6.3. % Errors (a) IDW, $\beta = 1$ (b) IDW, $\beta = 2$ (c) IDW, $\beta = 3$.

6.2. Numeric Results

Although these visual results may create the impression that our algorithms consistently outperform IDW in all cases, this is not entirely accurate. Among the three previously defined algorithms, those other than the Main Network are numerically outperformed by IDW, particularly at higher β values. Despite this, their predictions appear to be more successful, as they better capture the structural characteristics of the REMs to be estimated.

To better assess these results, a total of 442 REMs were generated, and measurements were conducted at 32 distinct points on these REMs. Using these measurements, IDW interpolations were performed, and MSE values are presented in Table 6.1. As shown, increasing the β parameter in the IDW method leads to a reduction in error rates; however, this improvement quickly reaches a plateau.

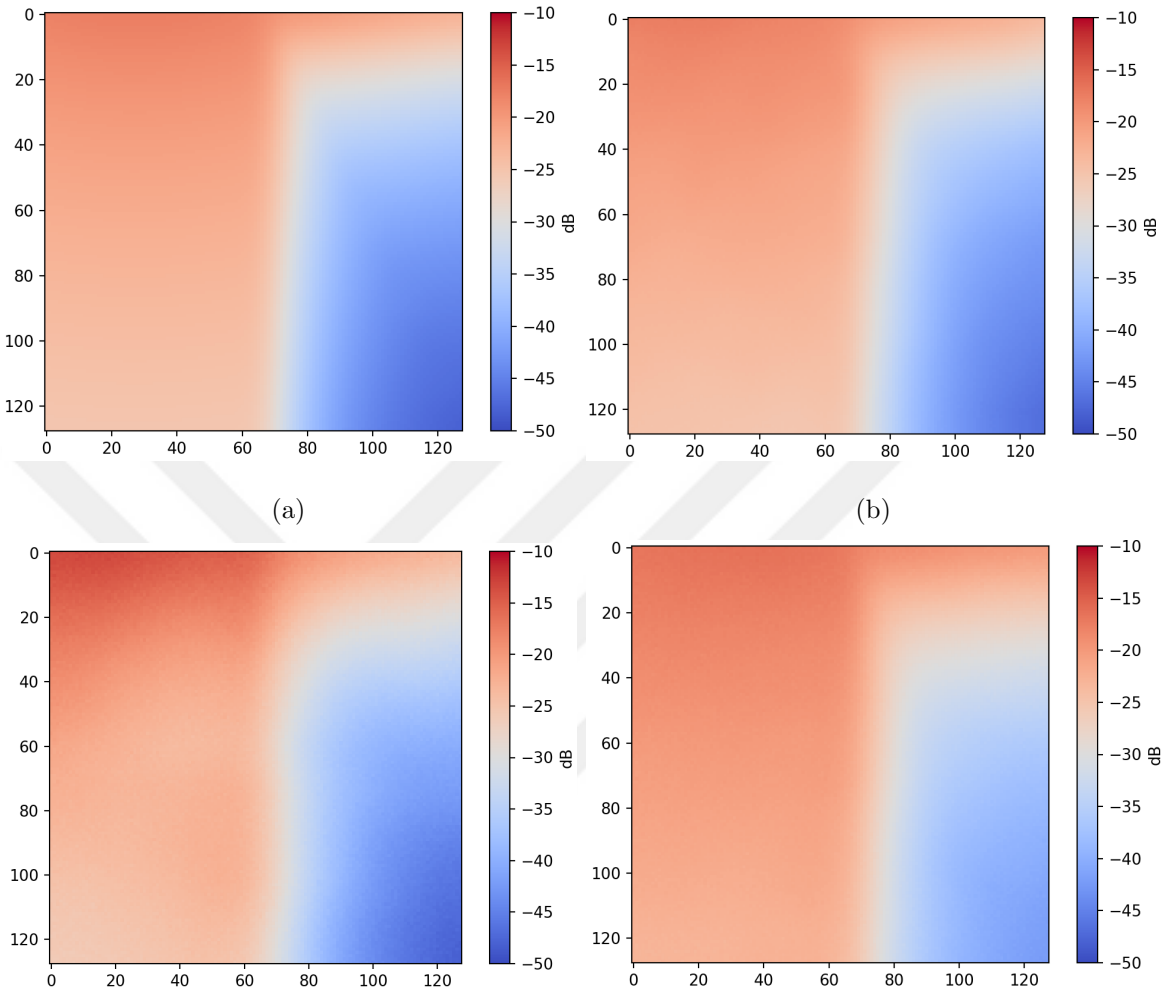

Figure 6.4. (a) Original REM (b) main network (c) dropout network (d) big network.

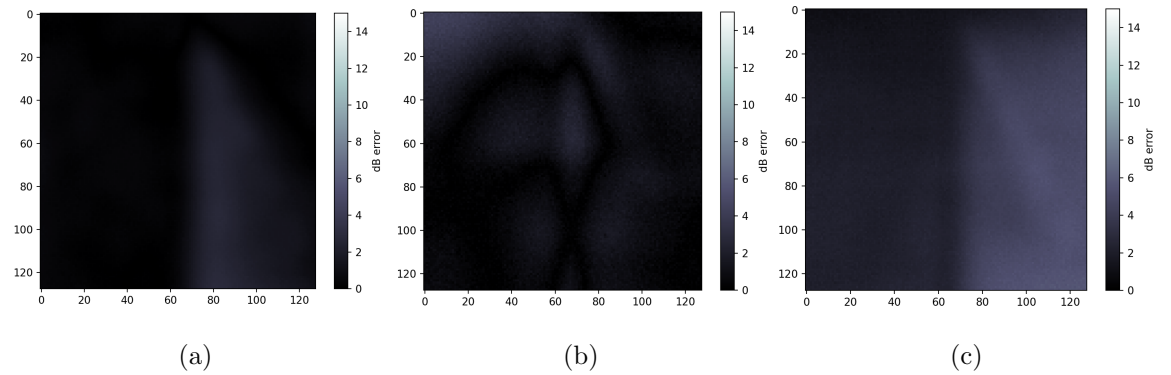

Figure 6.5. Errors in dB (a) main network (b) dropout network (c) big network.

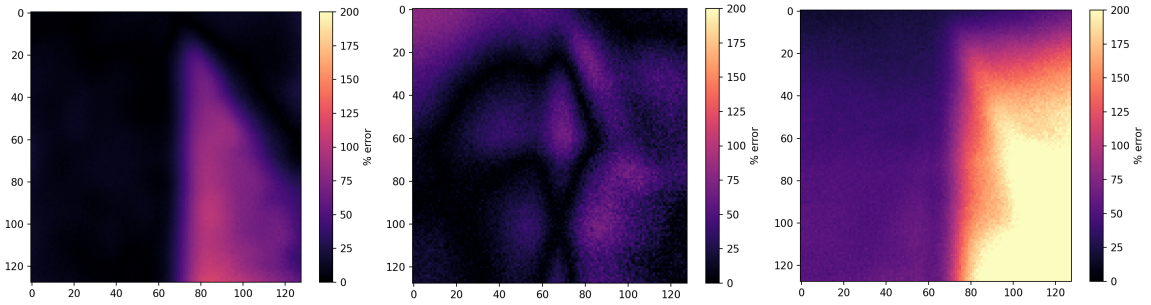

(a) (b) (c)

Figure 6.6. % Errors (a) main network (b) dropout network (c) big network.

Table 6.1. IDW results.

	$\beta = 1$	$\beta = 2$	$\beta = 3$	$\beta = 4$	$\beta = 5$
dB	3.397	1.935	1.398	1.263	1.234
σ**(dB)**	1.719	1.026	0.768	0.697	0.676
MSE	22.208	9.763	6.272	5.319	5.067
σ**(MSE)**	20.503	10.077	7.344	6.595	6.417

Table 6.2. Algorithm results.

	Main Network	**Dropout Network**	**Big Network**
dB	1.115	1.647	5.371
σ**(dB)**	0.946	0.755	2.646
MSE	3.828	7.354	38.677
σ**(MSE)**	8.973	7.115	33.423

The MSE performance of our custom-developed algorithms is presented in Table 6.2. The Main Network algorithm consistently outperforms IDW in all scenarios. In contrast, the Dropout Network algorithm is outperformed by IDW when the parameter β reaches 3 or higher. The Big Network algorithm, on the other hand, suffers from data and training limitations due to the lack of sufficient resources and feasibility for training, and therefore fails to surpass IDW at any value. These findings highlight

Table 6.3. IDW results: two-region REM.

	$\beta = 1$	$\beta = 2$	$\beta = 3$	$\beta = 4$	$\beta = 5$
dB	4.195	2.377	1.672	1.480	1.430
σ**(dB)**	1.309	0.741	0.568	0.523	0.507
MSE	27.780	11.897	7.369	6.065	5.674
σ**(MSE)**	15.757	7.035	5.114	4.644	4.537

Table 6.4. IDW results: multi-region REM.

	$\beta = 1$	$\beta = 2$	$\beta = 3$	$\beta = 4$	$\beta = 5$
dB	2.614	1.500	1.129	1.050	1.041
σ**(dB)**	1.712	1.080	0.841	0.776	0.761
MSE	16.734	7.678	5.204	4.595	4.478
σ**(MSE)**	22.958	11.975	8.869	7.985	7.780

that increasing the size of a neural network does not necessarily lead to improved performance, emphasizing the importance of balanced and efficient design in algorithm development.

As previously mentioned, the REM database we constructed consists of two types of data. In the first type, the maps are divided into two halves, each region with a distinct PLE value; in the second type, a random number of regions are generated at random locations within the maps. We refer to the former as two-region REMs and the latter as multi-region REMs. This distinction allows us to compare the performance of both the IDW method and our proposed algorithms under different conditions.

As shown in Table 6.3, it is evident that all IDW results have deteriorated compared to those in Table 6.1. The lower standard deviation combined with a higher average error suggests that IDW more frequently produces larger errors. In contrast, this trend is reversed in the results presented in Table 6.4. Here, IDW performs better than in Table 6.1, indicating improved overall accuracy; however, the higher standard

Table 6.5. Algorithm results: two-region REM.

	Main Network	**Dropout Network**	**Big Network**
dB	0.757	1.178	3.085
σ**(dB)**	0.369	0.281	0.653
MSE	1.268	2.839	11.655
σ**(MSE)**	1.179	1.367	4.641

Table 6.6. Algorithm results: multi-region REM.

	Main Network	**Dropout Network**	**Big Network**
dB	1.467	2.106	7.605
σ**(dB)**	1.179	0.791	1.824
MSE	6.343	11.768	65.094
σ**(MSE)**	12.0614	7.674	27.865

deviation implies the presence of significant outliers, meaning that despite the generally good performance, the method still yields very poor results in extreme cases.

In the case of our custom-developed algorithms, the opposite trend is observed. As shown in Table 6.5, the results are noticeably better than those in Table 6.2. Additionally, the lower standard deviations indicate that the algorithms yield more consistent and reliable performance. However, the results in Table 6.6 tell a different story: both the error rates and standard deviations are higher. This suggests that although the algorithms occasionally produce highly accurate predictions, they tend to make larger errors more frequently. Given that our dataset is evenly split between Two-Region and Multi-Region REMs, the algorithms perform more effectively on the simpler Two-Region cases. At the same time, this highlights an increased likelihood of error in the more complex Multi-Region cases, where the number of possible configurations is significantly greater.

6.3. Further Analysis

Considering all these factors, it becomes evident that comparing only the average results is insufficient. The performance of the developed algorithms requires more comprehensive analysis. Several additional aspects should be taken into account when evaluating algorithmic performance: How does the distribution of MCDs—that is, the spatial arrangement of the measurement points—affect the results? Which method benefits more from a uniformly distributed set of MCDs across the entire map? How effectively can densely deployed MCDs capture the structural characteristics of the map? Furthermore, how does the location of the PU influence the outcomes? Does the presence of the PU within the mapped REM offer any advantage? Does the distance of the PU to the REM area affect which algorithm performs better? Let us now address these questions in detail.

Now, let us address the distribution of MCDs. We consider that there will be three different types of distribution: uniformly distributed MCDs, clustered MCDs, and concentrated MCD distribution.

Uniformly distributed MCDs are expected to be spread evenly throughout the environment, with relatively similar distances between them. Clustered MCDs are positioned close to each other within groups, while the distribution among the groups is approximately uniform. Concentrated MCD distribution refers to a situation where almost all MCDs are located near each other.

In Figure 6.7 we can see four examples of MCD distributions, Figure 6.7-(a) shows a random distribution of MCDs, this was previously used by algorithms to reconstruct the REM. Figure 6.7-(b) shows MCDs densely distributed where there are no MCDs at the top and right of the map and most of the MCDs are located at the center of the environment. Figure 6.7-(c) shows four clusters of MCDs where they are close to each other within the clusters, but clusters itself are evenly distributed. Figure 6.7-(d) shows MCDs evenly distributed through the environment.

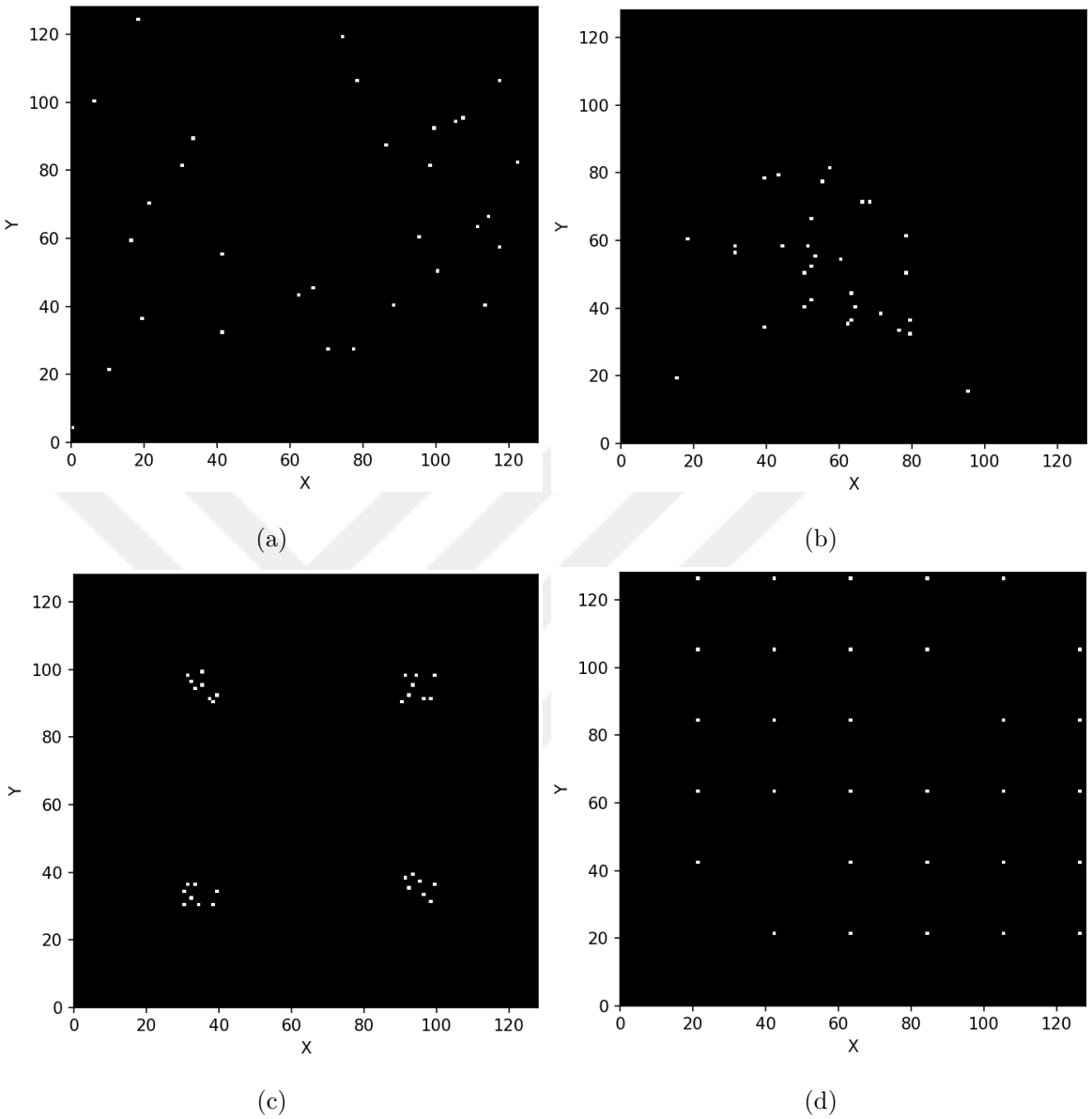

Figure 6.7. (a) Random MCD distribution (b) dense MCD distribution (c) cluster MCD distribution (d) even MCD distribution.

Now, let us define the error rates for different β values in each of the given measurement point selections. As it can be seen in Table 6.7 even distribution of MCDs is crucial for REM prediction using IDW algorithm with various β values. For all β values, ranking these three distributions stay the same with even distribution perform the best, clustered distribution comes the second, and densely packing the MCDs is the worst performing distribution.

Table 6.8. Analysis of algorithm behavior.

	Evenly Distributed MCDs	**Clustered MCDs**	**Densely Packed MCDs**
Main, MSE	2.714	2.562	6.421
Main, σ	6.192	6.081	11.168
Dropout, MSE	4.356	3.937	9.718
Dropout, σ	5.009	6.721	11.231
Big, MSE	22.914	24.154	46.406
Big, σ	23.513	19.347	43.807

Table 6.7. Analysis of IDW behavior.

	Evenly Distributed MCDs	**Clustered MCDs**	**Densely Packed MCDs**
$\beta = 1$, **MSE**	20.496	24.733	46.740
$\beta = 1$, σ	19.275	21.403	44.214
$\beta = 2$, **MSE**	6.744	16.038	38.837
$\beta = 2$, σ	7.654	15.527	36.998
$\beta = 3$, **MSE**	3.523	13.709	33.504
$\beta = 3$, σ	4.926	14.759	32.582
$\beta = 5$, **MSE**	3.002	13.229	28.020
$\beta = 5$, σ	4.518	15.081	28.168

In Table 6.8 on the other hand, shows the opposite for our Main Network and Dropout Network algorithms where Clustered Distribution causes slightly better predictions compared to the Even Distribution. This is mainly because of our database distribution where we have 20.000 two zone REMs and 20.000 N zone REMs. Clustered Distribution is clearly better at detecting two zone REMs and its characteristics, whereas it fails to perform on the same level for N zone REMs. Even distribution on the other hand, perform nearly the same for these two REM types. This leads to Clustered Distribution outperforming Even Distribution. In the case of Big Network algorithm, Even Distribution is better than the Clustered Distribution, but has a higher standard deviation.

Now let us visualize these results. We will visualize these results under three subsections, in Subsections 6.3.1, 6.3.2, 6.3.3 we will address MCD location distributions and its effect on REM generation. In order to keep our analysis compact, we will analyze IDW algorithm in four different cases where β is 1,2,3 and 5. First let us remind ourselves the original REM that we are trying to estimate. In Figure 6.8 we can see the original REM.

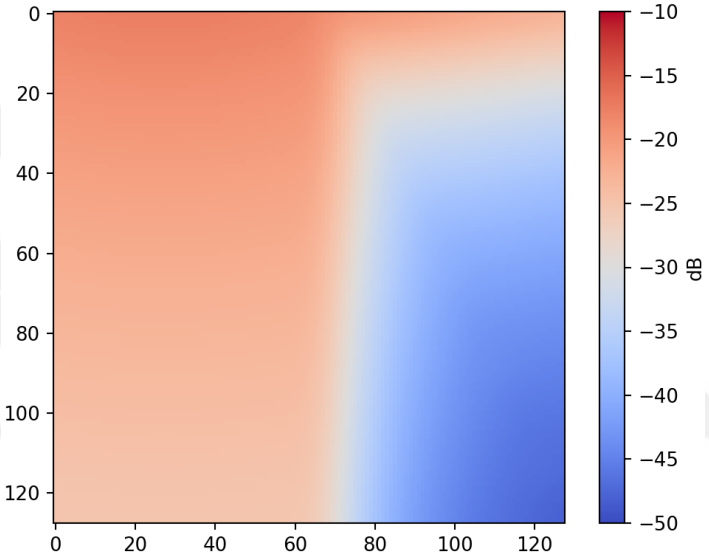

Figure 6.8. Original REM.

6.3.1. Clustered Location Analysis

This subsection is dedicated to analyzing clustered distribution and its effects on the REM generation. To start this analysis we must first discuss how the predefined IDW algorithm works on different β values and with different distributions. In Figure 6.9-(a), we can see the locations of the MCDs clearly, and in Figure 6.9-(b), we can see that our dB error rate exceeds 10 in $x > 110, y > 110$ zone and Figure 6.9-(c) supports this by showing in the $x > 64$ side of the map, we fail to capture the change in the signal power where we mostly see error rates above 200%.

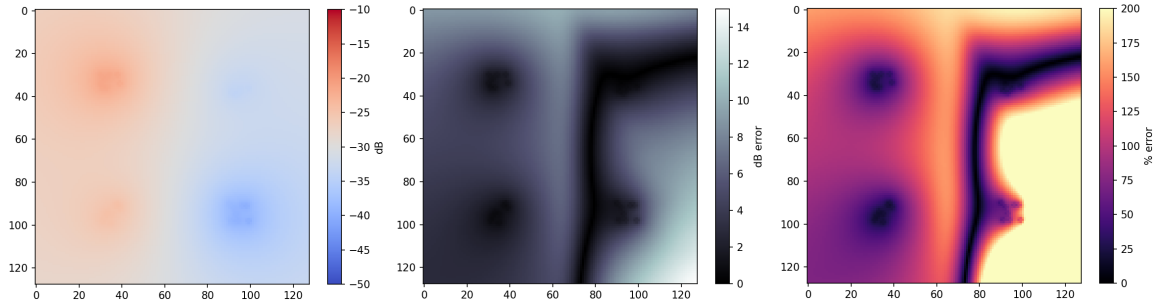

(a) (b) (c)

Figure 6.9. (a) $\beta = 1$ generated REM (b) dB error (c) % error.

In Figure 6.10-(a), the generated REM gets clearly softer and predict higher values, this trend continues Figure 6.10-(b), we can see that high error rates in $x > 110, y > 110$ zone get flattened out and Figure 6.10-(c) shows this improvement mostly in $80 < x < 100, 40 < y < 60$ zone.

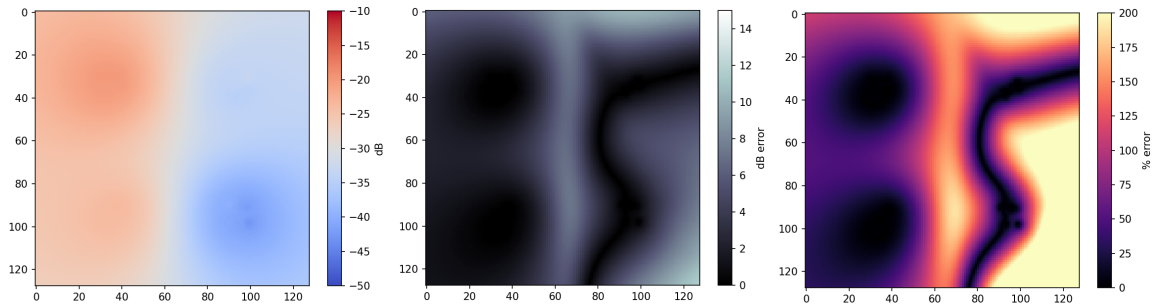

(a) (b) (c)

Figure 6.10. (a) $\beta = 2$ generated REM (b) dB error (c) % error.

In Figure 6.11-(a), the MCD clusters get more defined where we can see darker orange in $x < 64, y < 64$ zone and darker blue in $x > 64, y > 64$ zone, which aligns with the original REM. Also in Figure 6.11-(b), we can see error rates between clusters get lower, especially in $x < 64$ zone but we still fail to detect the zone where the high PLE zone starts and signal strength drop rapidly. Figure 6.11-(c) on the other hand, shows the errors get more refined, in $65 < x < 80, 80 < y < 100$ we can definitely see a new zone with a high error rate forming, which is alarming for high β values.

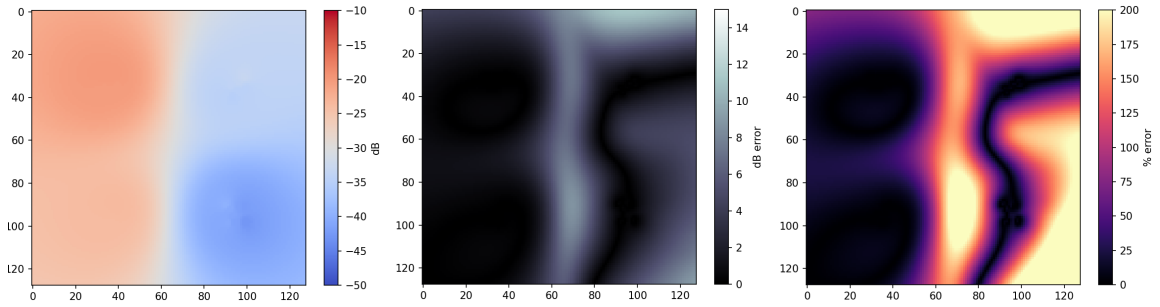

(a) (b) (c)

Figure 6.11. (a) $\beta = 3$ generated REM (b) dB error (c) % error.

In Figure 6.12-(a), we can observe the continuation of the trend of MCD cluster getting more defined. Also in Figure 6.12-(b), we can see error rates within the cluster areas get lower, but in the mean time observe the transition between clusters get sharper. Figure 6.12-(c) shows the errors get lower in $x > 100, 50 > y > 100$ but at the same time errors get higher in $55 < x < 75$ zone, where the transition from lower PLE zone to higher PLE zone happen in the original REM.

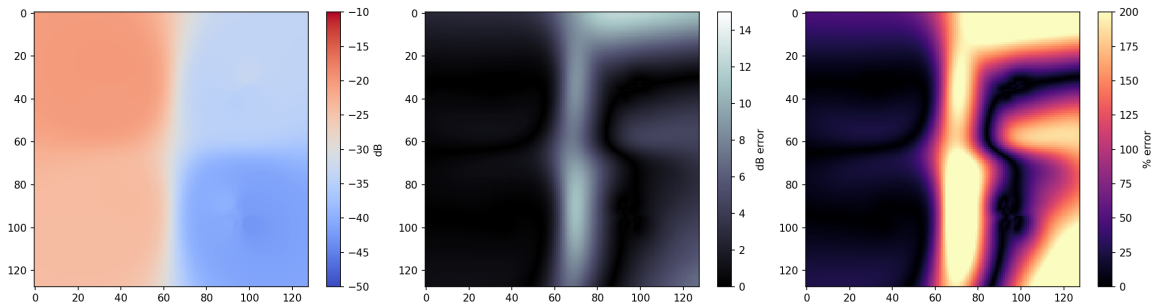

(a) (b) (c)

Figure 6.12. (a) $\beta = 5$ generated REM (b) dB error (c) % error.

Now let us compare IDW results to our proposed networks. To begin with, let us examine our most successful network, the Main Network. As it can be seen in Figure 6.13-(a), we are generating a more successful representation of the true REM compared to IDW algorithm. We can reconstruct the general shape of the network and general signal propagation characteristics. Most importantly, we correctly detect the

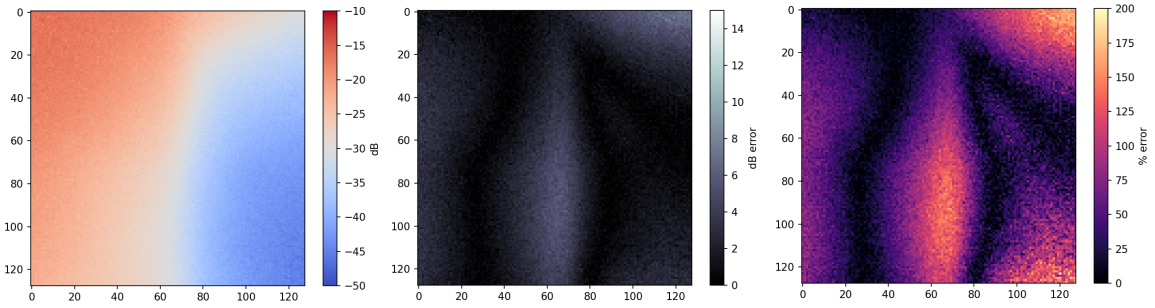

(a) (b) (c)

Figure 6.14. (a) Dropout network generated REM (b) dB error (c) % error.

high signal strength zone in $y < 20, x > 64$, which was absent in all IDW results. And we observe that our % error rates are reduced compared to Figure 6.6.

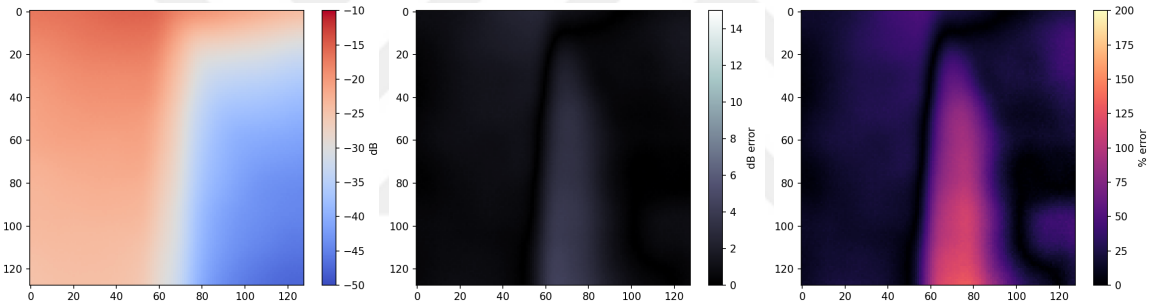

(a) (b) (c)

Figure 6.13. (a) Main network generated REM (b) dB error (c) % error.

In the case of the Dropout Network, there is still visible noise in the results, just like in the first example. But this time our % errors are higher than the 6.6. This is mainly related to high dropout rate we've decided. This goes on to show the dependency on good MCD coverage on the environment for this network architecture. Dropping 20% of the MCD inputs, which are clustered, causes the loss of subtle details which would help with REM reconstruction, such as the drastic PLE change at $x = 64$.

Lastly, our bigger network design can also make out the general propagation characteristics of the true REM, but it generally lacks the precision and has a high error rate. This could be its need to increase the training time and data exponentially, thus, training all the networks for the same amount of time fails to meet the needs for

a wider network. As it can be seen in Figure 6.15-(c), predicted REM has high error rates all over.

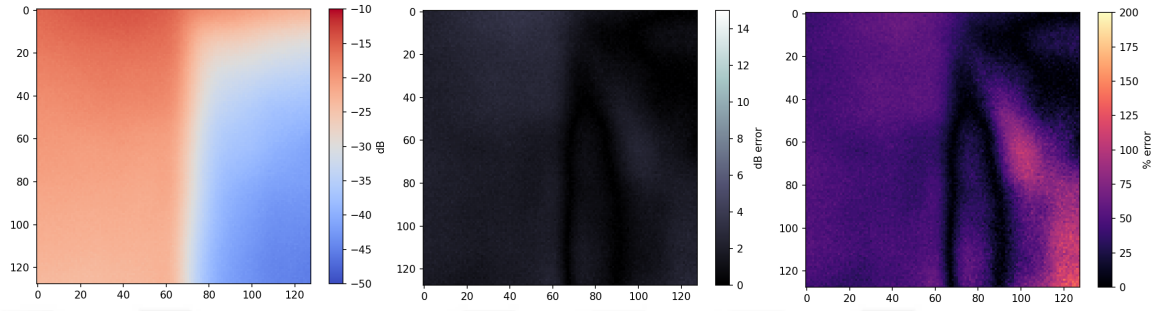

(a) (b) (c)

Figure 6.15. (a) Big network generated REM (b) dB error (c) % error.

6.3.2. Densely Packed Location Analysis

Now, let us discuss the effects of densely packing the MCDs on the REM prediction. By densely packing, we do not mean having all the MCDs in the same places, we might have occasional SUs which are close to the rest, such as the MCDs visible on Figure 6.7-(b) at $(17, 20)$ and $(96, 17)$. Densely packed MCDs generally concentrate on one region of the environment while there are some areas entirely devoid of MCDs. As it can be seen in the same figure, we have near-zero MCDs in $x > 100$ or $y > 80$ ranges which overlaps with the high-PLE region in Figure 6.8 in $x > 64$ range. Which could make us entirely miss this region and have high prediction errors.

Now let us begin analyzing this topic with IDW algorithm. As it can be seen in Figure 6.16, for $\beta = 1$, generated REM completely misses the high-PLE zone and predicts every point to have similar signal strength even though there are MCDs on the transition area.

For $\beta = 2$, we can see a slight improvement for visible MCDs on the transition area in $64 < x < 85$. These MCDs contribute more on the REM prediction, but overall REM still has high error rate, and more than 200% error on the high-PLE zone.

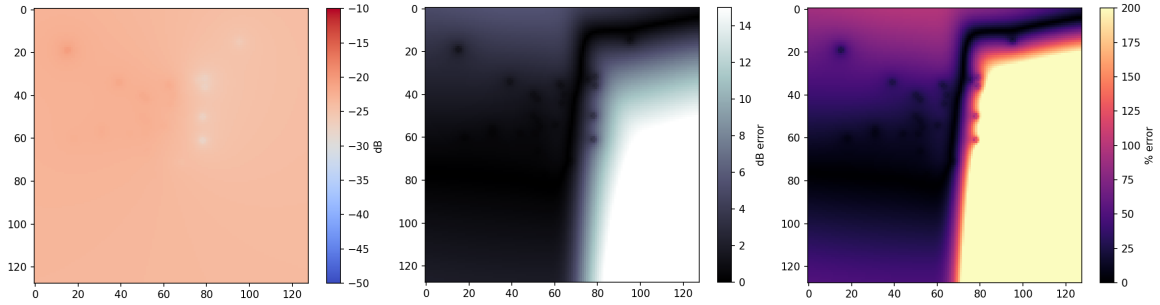

(a) (b) (c)

Figure 6.16. (a) $\beta = 1$ generated REM (b) dB error (c) % error.

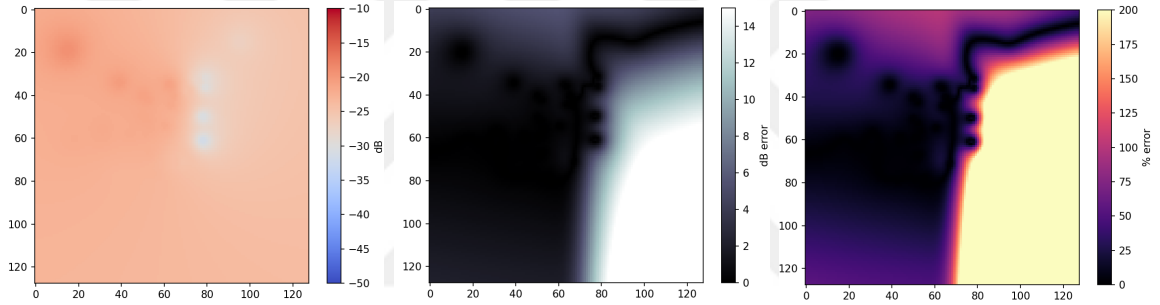

(a) (b) (c)

Figure 6.17. (a) $\beta = 2$ generated REM (b) dB error (c) % error.

In the case of $\beta = 3$, the error rates for the zone $x < 64, y < 64$ decrease significantly, but the sky-high error rates in the high-PLE zone persists. Also, we continue to see the continuation of the trend of MCDs on the transition area effecting a bigger zone.

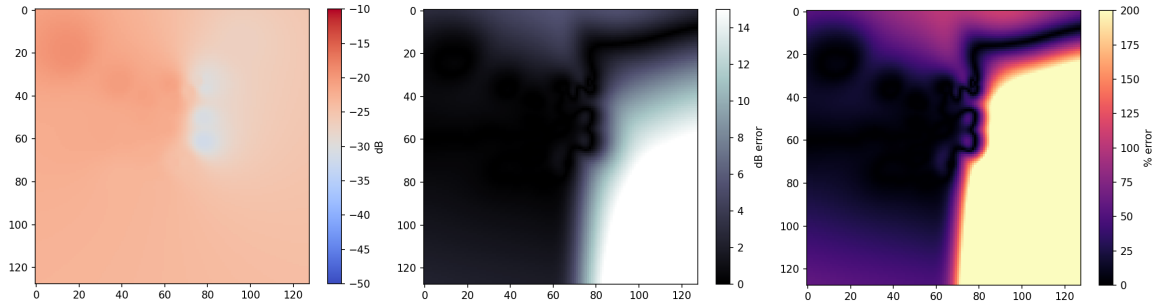

(a) (b) (c)

Figure 6.18. (a) $\beta = 3$ generated REM (b) dB error (c) % error.

For $\beta = 5$, which is visible in Figure 6.19, dB errors keep decreasing, even in high-PLE zone, but it is no where near to detect the propagation characteristics of the entire environment. This goes on to show us the importance of MCD location for the REM generation performance using the IDW algorithm.

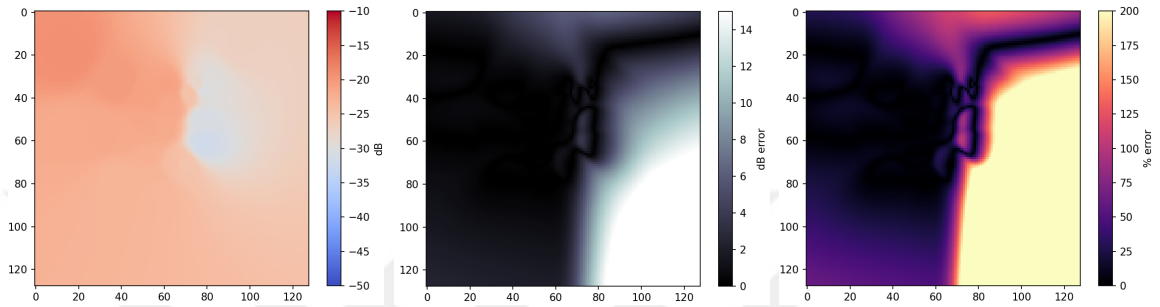

(a) (b) (c)

Figure 6.19. (a) $\beta = 5$ generated REM (b) dB error (c) % error.

Now let us discuss our methods, focusing first on the Main Network as we did before. As we observe Figure 6.20-(a), we see a slightly blue region emerging where there is a high-PLE zone. This is something beyond numerical measurement because we are detecting the general propagation characteristics. Even with the high % errors persist in Figure 6.20-(c), it is invaluable to detect the presence of a different zone within the environment we are trying to map.

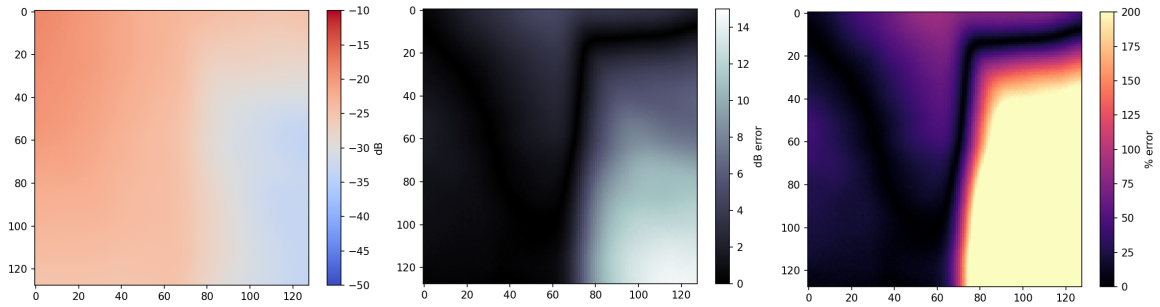

(a) (b) (c)

Figure 6.20. (a) Main network generated REM (b) dB error (c) % error.

As it can be seen in Figure 6.21, Dropout Network improves upon the Main Network by more clearly defining the lines and characteristics of the high-PLE region. Despite the presence of visible noise, this area is successfully identified due to the network's high dropout rate. This result provides a strong argument for using and further developing this method. In previous examples, we've seen the Main Network beat this method repeatedly, but in dire circumstances, having a high dropout rate helps the network by preparing it to unexpected scenarios.

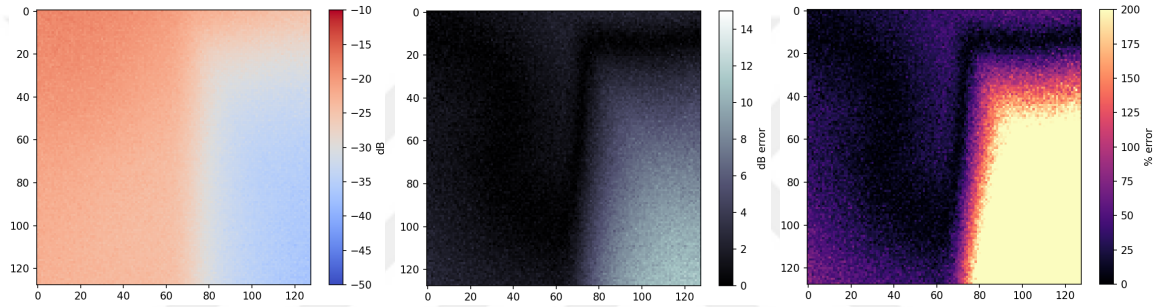

(a) (b) (c)

Figure 6.21. (a) Dropout network generated REM (b) dB error (c) % error.

Our last method, the Big Network, completely misses the high-PLE zone and even fails to predict the correct signal power in low-PLE zone, as shown in Figure 6.22. This network needs a revision or a separate training method to be useful in any capacity.

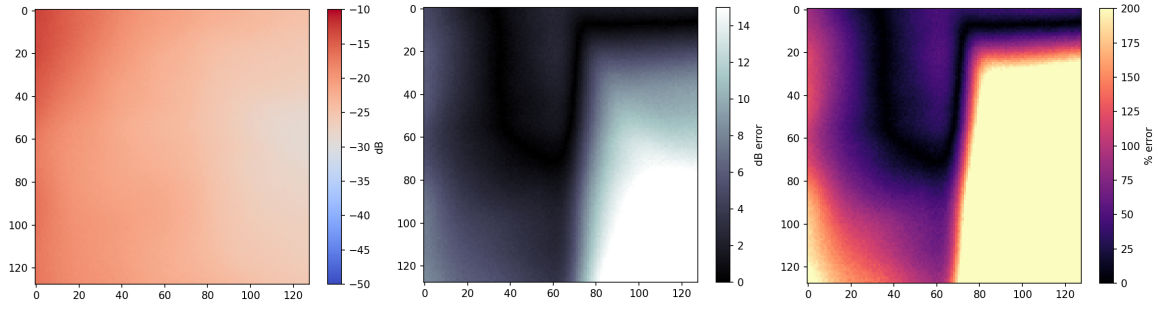

(a) (b) (c)

Figure 6.22. (a) Big network generated REM (b) dB error (c) % error.

6.3.3. Evenly Distributed Location Analysis

In order to complete the topic of *Effects of MCD distribution on REM generation performance*, we must cover even distribution of the MCDs over the area of interest. Even though this method is unnatural and can be costly, this is expected to perform the best. An example distribution of 31 MCDs can be seen in Figure 6.7-(d).

Let us begin our analysis with IDW algorithm with the $\beta = 1$. In Figure 6.23, we can see that even with the low β value, IDW can outline the high-PLE zone, especially compared to the previous case. Despite this, the tradition of high dB and % errors for $\beta = 1$ continues, which is visible Figure 6.23(b-c). A newly risen highlight for this distribution is visible low error rates on the zone where the transition between the low-PLE zone and the high-PLE zone.

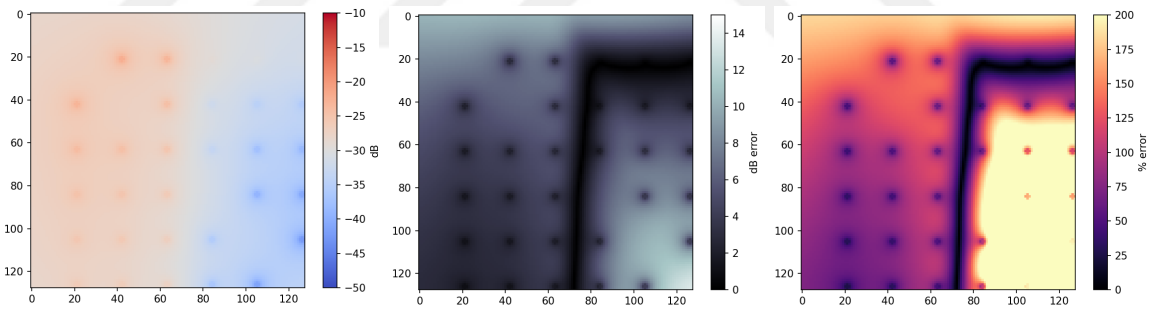

(a) (b) (c)

Figure 6.23. (a) $\beta = 1$ generated REM (b) dB error (c) % error.

For $\beta = 2, 3, 5$, the predicted REM gets smoothed out and overall error rates are better than their counterparts in previous distributions. Increasing the β values reduces the error rates for $x < 64$ zone to near-zero levels, but high error rate can be seen in different parts of the $x > 64$ region, even then, it is the best version of the IDW algorithm. Because this was expected, no further comments will be made about rest of the graphs on IDW algorithm.

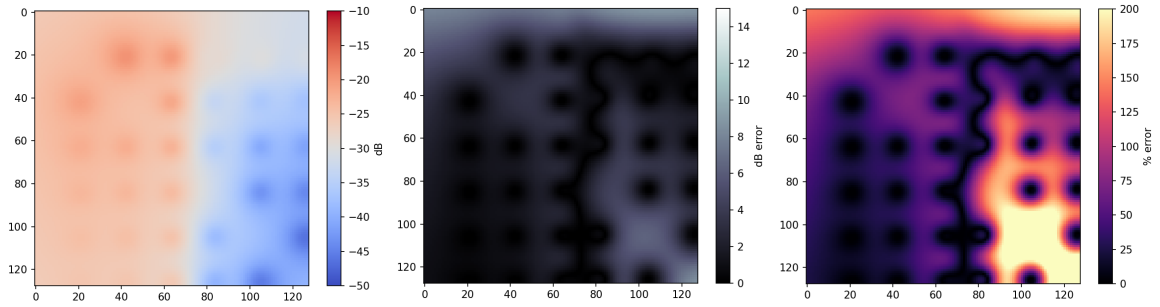

(a) (b) (c)

Figure 6.24. (a) $\beta = 2$ generated REM (b) dB error (c) % error.

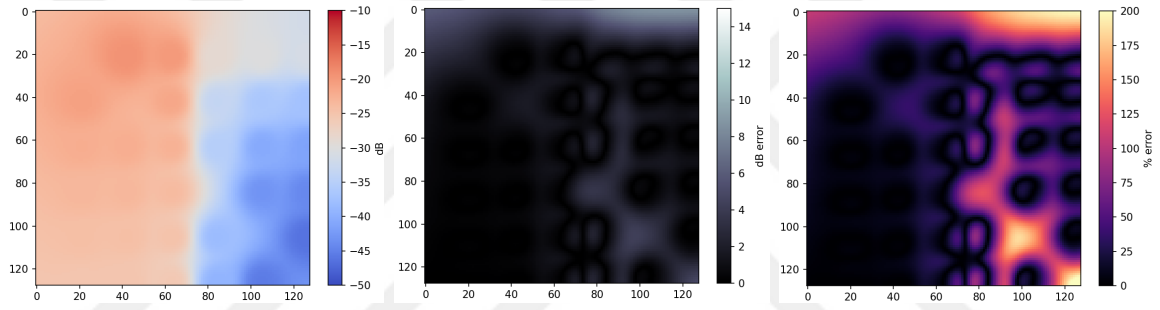

(a) (b) (c)

Figure 6.25. (a) $\beta = 3$ generated REM (b) dB error (c) % error.

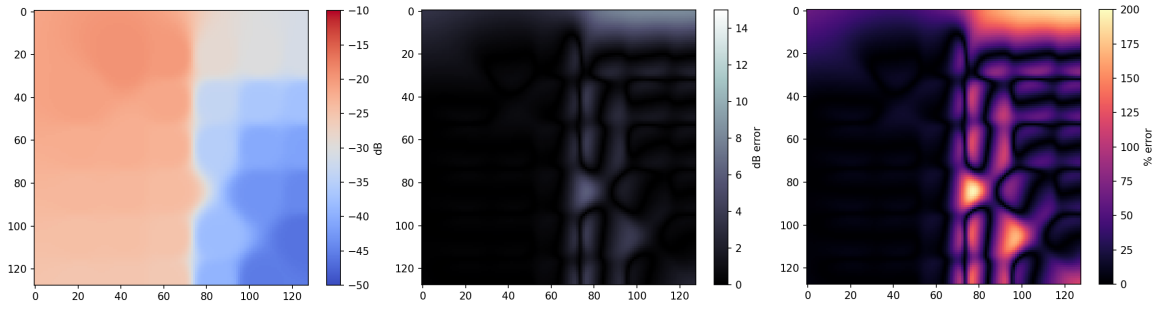

(a) (b) (c)

Figure 6.26. (a) $\beta = 5$ generated REM (b) dB error (c) % error.

Now let us discuss our proposed algorithms and how they work in the case of evenly distributed MCDs. Figure 6.27 shows us the predictions are better than densely packing MCDs, but worse than clustered distribution. Previously, on Figure 6.20-(b) we've seen a more pronounced error rate at the transition about $x = 64$ line, but this

changes in this distribution, where we see a less pronounced error rate at this zone, but there is a higher error rate at the top-right corner of the Figure 6.27-(b). Subfigures (c) show a higher error rate at this zone, but a lower error rate at $x < 64$. But compared to Figure 6.13-(c), there is a higher error rate in the high-PLE region. This is because having four different clusters of MCDs helps with deciding two-zone REMs, but it is the opposite for multi-region REMs.

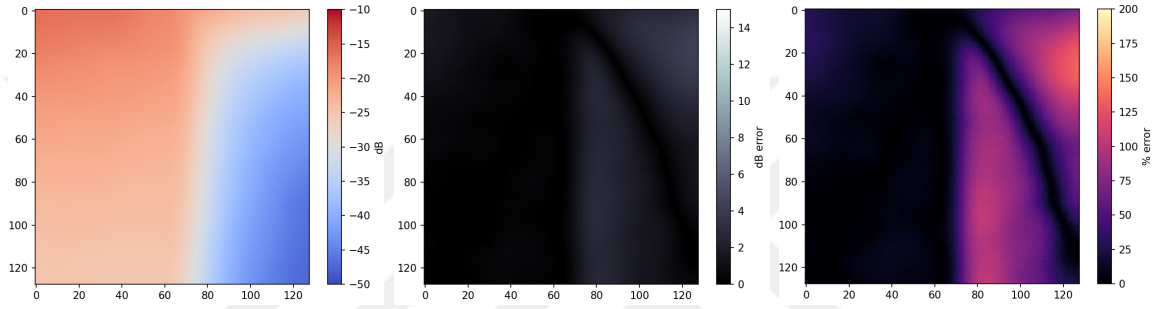

(a) (b) (c)

Figure 6.27. (a) Main network generated REM (b) dB error (c) % error.

Dropout network on the other hand, somehow exceeds the Main Network in terms of capturing the general propagation characteristics, although the Main Network was more successful in every other aspect. Also, the problem of having a high noise for this network still remains. A solution for this might be adding a smoothening layer at the end of the Dropout Network, which might help with the persisting noise, but might risk failing to capture the sudden spikes in PLE or interference. And this network design also exceeds Figure 6.14-(c) in terms of lower error rates which is different from Main Network and Bigger Network architectures. Dropping out random MCDs when they are evenly distributes does not a skew towards a random zone, but given that clustered MCDs are closer to eachother, having a slight unevenness in terms of number of MCDs between clusters can create a skew towards one clusters.

Compared to earlier results in Figure 6.2, error rates in Figure 6.29-(b) are higher. This goes on to show us the ability for clustered MCD distribution to detect Two-zone REMs better.

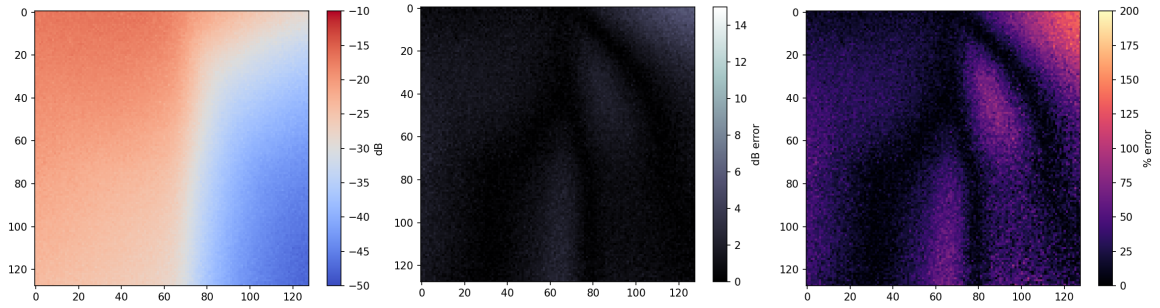

(a) (b) (c)

Figure 6.28. (a) Dropout network generated REM (b) dB error (c) % error.

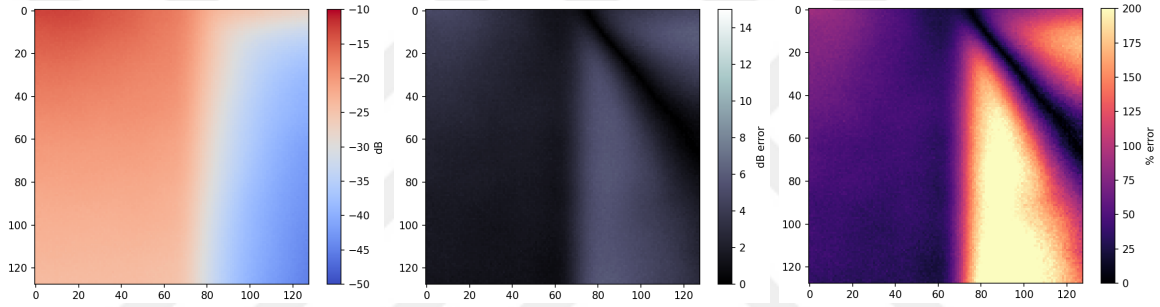

(a) (b) (c)

Figure 6.29. (a) Big network generated REM (b) dB error (c) % error.

Our last word for this analysis step is; densely packing SUs (or MCDs) has a significant effect on REM reconstruction. Despite clustered distribution having a slight edge on MSE, there is no evidence that it is significant and there is no proof that this is a universally valid rule. As it was previously discussed, this is mainly because of our database distribution and is related to the fact that the locations of the clusters are being symmetrical to each other.

6.3.4. General Analysis Of PU Location

Now let us discuss effects of the PU location on the REM generation. In our case, there are two possibilities for the PU, it is either in the area of interest, A, or is out of the boundaries of it. In our case, out of 442 REMs we predicted, which are not present in the training data, 49 of REMs have the PU in the A, meanwhile 393 of them have

Table 6.10. Analysis of algorithm behavior when PU is in A.

	Main Network	**Dropout Network**	**Big Network**
MSE	9.444	10.582	25.468
σ	13.482	8.063	20.294

the PU is not located in A. Given that PU can be located between $-128 < x < 256$ and $-128 < y < 256$, this distribution is expected.

As it can be seen in Table 6.9, when the PU is in A, error rates increase significantly, the same behavior is also present in Table 6.10. This is caused by the fact that PU being in the A increases the range of dB present in the REM. For example, a given REM with a PU in A can have signal strength ranging from +10dB to -50dB, but if a PU has no resident PU in A signal strength range from -20dB to -60db.

Table 6.9. Analysis of IDW behavior when PU is in A.

	$\beta = 1$	$\beta = 2$	$\beta = 3$	$\beta = 5$
MSE	49.833	21.289	14.073	12.230
σ	17.512	10.628	8.570	7.178

In Table 6.10 we see the trend of Main Network making better predictions but having a higher standard deviation than Dropout Network continue. Despite the Main Network having 2.5 times more MSE than its overall performance, it clearly has better performance than any other approach, but the Dropout Network comes closer to ever to the Main Network in terms of MSE performance. Also, surprisingly, Big Network architecture is not that far behind, considering its average performance in MSE is 10 times worse than Main Network.

In Table 6.11, we see that the error rates decrease significantly. Predictions are overall three times better in terms of MSE, but no significant change in terms of standard deviation is observed.

Table 6.11. Analysis of IDW behavior when PU is not in A.

	$\beta = 1$	$\beta = 2$	$\beta = 3$	$\beta = 5$
MSE	18.762	8.332	5.305	4.178
σ	18.068	9.014	6.546	5.710

In Table 6.12, we see a interesting trend. While two network designs, Main Network and Dropout Network perform better than when the PU is in A, Big Network performs worse with this scenario. This could be because of Big Network tends to predict overall higher signal strength, which helps when PU is in A, which results in higher signal strength overall. The same trend continues in terms of standard deviation.

Table 6.12. Analysis of algorithm behavior when PU is not in A.

	Main Network	**Dropout Network**	**Big Network**
MSE	3.128	6.951	40.328
σ	7.967	6.882	34.361

After this general performance analysis on PU location, we must talk about four different cases that is present in our predictions; there is either a PU is present in A or not, and the REM type is either two zone or N zone. So we must discretely analyze these cases in order to better understand how IDW algorithm and our proposed algorithms work when predicting a REM.

6.3.5. PU Inside A: Two Zone REM

This case will cover when the REM type is two zone, and there is a PU resident in A. In Figure 6.30, we can see that the PU is located at the top right side of the REM, despite this region having more signal power than -10 dB, we will not change the color map range in order to make these analysis fit the rest of this thesis.

As it can be seen in the same figure, there is a clear signal power drop at $x = 64$ line when signal travels from the PU, which is located at the right side of the REM, to the left side of the REM.

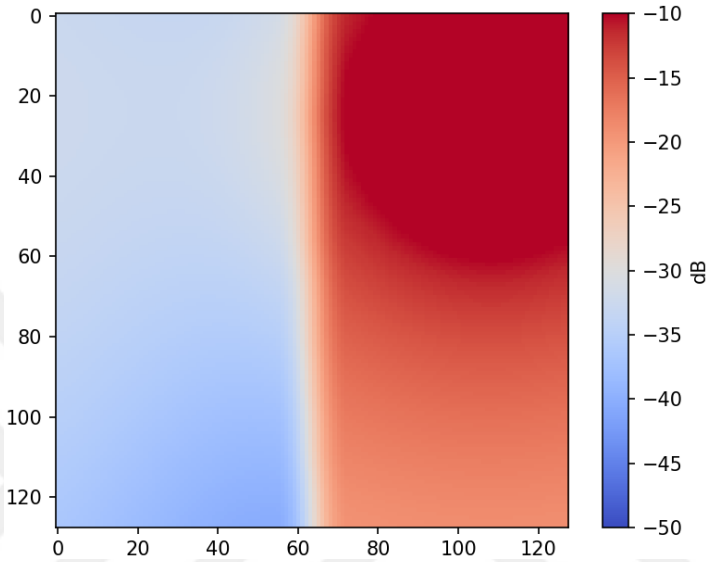

Figure 6.30. PU inside A: original two zone REM.

Figures 6.31-6.34 show the performance of the IDW algorithm on the case of PU residing in a two zone REM. As it can be seen in those figures, increasing the β value, makes us predict the high PLE zone on the left easier, but at the same time, no β value makes us comprehend the entire REM characteristic.

We entirely miss on the PU location and the high signal power in locations close to the REM. Moreover, using the IDW algorithm, we cannot accurately predict when we transition from a low PLE region to a high PLE region. There is a high error rate zone clearly visible in $50 < x < 64$ zone for all β values.

Now, let us examine the algorithms we proposed, and as per the tradition we have set throughout this thesis, we will begin our analysis with the Main Network. In Figure 6.35, we see the arguably the best result for our Main Network so far. Percentage and dB errors are near-zero for this case. This is probably caused by the fact that there

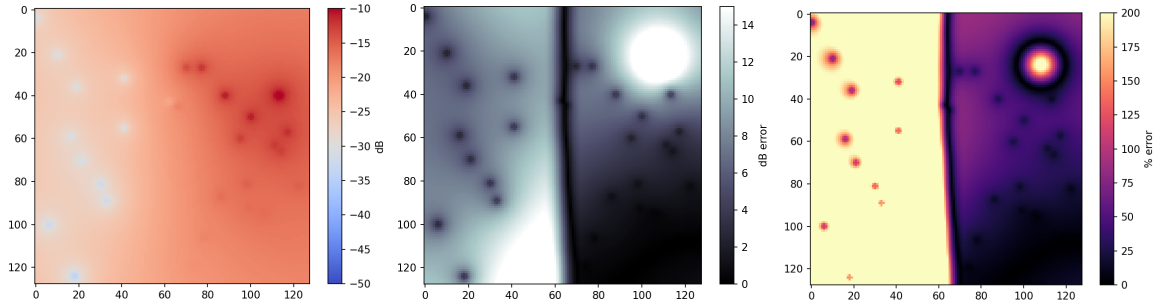

(a) (b) (c)

Figure 6.31. (a) $\beta = 1$ generated REM (b) dB error (c) % error.

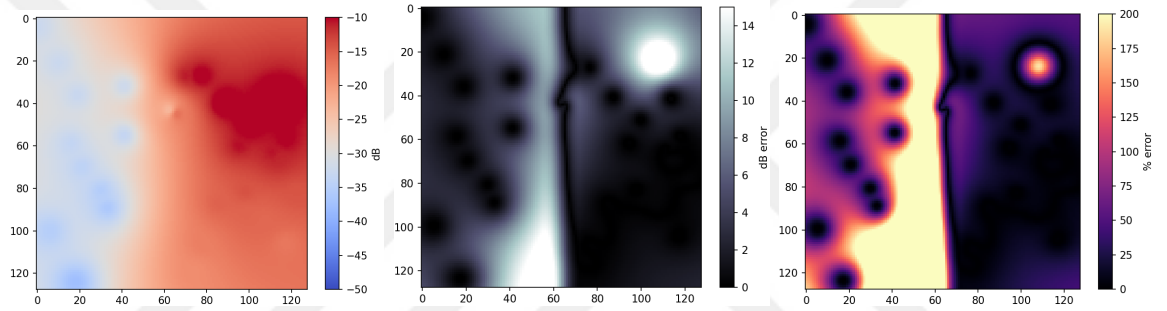

(a) (b) (c)

Figure 6.32. (a) $\beta = 2$ generated REM (b) dB error (c) % error.

are 20.000 two zone REMs within our datasets, and if probability of PU being in the A holds true to 11.1%, we can expect at least 2200 REMs where the REM type is two zone and there is a resident PU. Because this REM type lacks the variation, we can certainly assume that our models have trained on a similar REM-despite this particular REM not existing in our training dataset.

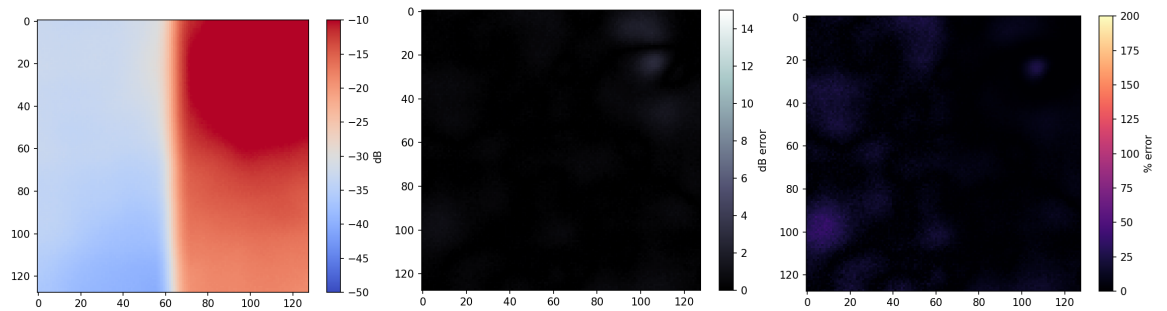

(a) (b) (c)

Figure 6.35. (a) Main network generated REM (b) dB error (c) % error.

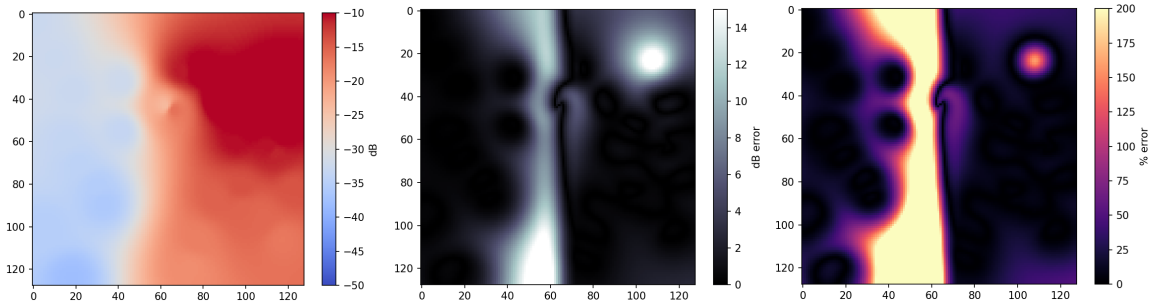

(a) (b) (c)

Figure 6.33. (a) $\beta = 3$ generated REM (b) dB error (c) % error.

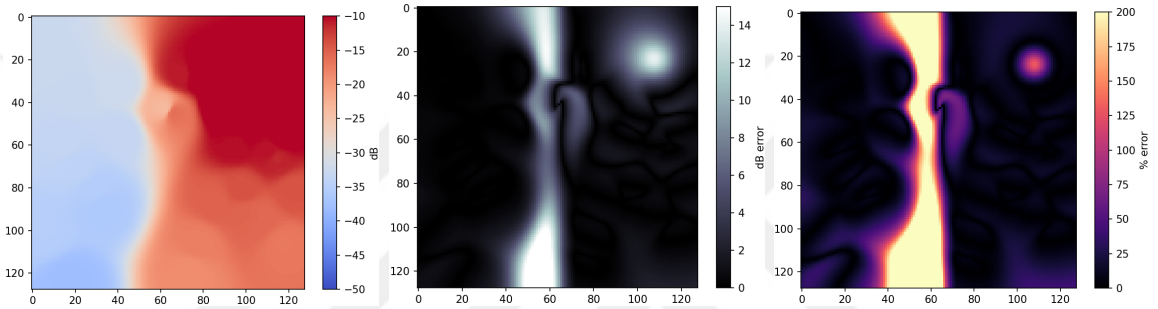

(a) (b) (c)

Figure 6.34. (a) $\beta = 5$ generated REM (b) dB error (c) % error.

Same trend continues with our Dropout Network and Big Network algorithms where we see a successful reconstructions throughout. In Figure 6.36 and 6.37 we see relatively low error rates compared to previous cases. In the case of Dropout Network, this is particularly impressive despite missing a high signal strength zone near the PU because of the 20% dropout rate. Even if the network is trained on the same REM, it drops the 20% of the inputs, which makes overfitting impossible. Therefore we cannot say the same thing we said to Main Network about "training on similar data" to the Dropout Network.

6.3.6. PU Inside A: N Zone REM

In this case, we will analyze a REM with N different resident zones with different propagation characteristics. As it can seen in Figure 6.38, there is a clear high PLE zone at $70 < x < 100$ and $35 < y < 55$ which creates a huge shadowing effect to the top right side ($x > 70$ and $y < 60$) of the REM.

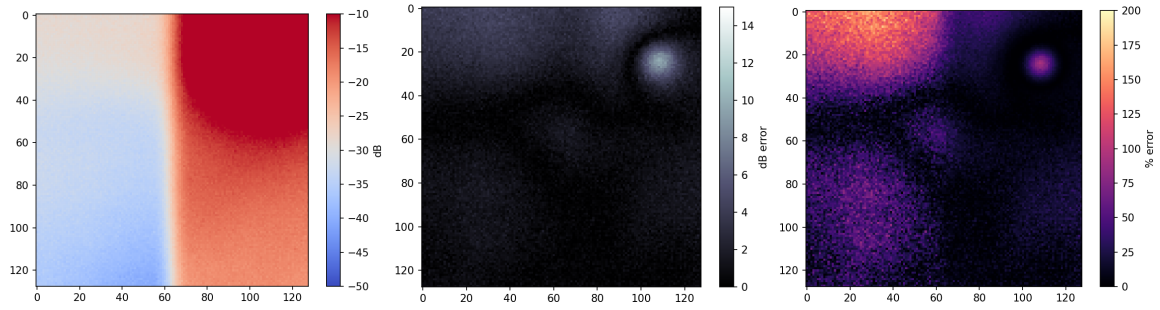

(a) (b) (c)

Figure 6.36. (a) Dropout network generated REM (b) dB error (c) % error.

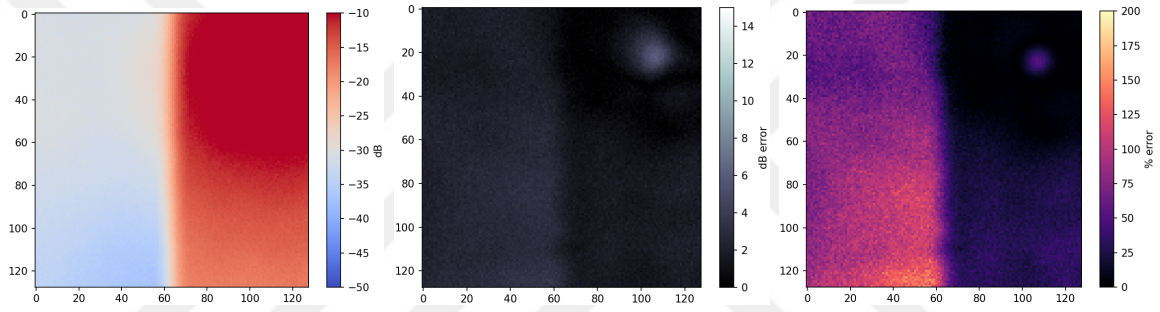

(a) (b) (c)

Figure 6.37. (a) Big network generated REM (b) dB error (c) % error.

Now let us analyze how the IDW algorithm works on a such case. As it can be seen in Figure 6.39-(a) there are five different MCDs within the high PLE zone we have described previously. This is a highly lucky scenario for the IDW algorithm because it can detect this zone opposite to what happened in densely distributed REM case we have discussed previously. But as it can be seen for all β values, IDW algorithm fails to capture the true strength of this high PLE zone and cannot define its boundaries. But it does a good job on locating and evaluating the PU location and that second high PLE zone.

After this, let us discuss our algorithms and how they work compared to the IDW algorithm, and let us start with the Main Network algorithm. As it can be seen in Figure 6.43, the network predicts the high PLE zone to the top right of the REM almost perfectly, but it fails to locate the PU and the second high PLE zone compared to the IDW algorithm. Despite this, in Figures 6.43-(b,c) we see lower error rates. And

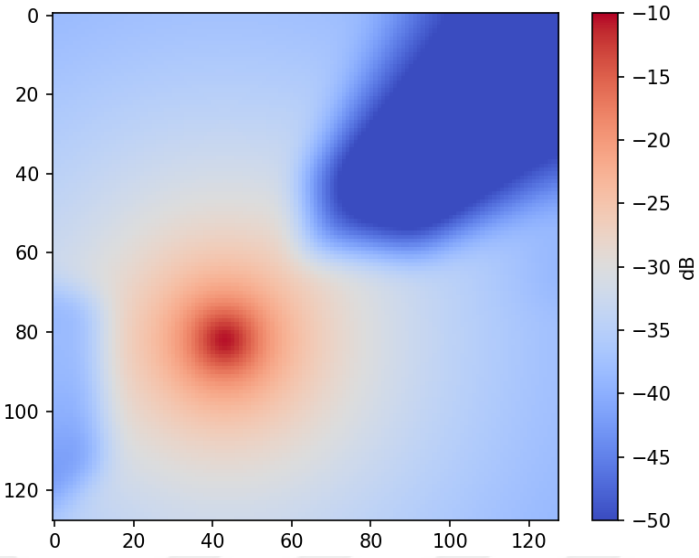

Figure 6.38. PU inside A: original N zone REM.

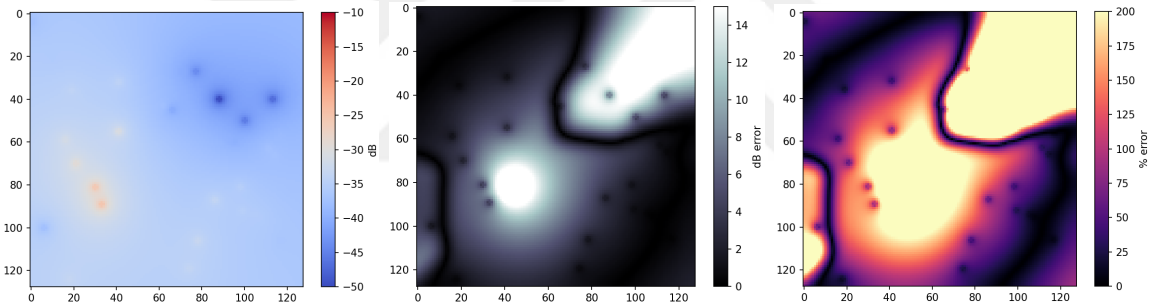

(a) (b) (c)

Figure 6.39. (a) $\beta = 1$ generated REM (b) dB error (c) % error.

despite outlining the high PLE zone successfully, this algorithm fails to comprehend the severity of it and has a huge % error rate within that zone.

Our other two algorithms cannot describe the zones or the PU location we have discussed previously. Despite this, Big Network algorithm predicts the characteristics of these zones better than the Dropout Network algorithm, which is opposite to what we have observed so far.

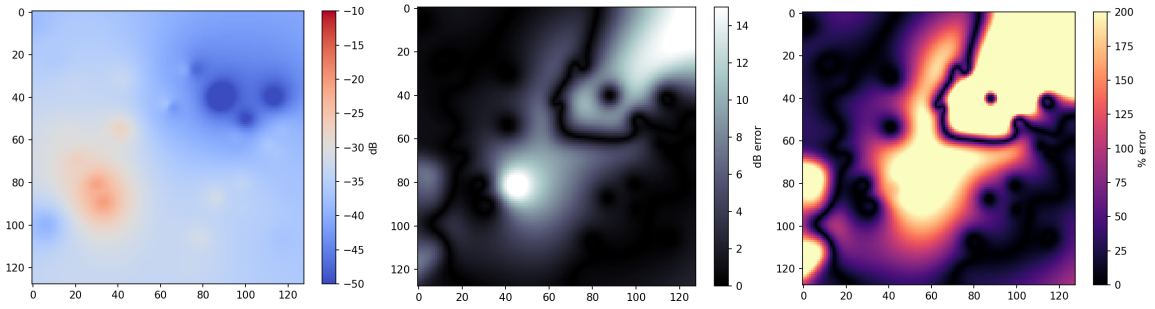

(a) (b) (c)

Figure 6.40. (a) $\beta = 2$ generated REM (b) dB error (c) % error.

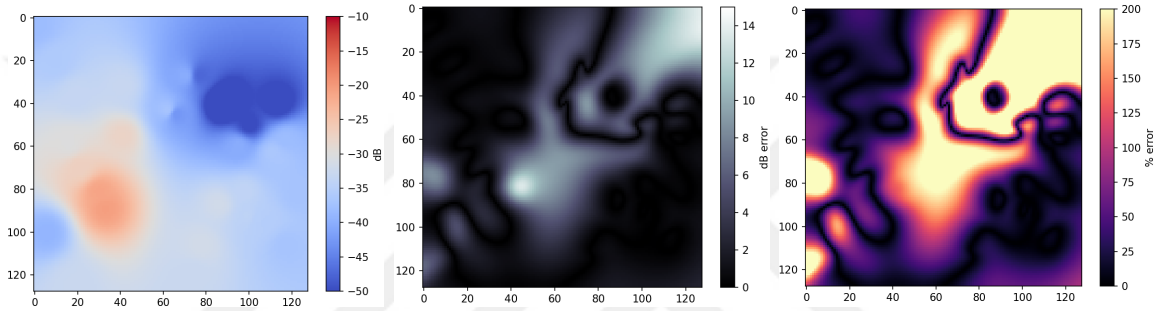

(a) (b) (c)

Figure 6.41. (a) $\beta = 3$ generated REM (b) dB error (c) % error.

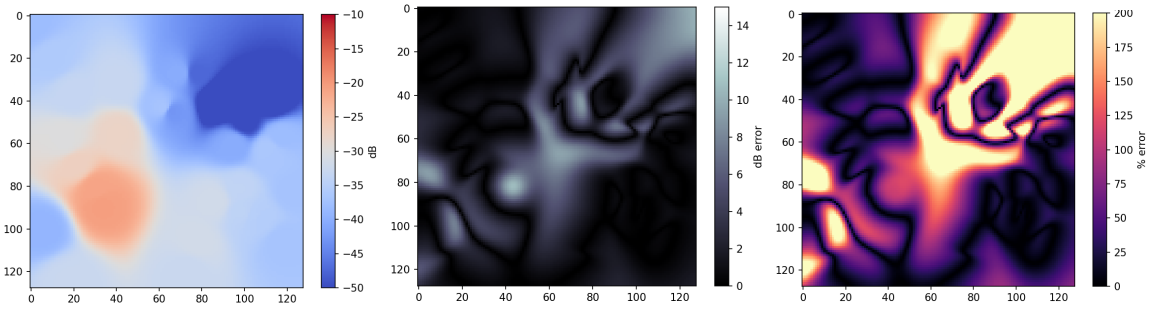

(a) (b) (c)

Figure 6.42. (a) $\beta = 5$ generated REM (b) dB error (c) % error.

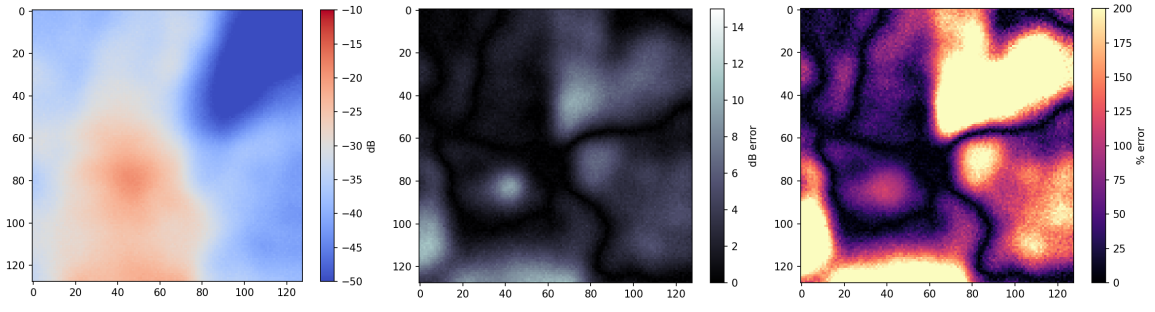

(a) (b) (c)

Figure 6.43. (a) Main network generated REM (b) dB error (c) % error.

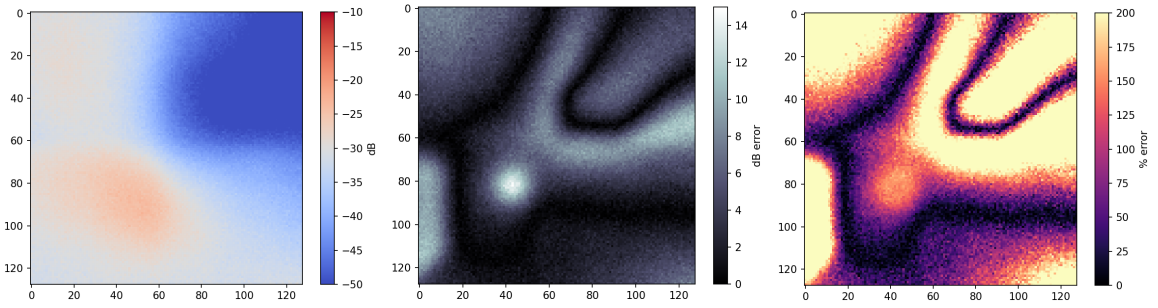

(a) (b) (c)

Figure 6.44. (a) Dropout network generated REM (b) dB error (c) % error.

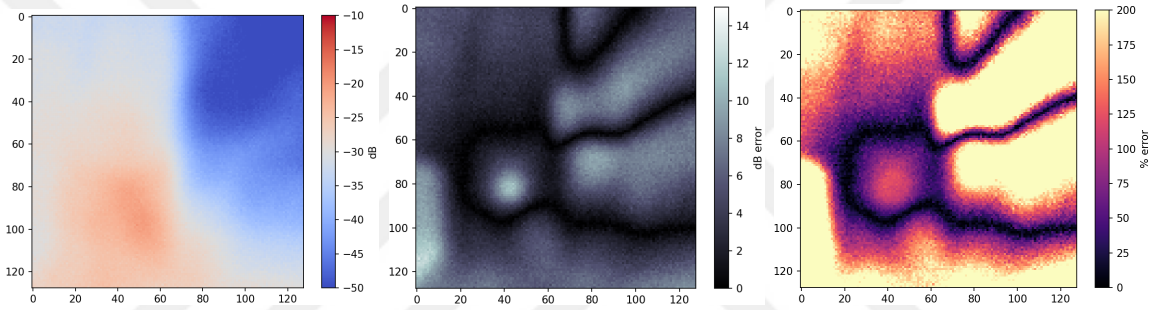

(a) (b) (c)

Figure 6.45. (a) Big network generated REM (b) dB error (c) % error.

6.3.7. PU Outside A: Two Zone REM

Now let us move to our benchmark case where the REM type is two zone and the PU is not a resident of A. We have repeatedly discussed this scenario previously, but the REM we will discuss now is completely different in terms of propagation characteristics, despite being subject to the same case. As it can be seen in Figure 6.46, there are slightly high received signal power zones at the top right and top left zones of the REM. At first glance, this does not make sense so we have to go deeper into analyzing this situation. The PU for this scenario is located at $(151, -40)$, which is over the top right corner of the REM. This means that the high signal power zone at the top right corner is directly related to its proximity to the PU. Top left side on the other hand, must have been caused by a shadowing effect. This means that the right side of the REM must be subject o a high PLE zone, whereas the left side must be subject o a low PLE zone. This means that at the $(64, 0)$ point, the high PLE will cause shadowing

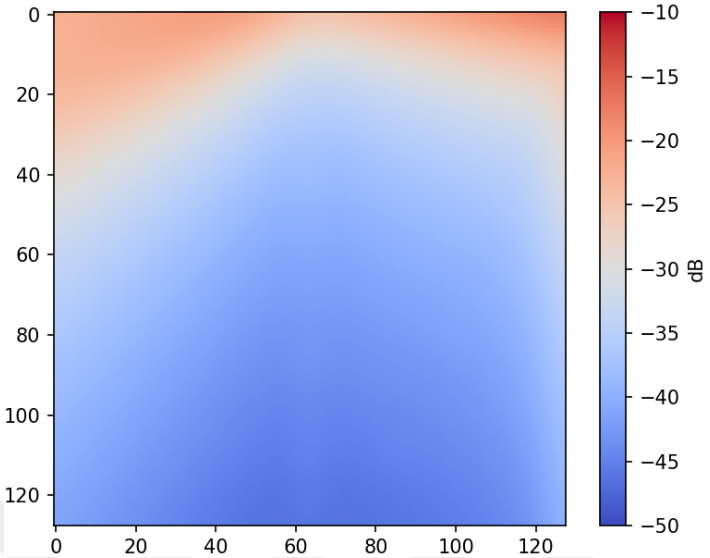

Figure 6.46. PU outside A: original two zone REM.

to the left side and reduce signal power at the lower parts of the low PLE zone, but it has no effect on the top left corner, which has high received signal power.

Now let us discuss how the IDW algorithm handles this unique situation. As it can be seen in Figure 6.47, there are no MCDs located to the top left side of the REM, which will mean that IDW will miss the high received signal strength in this zone and will assume that this zone is also receiving low signal power. This conclusion is confirmed across Figures 6.47-6.50.

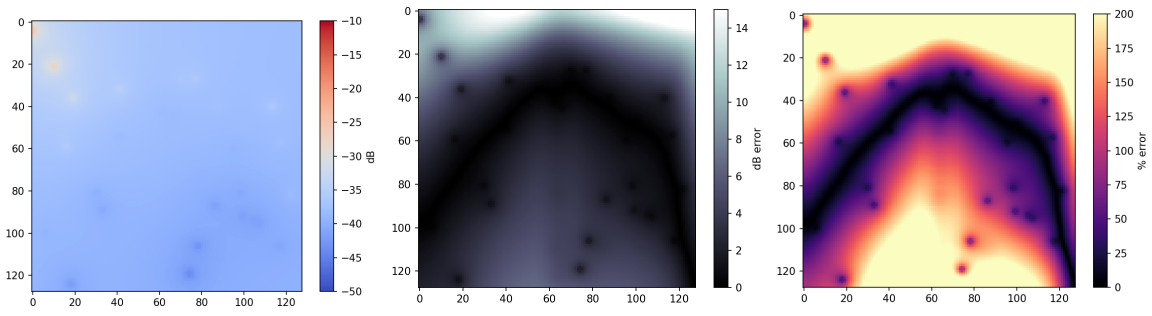

(a) (b) (c)

Figure 6.47. (a) $\beta = 1$ generated REM (b) dB error (c) % error.

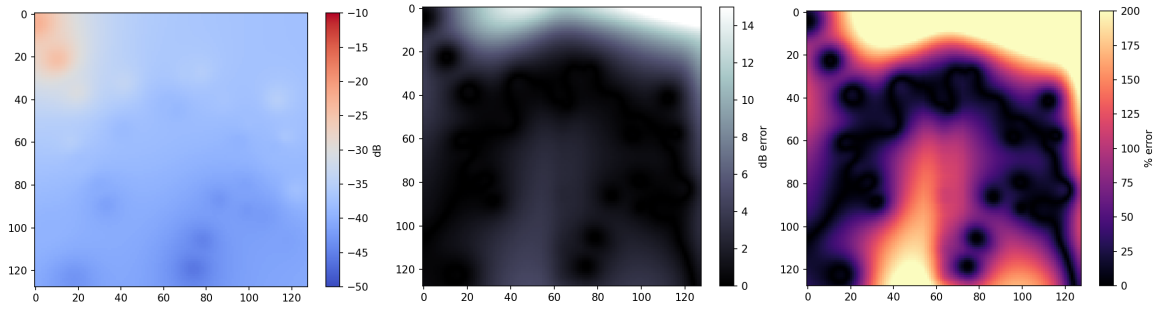

(a) (b) (c)

Figure 6.48. (a) $\beta = 2$ generated REM (b) dB error (c) % error.

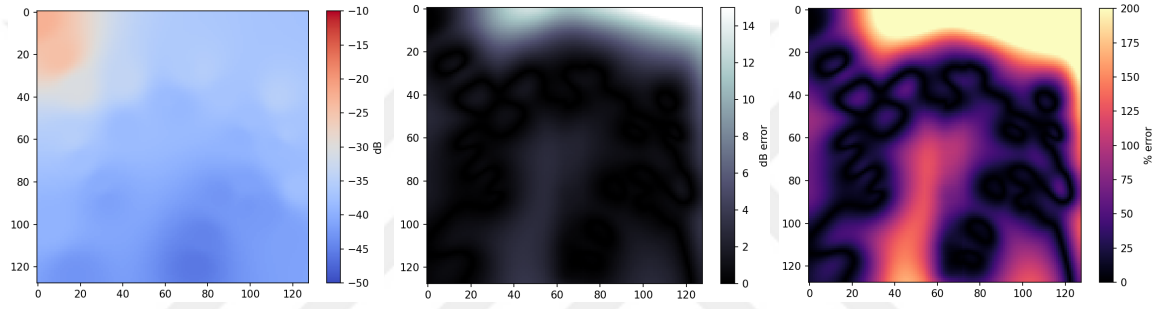

(a) (b) (c)

Figure 6.49. (a) $\beta = 3$ generated REM (b) dB error (c) % error.

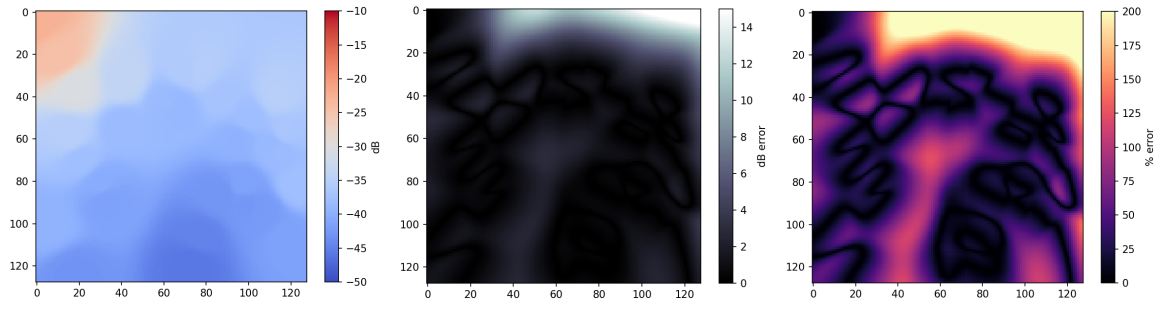

(a) (b) (c)

Figure 6.50. (a) $\beta = 5$ generated REM (b) dB error (c) % error.

Now lets begin how our algorithms work in this uncommon case. As it can be seen in Figure 6.51, our algorithm almost perfectly predicts this case. But how can be this true? Don't we just take IDW as an input to this network? How can it so clearly outperform IDW algorithm? In Figure 6.50-(a), there is a clear low signal strength zone at the bottom center of the map. This signifies that the PU must be at directly top of the A.

But given that there is a high received signal power at the top left of the map, and the signal power increases at bottom left and bottom right corners this cannot be true. Only logical explanation for this there should be another high signal strength zone at the opposite side of the known area at the top left. Now that we have predicted that there is another high signal strength zone at the top right, can we decide the PU is closer to which one? This is almost impossible to tell because of the shadowing the high PLE zone creates, which makes both sides identical but mirrored in terms of received signal strength.

Given that we have equal amounts of samples on both N zone REM and two zone REM, this performance is an outlier, an example to overfitting and should not be occurring in a more balanced dataset in terms of probability of encountering two zone REM in the real world.

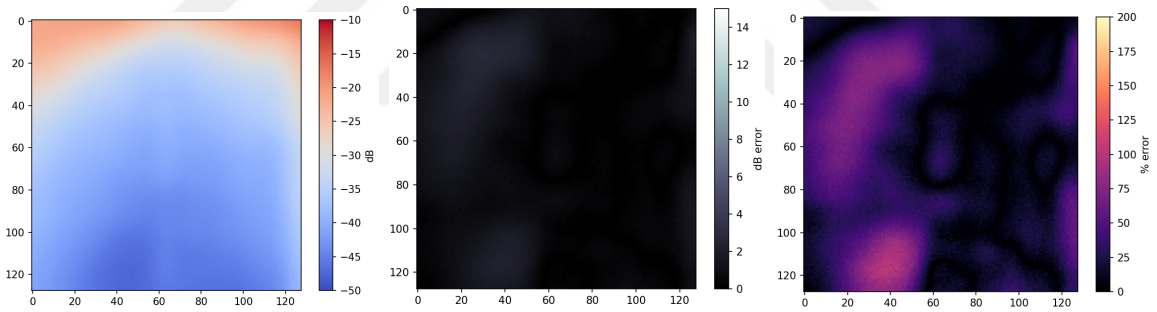

(a) (b) (c)

Figure 6.51. (a) Main network generated REM (b) dB error (c) % error.

Our other two algorithms can also predict that high signal strength zone , but they lack the precision compared to Main Network algorithm. Figures 6.52-6.53 confirm this by showing a greater noise and error rate throughout the REM.

6.3.8. PU Outside A: N Zone REM

Now let us examine our last example in this thesis. The case for this example is the REM type is N zone and there is no resident PU within A. As it can be seen in Figure 6.54, there is a REM located at $(60, 134)$, which is just outside of the

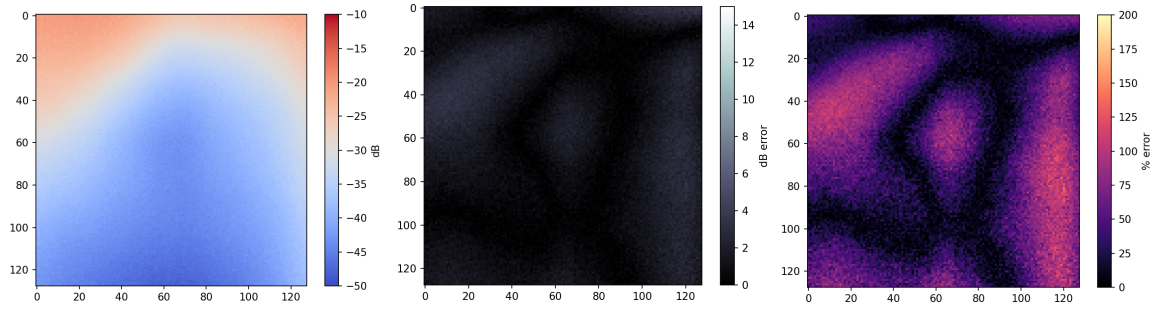

(a) (b) (c)

Figure 6.52. (a) Dropout network generated REM (b) dB error (c) % error.

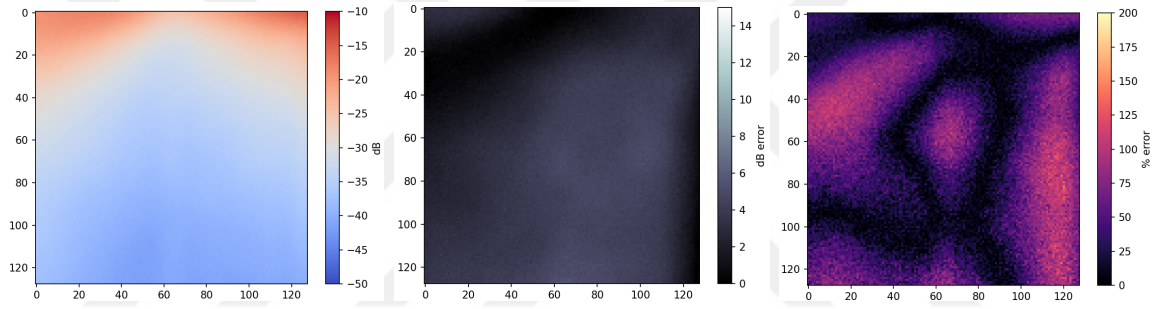

(a) (b) (c)

Figure 6.53. (a) Big network generated REM (b) dB error (c) % error.

perimeters of A. There are four different zones within this example, the first is located at $118 < x < 136$ and $7 < y < 65$ with a PLE of 2.67, the second is located at $95 < x < 104$ and $55 < y < 84$ with a PLE of 3.31, the third is located at $73 < x < 131$ and $67 < y < 85$ with a PLE of 3.14, the fourth and the last is located at $102 < x < 136$ and $16 < y < 62$ with a PLE of 3.06. The base map PLE (PLE outside of all defined zones) is 2.38 for this map. In the same figure, we can see the shadowing effect those regions create over the RF environment.

Now let us discuss the performance of IDW algorithm with different β values. As we can see in Figures 6.55-6.58 all results from the IDW algorithm fails to detect the PU presence which is neighboring the REM. At higher β values it can detect the zones where the signal power drops significantly, but regardless, it lacks the precision.

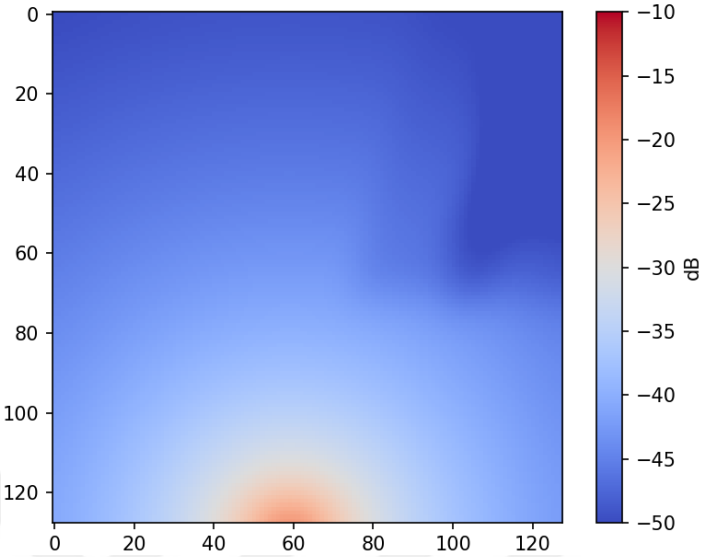

Figure 6.54. PU outside A: original N zone REM.

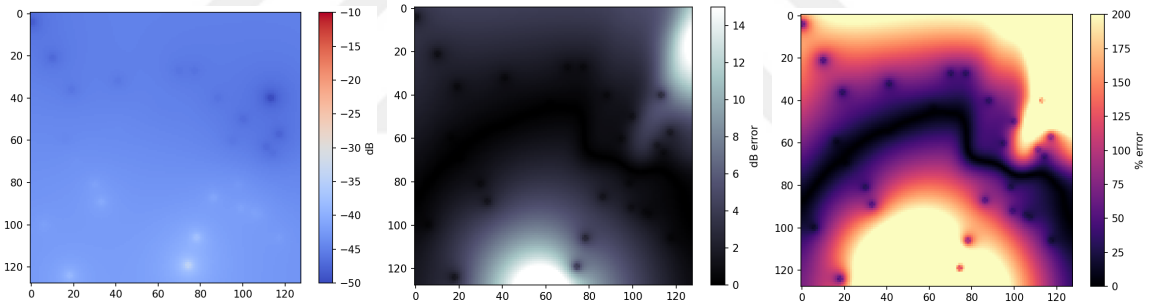

(a) (b) (c)

Figure 6.55. (a) $\beta = 1$ generated REM (b) dB error (c) % error.

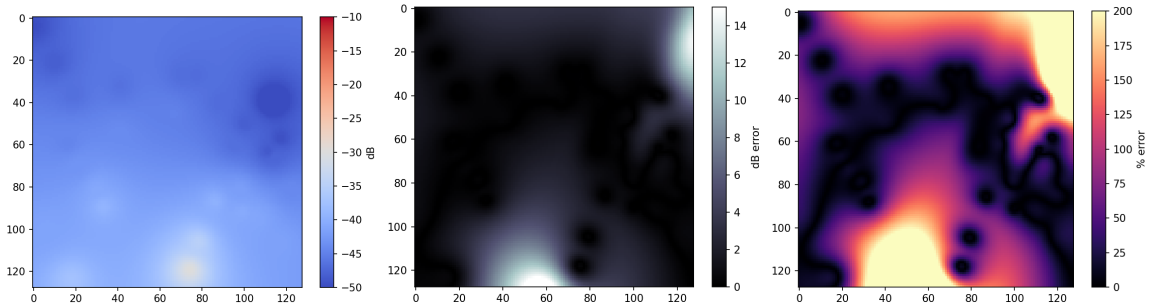

(a) (b) (c)

Figure 6.56. (a) $\beta = 2$ generated REM (b) dB error (c) % error.

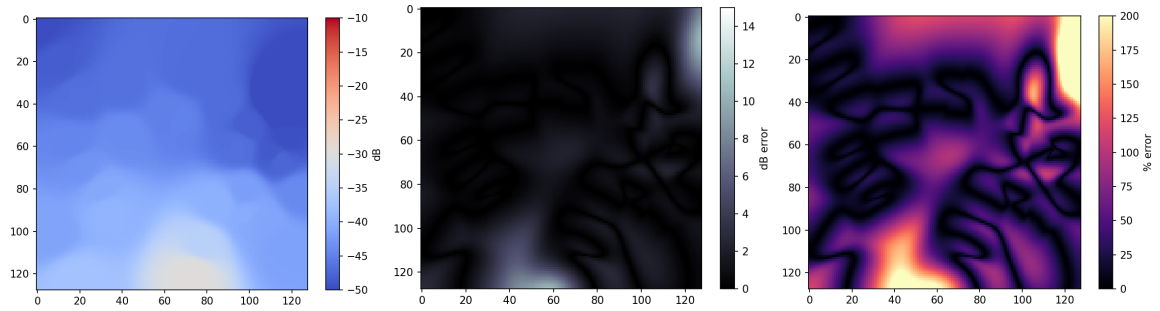

(a) (b) (c)

Figure 6.58. (a) $\beta = 5$ generated REM (b) dB error (c) % error.

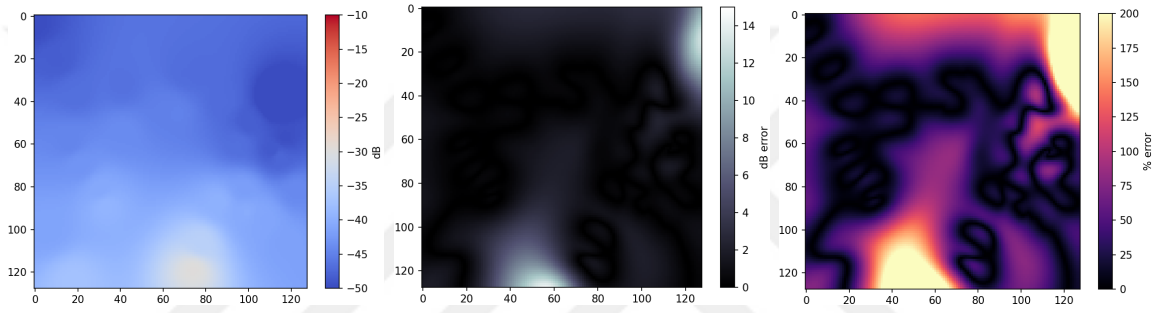

(a) (b) (c)

Figure 6.57. (a) $\beta = 3$ generated REM (b) dB error (c) % error.

Now let us discuss how our algorithms work in this case. As we have previously discussed, we expect our algorithms to have higher error rates in N zone REM cases because our dataset is evenly split between two types and N zone REM can contain much more REM types. This is a known weakness for our algorithms, and it does not change with this example. As it can be seen in Figure 6.59, Main Network algorithm fails to detect the neighboring PU and the high signal strength in the bottom center of the map, and it overshoots the presence of the high PLE zones to the top right side of the map meanwhile not grasping the signal drop rate through the left side of the map. Even though this shows that it fails to grasp the propagation characteristics of the RF environment, it still has reasonable error rates, which shows the weakness of evaluating REM generation only based on numerical error rates.

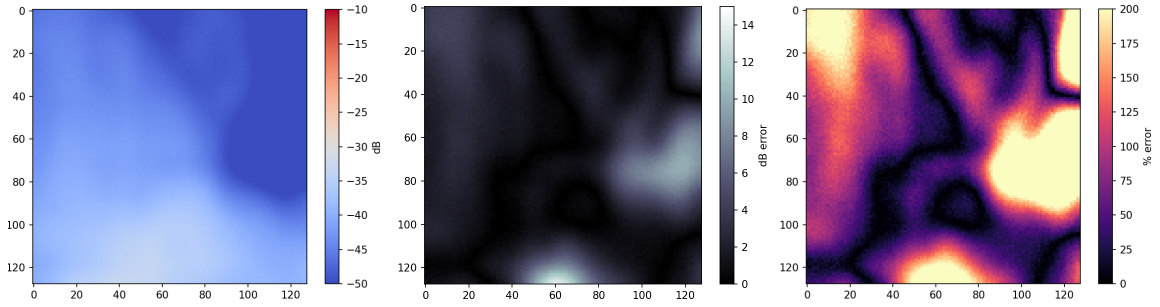

(a) (b) (c)

Figure 6.59. (a) Main network generated REM (b) dB error (c) % error.

In Figure 6.60, we can see how the Dropout Network performs, as it suffers from similar issues as the Main Network, but predicts a higher signal power at the bottom center of the map and does not overshoot the shadowing effect to the right of the map. Still, it fails to recreate a successful representation of the propagation characteristics of the original REM in Figure 6.54.

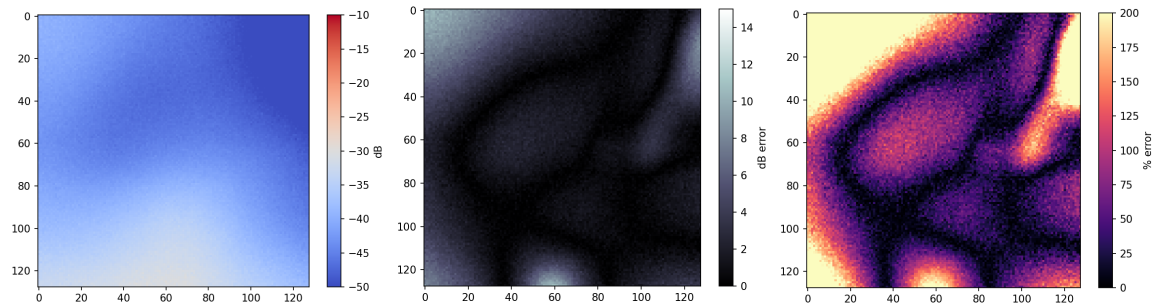

(a) (b) (c)

Figure 6.60. (a) Dropout network generated REM (b) dB error (c) % error.

Surprisingly, our most successful algorithm on detecting the presence of the neighboring PU is the Big Network algorithm. It almost perfectly describes the signal strength at the bottom center of the map, but overestimates it at the bottom left of the map. Even though it has high numerical errors and misses most of the high PLE zones, it is the only algorithm that can detect the presence of a neighboring PU to the A.

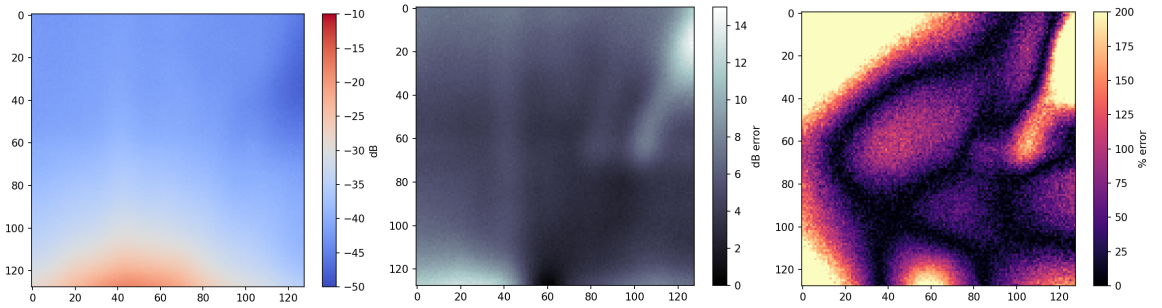

(a) (b) (c)

Figure 6.61. (a) Big network generated REM (b) dB error (c) % error.

6.3.9. Effect of Number of MCD on REM Generation Performance

This subsection is dedicated to analyze how the number of MCDs effect the performance of our REM Generation method. We are focusing only on the Main Network, which was our most successful network. To analyze this, we follow the steps in Figure 6.62.

In Figure 6.63 we see that left axis signify the error rate in dB and the right axis signify the standard deviation of error rate in dB. In the same figure we observe that increasing number of MCDs from 1 to 5 reduces the error rates from 18 dB to 7.8 dB. Also we see that increasing number of MCDs above 20 might seem that it has low impact on dB errors, but increasing the number of MCDs from 20 to 30, decreases the error rate from 1.22 to 1.11, which is a significant 10% improvement. But at the same time we observe an increase at the standard deviation from 0.90 to 0.93 which means that we are making better predictions overall but our consistency is slightly worse.

This concludes our analysis of the solutions we have proposed in the scope of this thesis. To wrap this thesis up we will be discussing what future researchers can focus on the topic of *Radio Environment Map Generation and Performance Evaluation in Heterogeneous Environments* in the next and the final chapter of this thesis.

Require $\mathbf{MCD_i}$, $i = 1, 2, \ldots, N$ are measurement capable devices

Require $\mathbf{REM_j}$, $j = 1, 2, \ldots, M$ are true REMs in test dataset.

for $k = 0$ to $N - 1$ **do**

  for $m = 1$ to M **do**

    Take measurements from first $N - k$ MCDs.

    $\mathbf{M}_{(m,N-k)} \Leftarrow \mathbf{measure}(\mathbf{REM_m}, \mathbf{MCD}[: -k])$;

    Generate IDW map using measurements.

    $\mathbf{IDW}_{(m,N-k)} \Leftarrow \mathbf{generateIDWMap}(\mathbf{M}_{(m,N-k)})$;

    Generate predicted REMs

    $\mathbf{PREM}_{(m,N-k)} \Leftarrow \mathbf{predict}(\mathbf{IDW}_{(m,N-k)})$;

    Calculate errors

    $\mathbf{errors}_{(m,N-k)} \Leftarrow \mathbf{mse}(\mathbf{REM_m}, \mathbf{PREM}_{(m,N-k)})$;

  end for

  Calculate error in dB and standard deviation for number of MCDs equal to $N - k$

  $\mathbf{errordB_{N-k}} \Leftarrow \mathbf{avg}(\mathbf{errors_{N-k}})$;

  $\mathbf{std_{N-k}} \Leftarrow \mathbf{calcStd}(\mathbf{errors_{N-k}})$;

end for

Figure 6.62. Calculating errors for different numbers of MCDs.

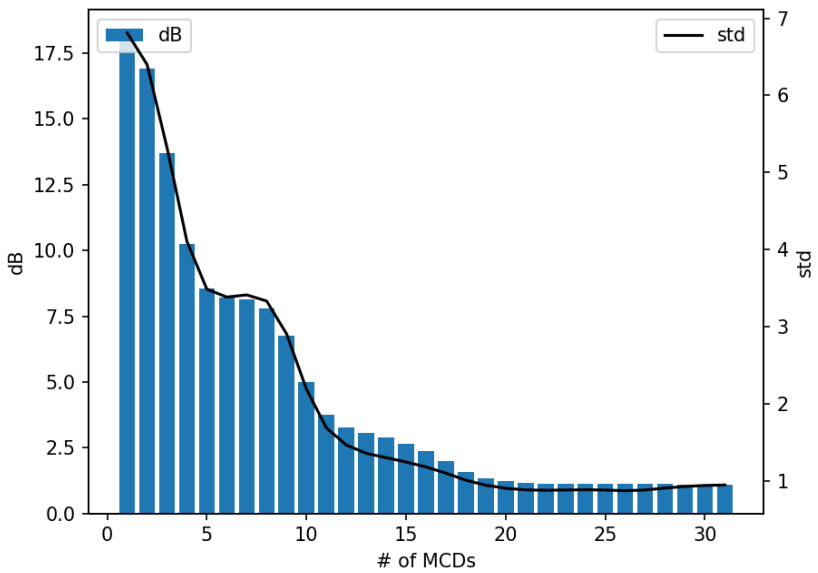

Figure 6.63. Effect of number of MCD on REM generation performance.

7. FURTHER WORK

This chapter discusses topics that could not be addressed within the scope of this project but could be explored in future work. The first of these is the refinement of the assumptions made during the construction of the REM. In this study, when creating regions with different PLE values, each region was assumed to be a homogeneous rectangle. For instance, in region A, where the PLE was set to 2, this value was uniformly applied to every point in the region, and similarly for region B with a PLE of 4. The boundaries of these regions were defined as simple rectangles.

Future researchers could improve upon this by redefining these region boundaries to support irregular shapes and by introducing intra-region variations in PLE using a noise map. Such enhancements would allow the resulting REMs to transition from a discrete to a continuous structure. Following these adjustments, it would also be necessary to evaluate the accuracy of the simulation algorithm and potentially replace the current discrete summation method with one based on integration.

Since the topic of noise has come up, it is worth emphasizing that future researchers should incorporate realistic noise into the measurement process over the constructed REM. In real-world scenarios, noise is expected to arise not only from the environment (e.g., reflections, obstacles, interference) but also from the intrinsic characteristics of the receiving antenna and associated hardware.

Rather than using idealized, noise-free measurements, more accurate simulations would benefit from adding noise distributions—such as Gaussian noise or more complex, context-specific models—to the sampled values. This would allow the neural networks or interpolation algorithms to generalize better and perform more robustly under real-world conditions.

Implementing these modifications within the simulation step would facilitate the generation of more realistic REMs. Rather than categorizing the resulting REM database as *two-zone REM* and *multi-zone REM*, as we have done, selecting REM types that directly correspond to real-world scenarios – for example, indoor REM and outdoor REM – would be a more effective approach. Furthermore, investigating the general propagation characteristics of structures potentially found within indoor or outdoor REMs (such as tables, walls, buildings, or forests) and employing semi-randomization instead of complete randomization of their effects on the REM could yield more realistic results.

Currently, we are generating propagation characteristics for an undefined area and then inferring the type of structure it might contain based on its propagation characteristics. Future researchers could initially define the structure type and then generate semi-randomized zones based on the propagation characteristics of that structure.

Currently, we define PLE as the sole variable governing propagation characteristics. However, researchers may wish to diversify this parameter. We all recognize that the wavelength of the visible light portion of the electromagnetic spectrum varies depending on the medium through which it travels, and we are aware that this principle also applies to radio waves. Consequently, should we not account for changes in the lambda value within the aforementioned Friis transmission equation when transitioning between regions? Considering this, the impact of inter-regional transitions on the signal wavelength should be investigated during simulation and incorporated into the model.

Let us now consider potential modifications to the REM reconstruction process. To ensure a fair comparison of architectural performance and to highlight architectural differences over those attributable to the Neural Network, we employed networks of similar structure for every architecture. Consequently, we may not have fully realized the potential of each architecture. Future researchers could address this by designing Neural Networks specifically tailored to each architecture. These networks may require

the utilization of diverse layer combinations (such as Conv2D, LSTM, Dense, or RNN) based on their individual requirements.

Within the scope of this project, we train initially with a learning rate of 10^{-7}¿, then reduce it to 10^{-8} and repeat the training process while iteratively decreasing the learning rate until observable improvements cease. Future researchers could explore a dynamic selection of this rate, rather than maintaining a fixed value, potentially enabling more successful escape from local minima. When network training performance plateaus around a certain value for an extended period, a checkpoint could be generated and the learning rate dynamically increased in an attempt to escape the local minimum, followed by a subsequent reduction of the learning rate to search for a better result. If the outcome surpasses the previous checkpoint, training continues with this result; otherwise, the process reverts to the last checkpoint and is retried.

Also, this project only focuses on the existence of a single PU that is transmitting in the RF channel. Future researchers could improve on that by increasing the number of transmitting PU antennas. This means that REM generation step should take into account the fact that having multiple transmitting antennas for a PU will cause an effect similar to Multi Path Fading discussed previously. Therefore new method which simulates the REMs with more than one PU should be proposed.

REFERENCES

1. Zhao, Y., J. D. Gaeddert, K. K. Bae and J. H. Reed, "Radio Environment Map Enabled Situation-aware Cognitive Radio Learning Algorithms", *Software Defined Radio Forum (SDRF) Technical Conference*, Orlando, USA, 2006.

2. Ali, Z., H. Ali and M. Badawy, "Internet of Things (IoT): Definitions, Challenges, and Recent Research Directions", *International Journal of Computer Applications*, Vol. 128, pp. 975–8887, 2015.

3. Holker, M., *Telecommunications Engineer's Reference Book*, Butterworth-Heinemann, Oxford, England, 1993.

4. Roberson, D. and W. Webb, *Cognitive Radio Communications and Networks*, Academic Press, Oxford, England, 2010.

5. Pi, Z. and F. Khan, "An Introduction to Millimeter-wave Mobile Broadband Systems", *Communications Magazine*, Vol. 49, No. 6, pp. 101–107, 2011.

6. Levin, H. J., *The Invisible Resource: Use and Regulation of the Radio Spectrum*, RFF Press, New York, USA, 2013.

7. Seflek, I. and E. Yaldiz, "Evaluation of Spectrum Occupancy and Comparison for Three Different Regions", *Journal of Fundamental and Applied Sciences*, Vol. 11, No. 1, pp. 40–64, 2019.

8. Korunur Engiz, B. and Y. A. R. Rajab, "Spectrum Occupancy Measurements in Cellular Frequency Band in Samsun", *Balkan Journal of Electrical and Computer Engineering*, Vol. 9, No. 2, pp. 138–143, 2021.

9. Masonta, M., A. Kliks and M. Mzyece, "Unlocking the Potential of Unoccupied Spectrum in Developing Countries: Southern African Development Community –

Case Study", *Development Southern Africa*, Vol. 34, pp. 1–21, 2017.

10. Moghaddam, S. S., "Cognitive Radio in 4G/5G Wireless Communication Systems", IntechOpen, Rijeka, Croatia, 2018.

11. Ghasemi, A. and E. Sousa, "Collaborative Spectrum Sensing for Opportunistic Aaccess in Fading Environments", *International Symposium on New Frontiers in Dynamic Spectrum Access Networks.*, pp. 131–136, Baltimore, Maryland, USA, 2005.

12. Mitola, J. and G. Maguire, "Cognitive Radio: Making Software Radios More Personal", *Personal Communications*, Vol. 6, No. 4, pp. 13–18, 1999.

13. Haykin, S., "Cognitive Radio: Brain-empowered Wireless Communications", *Journal on Selected Areas in Communications*, Vol. 23, No. 2, pp. 201–220, 2005.

14. Shuaibu-Sadiq, M. and A. I.F, "Analysis of Radio Frequency Spectrum Usage Using Cognitive Radio", *Journal of Electrical, Control and Telecommunication Research*, Vol. 1, pp. 1–8, 2020.

15. Pawełczak, P. and V. Prasad, *Defining Cognitive Radio*, Elsevier Inc., USA, 2010.

16. Devroye, N., M. Vu and V. Tarokh, "Cognitive Radio Networks", *Signal Processing Magazine*, Vol. 25, No. 6, pp. 12–23, 2008.

17. Liang, Y.-C., K.-C. Chen, G. Y. Li and P. Mahonen, "Cognitive Radio Networking and Communications: An Overview", *Transactions on Vehicular Technology*, Vol. 60, No. 7, pp. 3386–3407, 2011.

18. Molina-Tenorio, Y., A. Prieto-Guerrero, R. Aguilar-Gonzalez and M. Lopez-Benitez, "Cooperative Multiband Spectrum Sensing Using Radio Environment Maps and Neural Networks", *Sensors Journal*, Vol. 23, No. 11, 2023.

19. Mao, G., B. D. Anderson and B. Fidan, "Path Loss Exponent Estimation for Wireless Sensor Network Localization", *Computer Networks Journal*, Vol. 51, No. 10, pp. 2467–2483, 2007.

20. Cichoń, K., A. Kliks and H. Bogucka, "Energy-Efficient Cooperative Spectrum Sensing: A Survey", *Communications Surveys & Tutorials*, Vol. 18, No. 3, pp. 1861–1886, 2016.

21. Letaief, K. and W. Zhang, *Cooperative Spectrum Sensing*, Springer, USA, 2007.

22. Shellhammer, S. J., "Spectrum Sensing in 802.22", *IAPR Workshop Cognitive Information Processing*, pp. 9–10, Santorini, Greece, 2008.

23. Atapattu, S., C. Tellambura and H. Jiang, *Energy Detection for Spectrum Sensing in Cognitive Radio*, Vol. 6, Springer, New York, USA, 2014.

24. Boulogeorgos, A.-A. A., N. D. Chatzidiamantis and G. K. Karagiannidis, "Energy Detection Spectrum Sensing Under RF Imperfections", *Transactions on Communications*, Vol. 64, No. 7, pp. 2754–2766, 2016.

25. Sobron, I., P. S. R. Diniz, W. A. Martins and M. Velez, "Energy Detection Technique for Adaptive Spectrum Sensing", *Transactions on Communications*, Vol. 63, No. 3, pp. 617–627, 2015.

26. Johnson, D. H., "Signal-to-Noise Ratio", *Scholarpedia*, Vol. 1, No. 12, p. 2088, 2006.

27. Turin, G., "An Introduction to Matched Filters", *IRE Transactions on Information Theory*, Vol. 6, No. 3, pp. 311–329, 1960.

28. Brito, A., P. Sebastião and F. J. Velez, "Hybrid Matched Filter Detection Spectrum Sensing", *Access Journal*, Vol. 9, pp. 165504–165516, 2021.

29. Kapoor, S., S. Rao and G. Singh, "Opportunistic Spectrum Sensing by Employing Matched Filter in Cognitive Radio Network", *International Conference on Communication Systems and Network Technologies*, pp. 580–583, Katra, India, 2011.

30. Arianandа, D., M. Lakshmanan and H. Nikookar, "A Survey on Spectrum Sensing Techniques for Cognitive Radio", *International Workshop on Cognitive Radio and Advanced Spectrum Management*, pp. 74–79, Aalborg, Denmark, 2009.

31. Shankar, P. M., *Fading and Shadowing in Wireless Systems*, Springer, New York, USA, 2017.

32. Sommer, C., S. Joerer, M. Segata, O. K. Tonguz, R. L. Cigno and F. Dressler, "How Shadowing Hurts Vehicular Communications and How Dynamic Beaconing Can Help", *Transactions on Mobile Computing*, Vol. 14, No. 7, pp. 1411–1421, 2015.

33. Puccinelli, D. and M. Haenggi, "Multipath Fading in Wireless Sensor Networks: Measurements and Interpretation", *Proceedings of the International Conference on Wireless Communications and Mobile Computing*, p. 1039–1044, Association for Computing Machinery, New York, NY, USA, 2006.

34. Watteyne, T., S. Lanzisera, A. Mehta and K. S. J. Pister, "Mitigating Multipath Fading through Channel Hopping in Wireless Sensor Networks", *International Conference on Communications*, pp. 1–5, Cape Town, South Africa, 2010.

35. Mahender, K., T. A. Kumar and K. Ramesh, "Analysis of Multipath Channel Fading Techniques in Wireless Communication Systems", *American Institute of Physics Conference Proceedings*, Vol. 1952, American Institute of Physics Publishing, New York, USA, 2018.

36. Mella, K., *Theory, Simulation and Measurement of Wireless Multipath Fading Channels*, Master's Thesis, Norwegian University of Science and Technology, In-

stitute of Electronic and Telecommunication, 2007.

37. Durgin, G. and T. Rappaport, "Theory of Multipath Shape Factors for Small-Scale Fading Wireless Channels", *Transactions on Antennas and Propagation*, Vol. 48, No. 5, pp. 682–693, 2000.

38. Jeong, J., H. Kim, S. Lee and J. Shin, "An Analysis of Hidden Node Problem in 802.11 Multihop Networks", *International Conference on Networked Computing and Advanced Information Management*, pp. 282–285, Seoul, South Korea, 2010.

39. Ng, P. C., S. C. Liew, K. C. Sha and W. T. To, "Experimental Study of Hidden Node Problem in 802.11 Wireless Networks", *Sigcomm Poster*, Vol. 26, pp. 10–11, 2005.

40. Tsertou, A. and D. I. Laurenson, "Insights Into the Hidden Node Problem", *Proceedings of the International Conference on Wireless Communications and Mobile Computing*, pp. 767–772, Vancouver, Canada, 2006.

41. Yilmaz, H. B., T. Tugcu, F. Alagöz and S. Bayhan, "Radio Environment Map as Enabler for Practical Cognitive Radio Networks", *Communications Magazine*, Vol. 51, No. 12, pp. 162–169, 2013.

42. Zhao, Y., B. Le and J. H. Reed, *Cognitive Radio Technology*, Newnes, Burlington, USA, 2006.

43. Li, J., G. Ding, X. Zhang and Q. Wu, "Recent Advances in Radio Environment Map: A Survey", *Machine Learning and Intelligent Communications: International Conference*, pp. 247–257, Springer, Weihai, China, 2018.

44. Pesko, M., T. Javornik, A. Kosir, M. Štular and M. Mohorcic, "Radio Environment Maps: The Survey of Construction Methods", *KSII Transactions on Internet and Information Systems*, Vol. 8, pp. 3789–3809, 2014.

45. Zhao, Y., L. Morales, J. Gaeddert, K. K. Bae, J.-S. Um and J. H. Reed, "Applying Radio Environment Maps to Cognitive Wireless Regional Area Networks", *International Symposium on New Frontiers in Dynamic Spectrum Access Networks*, pp. 115–118, Dublin, Ireland, 2007.

46. Kaddouri, S., M. E. Hajj, G. Zaharia and G. E. Zein, "Indoor Path Loss Measurements and Modeling in an Open-Space Office at 2.4 GHz and 5.8 GHz in the Presence of People", *International Symposium on Personal, Indoor and Mobile Radio Communications*, pp. 1–7, Bologna, Italy, 2018.

47. Goldsmith, A., *Wireless Communications*, Cambridge University Press, Cambridge, United Kingdom, 2005.

48. Xu, Y.-Q., B. Zhang, B. Zhao and D. Guo, "Radio Environment Map Construction with Spatially Distributed Sensors", *Wireless Communications and Networking Conference Workshops*, pp. 1–7, Nanjing, China, 2021.

49. Zhang, X., Y. Zhao and H. Chen, "Wireless and Satellite Systems", Springer International Publishing, Harbin, China, 2019.

50. Hu, Y. and R. Zhang, "A Spatiotemporal Approach for Secure Crowdsourced Radio Environment Map Construction", *IEEE/ACM Transactions on Networking*, Vol. 28, No. 4, pp. 1790–1803, 2020.

51. Wang, H., R. Ren, D. Qu and G. Zhang, "A Radio Environment Mapping Based Spectrum Awareness for Cognitive Space Information Network with GEO and LEO Coexistence", *International Conference on Wireless Communications and Signal Processing (WCSP)*, pp. 654–659, Wuhan, China, 2020.

52. Amin, S., L. Li, Y. Guo, M. Pan and Y. Gong, "Geo-Indistinguishablility for Crowdsourced-Based Radio Environment Map Construction", *Global Communications Conference*, pp. 1–6, Taipei, Taiwan, 2020.

53. Meshkova, E., J. Ansari, D. Denkovski, J. Riihijarvi, J. Nasreddine, M. Pavloski, L. Gavrilovska and P. Mähönen, "Experimental spectrum sensor testbed for constructing indoor Radio Environmental Maps", *International Symposium on Dynamic Spectrum Access Networks*, pp. 603–607, Aachen, Germany, 2011.

54. Vizziello, A., I. F. Akyildiz, R. Agusti, L. Favalli and P. Savazzi, "Cognitive Radio Resource Management Exploiting Heterogeneous Primary Users", *Global Telecommunications Conference*, pp. 1–5, Houston, USA, 2011.

55. Willink, T. J. and H. Rutagemwa, "Framework for Performance Evaluation of Cognitive Radio Networks in Heterogeneous Environments", *Canadian Conference on Electrical and Computer Engineering*, pp. 199–203, St. John's, Newfoundland, Canada, 2009.

56. Pesko, M., T. Javornik, L. Vidmar, A. Kosir, M. Štular and M. Mohorcic, "The Indirect Self-Tuning Method for Constructing Radio Environment Map Using Omnidirectional or Directional Transmitter Antenna", *EURASIP Journal on Wireless Communications and Networking*, pp. 1–12, 2015.

57. Radojković, M., O. Pronić-Rančić and Z. Marinković, "Inverse Reading of ITU-R P.1546 Propagation Curves for the Broadcast Transmitter EM Field Level", *International Scientific Conference on Information, Communication and Energy Systems and Technologies*, pp. 220–223, Niš, Serbia, 2020.

58. Kaniewski, P., J. Romanik, E. Golan and K. Zubel, "Spectrum Awareness for Cognitive Radios Supported by Radio Environment Maps: Zonal Approach", *Applied Sciences Journal*, Vol. 11, p. 2910, 2021.

59. Chen, Q., J. Yang, M. Huang and Q. Zhou, "ACT-GAN: Radio Map Construction Based on Generative Adversarial Networks With ACT Blocks", *IET Communications*, Vol. 18, pp. 1541–1550, 2024.

60. Wang, Y., S. Sun, N. Liu, L. Xu and L. Wang, "Two-Stage Radio Map Construction With Real Environments and Sparse Measurements", *Wireless Communications Letters*, Vol. 14, No. 4, pp. 969–973, 2025.

61. Li, Y., C. Zhang, W. Wang and Y. Huang, "RadioTransformer: Accurate Radio Map Construction and Coverage Prediction", *arXiv preprint arXiv:2501.05190*, 2025.

62. Pedrotti, F. L., L. M. Pedrotti and L. S. Pedrotti, *Introduction to Optics*, Cambridge University Press, Cambridge, United Kingdom, 2017.

63. Ian Goodfellow, Y. B., Aaron Courville, *Deep Learning*, The MIT Press, Cambridge, MA, USA, 2016.